Construction of a ytterbium and lutetium ion trap and quantum control for multi-partite entanglement

ARJUN DAVID RAO

MSc

THE UNIVERSITY OF
SYDNEY

Supervisor: Dr. Ting Rei Tan
Associate Supervisor: Prof. Michael Biercuk

A thesis submitted in fulfilment of
the requirements for the degree of
Master of Philosophy

School of Science
Faculty of Physics
The University of Sydney
Australia

22 July 2024

Abstract

The technology of linear ion traps are constantly innovating with increasingly varying atomic species being trapped in more scalable systems. In some iterations, multiple species can be confined, offering advanced computing capabilities such as sympathetic cooling. As the ion chains grow in size, the ion operations must scale with it, permitting universal quantum computation in larger qubit arrays. In this thesis, the design, construction and preliminary characterization of a dual-species trapped-ion system is described. Additionally, an investigation into how entangling gates operate in these systems is performed. Laser setups at 355nm drive the spin-motion coupling in ytterbium ions to produce entanglement at high fidelities in longer chains. First, entangling gates are implemented in the ytterbium trap with improvements to the control software. Primitive Mølmer-Sørensen gates are introduced and phase modulated gates using Q-CTRL's graph based optimiser are implemented. Second, entanglement is computationally investigated in multipartite systems. Comparisons are drawn between quantum control techniques such as laser modulation and Rabi rate imbalances are investigated.

Acknowledgements

This is to certify that to the best of my knowledge, the content of this thesis is my own work. This thesis has not been submitted for any degree or other purposes.

I certify that the intellectual content of this thesis is the product of my own work and that all the assistance received in preparing this thesis and sources have been acknowledged.

Arjun David Rao

In this thesis, a big list of thanks is due. But, words on a page cannot express the deep gratitude I feel to all of you.

Firstly, to my parents. Moving to the antipodes in the middle of the pandemic was a challenge. I am so grateful for your support during this time, I couldn't have got this far without quality facetimes, trips and dubs in trivia. To my sister, excited for next installation of sibling trip.

To my friends, whom I miss dearly, home and away. Nate, Adam, Jorge, Bronte, Joe, Howo, Sara, Luce and Alex.

Now to the QCL. I am so proud to have worked in a team of talented and kindhearted individuals.

To Ting Rei, your outstanding knowledge and resilience is hard to come by. It has been a pleasure to work with you and your immeasurable support during this period of my life has not gone unnoticed. A rocky start to the degree came unexpected, but thanks to your generosity I managed to settle in no time.

To Mike, thank you for bringing and welcoming me to Sydney. The effort and dedication you put into the advancement of technology is unparalleled. I can speak for all of us at the QCL that we look up to you and thank you for what you have built for us to learn and develop.

To Jen, when I first arrived you made me feel like I had a home away from home. Thank you.

To Mav, ever grateful to meet real cowboy. Can't believe I have country music saved on my playlist. Shocking. Thank you for the camping trips, surf and conference laughs. To

Chris, thank you for being a living legend. Your patience and attitude to learning is more than inspiring. Also it was a challenge to compete against the GOAT of Dune, the Clovelly green room awaits you. To Tom, thank you for your guidance in the lab - yes with fibre coupling, but also the general advice too. A Michael Phelps in the making. To Billy, your quick wit and insane darts skills continue to impress. The lab is in safe hands, especially if you are blasting Bad Bunny on the speakers. To TWR, yours and Tom's motivational quotes on the whiteboard probably motivated the entire lab for years on end. Thanks for the chats along the way.

To the other members of the QCL as I have been here, Michael Ma, Rob, Joseph, Julian, I am so grateful to have met you all and it has been excellent to have your support throughout and share some Friday croissants. Cheers for everything.

To the Kassal group and co, Ivan, Clare, Ryan, Ben and Vanessa, what a pleasure to collaborate with you all.

Statement of Contribution

Achieving progress in experimental physics is typically a collaborative effort, evident in the extensive author lists in recent publications on quantum physics breakthroughs. This thesis, too, benefited significantly from the valuable input of members of the Quantum Control Laboratory.

The thesis direction and Yb-Lu trap was conceived by Dr. Ting Rei Tan. Octagonal trap design and assembly was completed by Dr. Tan, Dr. Tomas Navickas and myself. Construction of the vacuum system in chapter 3 was completed by all members of the QCL with different components constructed by each team member. Maverick Millican, Dr. Christophe Valahu and Dr. Alistair Milne designed and developed the resonator and Maverick designed the imaging system. Dr. Navickas built the ovens following from the initial design and prototypes from myself and Dr. Tan. The microwave antennae design was created by myself with advice from QCL members. The 369nm laser breadboard was designed by Dr. Valahu and I jointly constructed it. The frequency stabilisation and cavity alignment was performed by myself with help from Dr. Navickas. The bakeout and vacuum protocol along with initial trapping runs were performed by myself, Dr. Navickas, Dr. Valahu, Dr. Tan, Maverick Millican and Vassili Matsos.

In the Yb trap, the trap construction was completed by Dr. Alistair Milne and Dr. Cornelius Hempel. Frequent experimental setup (laser alignment and power optimisation) was performed by Dr. Navickas, Dr. Tan, Maverick Millican, Dr. Valahu and myself. ARTIQ was set up by Dr. Navickas, Tim Wohlers-Reicher, Dr. Tan and myself. The upgrade to DAX was implemented by Dr. Valahu. The experimental scripts for the Mølmer-Sørensen interaction in chapter 4 were developed by myself with valuable advice from Dr. Valahu. The implementation of maximum-likelihood was co-developed with Dr. Valahu. The multitone implementation idea was formulated by Dr. Tan, Dr. Valahu and myself. I created and processed the simulations using the Q-CTRL Boulder Opal suite in Python. Special thanks to Dr. André Carvahlo and Dr. Chris Bentley for creation of the multitone node.

This research reported in this thesis was supported by the award of a Sydney Quantum Academy Program scholarship to the Candidate.

Contents

List of Figures

CHAPTER 1

Introduction

Information processing is becoming ever-present in our daily lives, with computers getting smaller and more efficient with every iteration and hardware improvement. Faster architectures accelerate complex problem-solving, while cloud access seamlessly extends the reach from large data centers to the palm of our hands. Nevertheless, some problems are deemed to be intractable to solve on computers due to their complexity and that the required resources exceed the currently available hardware limits. In response to this challenge, quantum information processing (QIP) has become a dynamic field in physics, aiming to address and solve these intractable problems. Richard Feynman proposed the concept of a 'universal computer' or quantum computer in 1982, laying the foundation for this evolving field [1].

Quantum computers, exploiting the quantum nature of particles, promise unparalleled computational power. Various architectures have been developed to achieve this, each with its own set of advantages and challenges. Among these architectures, the ion trap stands out as a propitious avenue for QIP. By manipulating the quantum properties of ions using sophisticated quantum logic, ion traps enable the encoding of quantum bits, or qubits, which have the potential to outperform traditional bits. The ability to simulate natural sciences and perform quantum computations by leveraging the quantum mechanical properties of trapped ions makes this approach particularly compelling.

This thesis focuses on the design and construction of a trapped ion quantum information processing system within the Quantum Computing Laboratory (QCL). Notably, this system features a unique combination of two distinct ion species, ytterbium (Yb) and lutetium (Lu), within the same trap - an unprecedented exploration in the field. The research also delves into the improvement of state-of-the-art quantum logic gates employed in ion trapping, with a specific emphasis on investigating the Mølmer-Sørensen interaction.

This work aims to contribute to the ongoing advancements in QIP. The combination of diverse ion species and enhancements in quantum logic gates represents a gradual step

forward, unlocking new possibilities for quantum computation and paving the way for future breakthroughs in the field.

The thesis is organised as follows : Chapter 2 introduces the ion trapping field theoretically. It then depicts the two species used, showing their energy levels and how they are prepared into their qubit states. It also delves into the theory of ion operations mediated by laser interactions, either driving just the spin or additionally coupling the motion to produce entangling operations. Chapter 3 describes the experimental setup for the Yb-Lu trap. The preparation of the vacuum is shown along with components that are placed into the vacuum chamber, such as the ovens and microwave addressing apparatus. After this, the current laser setup is described for the Yb-Lu trap, focusing on the ytterbium lasers. Finalising this chapter, the ion trap is shown to trap ytterbium ions by imaging their fluorescence on an EMCCD camera. Chapter 4 describes the entangling gates in ion traps. ARTIQ, a novel control system, is deployed in the Yb trap and experiments are sequenced to prepare and enact both primitive and robust entangling gates. Concluding the thesis, phase modulation and a novel multitone scheme for global entangling gates are investigated. Simulations for these gates are shown by leveraging the Q-Ctrl Boulder Opal optimisation suite. Amplitude inhomogeneity of the laser interaction is investigated and found to reduce the fidelity of multipartite gates, signalling the necessity of equal illumination.

CHAPTER 2

Background theory

The field of quantum computation, like many scientific endeavours, is a blend of different topics. Quantum involves components from experimental and theoretical physics, chemistry, electronics and mechanical engineering. Here, the theoretical information required to present this thesis is included.

2.1 Quantum information

In the information age, ones and zeros are more widespread than ever. Humans store, process and harness information by encoding it into arrays of bits, contributing to the computing power used across the globe today. A significant scientific effort has emerged, intending to enhance this capability. Moore's law states that the number of transistors in integrated circuit technologies doubles every two years [2, 3]; this exponential growth has significantly advanced information encoding and processing capabilities. However, recent progress has been slowing as the physical limits of transistor scaling are being reached. Hence, the pursuit of other ways of encoding information, that can sustain and surpass the pace set by Moore's law, has emerged. Quantum information has emerged as a favourable means in this endeavour.

Quantum information harnesses the inherent properties of quantum states, extracting information from microscopic levels. At the epicentre of this field is the qubit, the quantum mechanical version of the bit. It has advantages over the traditional bit as it exploits these properties. One such property is superposition, where a linear combination of basis states ($|0\rangle, |1\rangle$) can be created. A two-dimensional pure state can be written as

$$|\psi\rangle = a\,|0\rangle + b\,|1\rangle\,. \tag{2.1}$$

Here, a and b are complex values which are normalised, $|a|^2 + |b|^2 = 1$. Upon measurement of the quantum state, the wavefunction collapses into the $|0\rangle$ or $|1\rangle$ state, with a probability according to the Born rule of $|a|^2$ or $|b|^2$ respectively [4]. By completing multiple measurements of a similarly prepared quantum state, the magnitude of the coefficients a and b can be

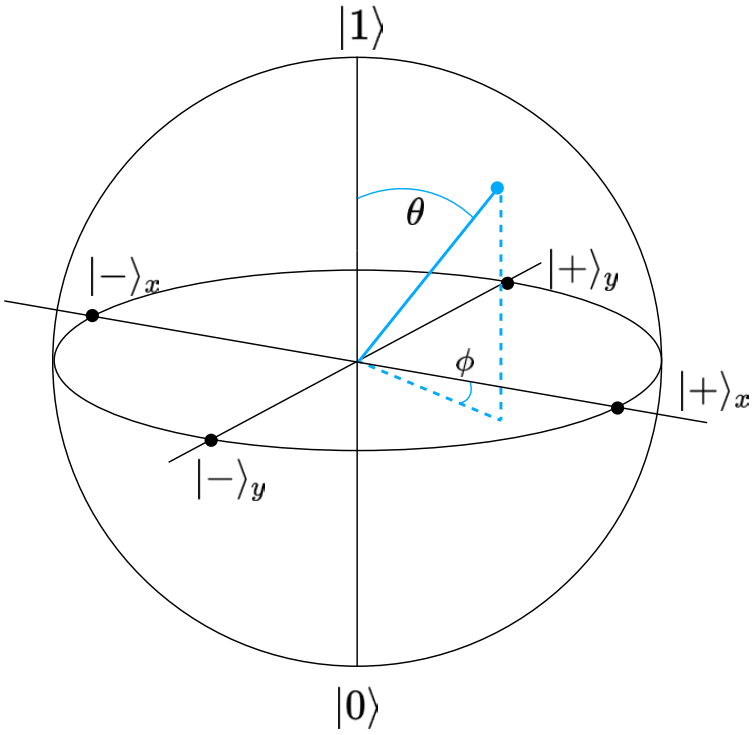

FIGURE 2.1. Bloch sphere representation of a single qubit. It is parametrised with θ, the polar angle and ϕ, the azimuthal angle.

inferred. The coefficients a, b can be parameterised by θ and ϕ and displayed on the Bloch sphere [5, 6]. $\theta \in [0, \pi]$ and is known as the polar angle and $\phi \in [0, 2\pi]$ is the azimuthal angle. Discarding the global phase, the wavefunction can be written as

$$|\psi\rangle = \cos(\theta/2)\,|0\rangle + e^{i\phi}\sin(\theta/2)\,|1\rangle\,. \tag{2.2}$$

This sphere can be used to show how single qubit operations drive the qubit. For example, if a qubit is acted on by a Hamiltonian $H = \hbar\omega_0\sigma_x$, it will rotate around the Y-axis of the Bloch sphere.

2.1.1 Entanglement

Other properties of quantum nature appear when considering more than one qubit. The possible permutations of states considering two qubits are $|00\rangle, |01\rangle, |10\rangle$ and $|11\rangle$. This scales for more qubits as 2^N. An example of a state that you can create out of two qubits

would be

$$|+\rangle_A \otimes |+\rangle_B = \frac{1}{\sqrt{2}}(|0\rangle_A + |1\rangle_A) \otimes \frac{1}{\sqrt{2}}(|0\rangle_B + |1\rangle_B), \tag{2.3}$$

where the $\otimes$ is the tensor product between the two qubit states and the indices A and B refer to the two electronic Hilbert spaces. By expanding this, the wavefunction can be written as

$$|+\rangle_A \otimes |+\rangle_B = \frac{1}{2}|0\rangle_A |0\rangle_B + \frac{1}{2}|0\rangle_A |1\rangle_B + \frac{1}{2}|1\rangle_A |0\rangle_B + \frac{1}{2}|1\rangle_A |1\rangle_B . \tag{2.4}$$

Here, this is an example of a state that is a member of the tensor product between the two Hilbert spaces of H_A and H_B, but they are separable and can be written as a product state between $H_A \otimes H_B$. Entanglement between these two qubits can occur when a state ϕ is created that is not separable. This means that the state cannot be written as a tensor product of the two ions' individual states. For example, the maximally entangled Bell state,

$$\left|\Phi^+\right\rangle = \frac{1}{\sqrt{2}}\left(|0\rangle_A \otimes |0\rangle_B + |1\rangle_A \otimes |1\rangle_B\right), \tag{2.5}$$

cannot be factorised into two separable states. Entanglement is one of the quantum properties which differentiates quantum computation from classical. By combining entangling operations with single qubit rotations, universal quantum computation can be achieved [7]. Trapped ions can enact high fidelity entangling gates and have to date the highest fidelity entangling operations [8, 9].

Entanglement is not just restricted to two qubits, any number of qubits can be entangled. A subset of these states is known as the Greenberger–Horne–Zeilinger (GHZ) states [10], where M qubits are prepared in the following entangled state,

$$|\mathrm{GHZ}\rangle = \frac{|0\rangle^{\otimes M} + |1\rangle^{\otimes M}}{\sqrt{2}}. \tag{2.6}$$

In trapped ions, this can be engineered by using the Mølmer-Sørensen interaction [11, 12]. Entanglement can be generated between arbitrary qubits by illuminating specific ions with laser light or shelving ions with single-ion addressing.

2.2 Ion traps

Different technologies have been competing for the goal of universal quantum computation, such as superconducting circuits [13, 14, 15], nitrogen-vacancy centres [16, 17] and quantum dots [18, 19, 20, 21]. Trapped ions are one such implementation, with high trapping lifetimes and high fidelity entangling gates being among some of the benefits [22, 23, 24, 25, 26, 27]. Ion traps operate on the principle of keeping individual ions confined and then using their

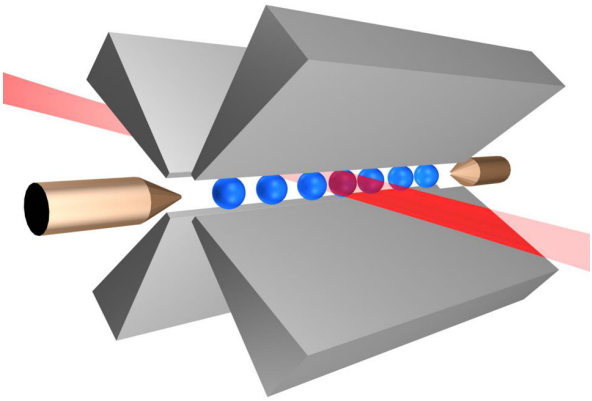

FIGURE 2.2. Schematic of an ion trap showing the four blades and the two endcaps. Here multiple ions are trapped and a laser is focused down onto one ion. Figure taken from [30]

electronic energy levels as the qubit states. This section contains a discussion of the operating principles of trapped ions, with a focus on the mathematical description.

2.2.1 Paul traps

Paul traps, which are used throughout this thesis, use a combination of direct current (DC) and oscillating radio-frequency (RF) electric fields to trap the ions in space [28, 29]. An averaging force on the ions produce the required trapping potential. A linear ion trap consists of two endcaps, to confine the ions axially, and four rods or blades, to confine the ions radially. In the ion traps mentioned in this thesis, the DC field is applied to the endcaps and the RF field is applied to the other two opposing radial electrodes.

The trapping potential Φ in a Paul trap is the following,

$$\Phi(\hat{r},t) = \frac{1}{2}\left(u_x x^2 + u_y y^2 + u_z z^2\right) + \frac{1}{2}\left(v_x x^2 + v_y y^2 + v_z z^2\right)\cos(\Omega_{RF} t) \tag{2.7}$$

$$= \Phi_{DC}(\hat{r}) + \Phi_{RF}(\hat{r},t), \tag{2.8}$$

where u_i are the coefficients for the static fields and v_i are the coefficients for the oscillating fields. Ω_{RF} is the frequency of the oscillating potential applied to the trap. $\Phi_{DC/RF}$ are the potentials of the oscillating and static fields, respectively. The following discussion is adapted from [31, 32]. If tuned correctly, the combination of both of these fields can produce an oscillating saddle potential, which will keep the ion in the trap.

The values of u and v are restricted by Laplace's equation, $\nabla^2\Phi_{DC} = \nabla^2\Phi_{RF} = 0$, so $\sum_i u_i = \sum v_i = 0$. Assuming that the RF potential is uniform and the blades are infinitely

long with $v = v_{rf}(0, 1, -1)$ and the DC confines in the x direction, then $u_x > 0$. The dynamics of the ion are derived using Newton's second law, noting that the electric field is the gradient of the potential,

$$\frac{d^2 r_i}{dt^2} = -\frac{e}{m}\frac{\partial \Phi}{\partial r_i}. \tag{2.9}$$

where $r_i \in x, y$ or z. With the constraints from Laplace's equation and geometrical bounds on the fields, this reduces to a form of the Mathieu equation,

$$\frac{\mathrm{d}^2 r_i}{\mathrm{d}\tau^2} + (a_i - 2q_i \cos(2\tau))\, r_i = 0, \tag{2.10}$$

with the substitutions,

$$\tau = \frac{\Omega_{RF} t + \pi}{2}, \quad a_i = \frac{4eu_i}{m\Omega_{RF}^2}, \quad q_i = \frac{2ev_i}{m\Omega_{RF}^2}, \tag{2.11}$$

where e, m are the charge and mass of the ion. This Mathieu equation has a solution [33],

$$r_i(t) \propto \cos\left(\frac{\sqrt{a_i + q_i^2/2}}{2}\Omega_{RF} t\right)\left[1 + \frac{q_i}{2}\cos\left(\Omega_{RF} t\right)\right]. \tag{2.12}$$

Therefore we have two oscillating components of the ion in each direction. Here, we set $\beta_i = \sqrt{a_i + q_i/2}$. In Equation 2.12, the first term oscillates at the secular frequency $w_i = \beta_i \Omega_{RF} t/2$. From this, one can derive two equations for the axial and radial mode frequencies of the trap. For the axial frequency ω_{axial}, $q_z = 0$, so $\beta_z = \sqrt{a_z}$. The axial and radial frequencies can therefore be written as,

$$\omega_{axial} = \frac{\beta_z}{2}\Omega_{RF} = \frac{\Omega_{RF}}{2}\sqrt{a_z} = \sqrt{\frac{2eV_{DC}}{mZ^2}} \tag{2.13}$$

$$\omega_{radial} = \sqrt{\left(\frac{eV_{RF}}{\sqrt{2}m\Omega_{RF}R^2}\right)^2 - \frac{1}{2}\omega_{axial}^2}, \tag{2.14}$$

where Z is the distance from the trap center to the endcap electrodes and R is the distance from the centre to the radial electrodes. V_{RF} is the peak amplitude of the RF drive. V_{DC} is the DC voltage applied to the endcaps. The other component in Equation 2.12, a driven oscillation at trap drive frequency, is termed the micromotion. This oscillation can negatively impact ion trapping and precise calibration as it causes a Doppler shift on the ions. The coupling to the carrier using a 355nm laser can be reduced and cooling and manipulation of the qubit can be affected [34]. There are two types of micromotion to consider: the first, called intrinsic, is natural to the oscillation and occurs when the ion travels through the RF null whilst oscillating at the trap frequency. The other is the excess micromotion, which is caused when the ion is

displaced from the RF null, normally from laser-charged electrodes, patch effects or electric field offsets. This micromotion can be compensated for by using the compensation electrodes. For more details regarding the location of compensation electrodes in this trap, see Figure 3.3, with the layout of the trap indicating the location of the trap electrodes. For details on how to minimise the excess micromotion, see [32].

2.2.2 Motional modes

As the ion is trapped in the electromagnetic potential well, assuming micromotion is nullified, the ion motion can be shown to be that of a 3D quantum harmonic oscillator with the energy difference between the Fock states of $\hbar\omega$, with the frequency of oscillation dependent on the axis. These quantised energy levels play a key role in trapped ion quantum information processing; they are manipulated for cooling to motional ground states and used as an information bus for qubit operations. The Hamiltonian for a qubit in the harmonic well is then

$$H = \hbar\frac{\omega_0}{2}\sigma_x + \sum_i \hbar\omega_i \left(a_i^\dagger a_i + \frac{1}{2}\right), \tag{2.15}$$

where ω_0 is the qubit energy difference and $a_i, a_i^\dagger$ are the motional jump operators for each coordinate basis, $i \in \{x, y, z\}$ (hats are omitted for operators in this thesis). A single ion in a trap then has three bosonic modes. This scales as more ions are added into the trap, with N ions having $3N$ modes.

Ions in the trap are charged and repulse each other, forming Coulomb crystals if they are cooled. The strong radial confinement in ion traps causes the ions to be extended into a chain along the axial direction, with the spacing between the ions increasing on the outer ions. Due to this repulsion, the displacement of one ion creates a perturbation and the ions can be treated as having normal modes. As more ions are added into the trap, the motional mode frequencies can be calculated by considering their Lagrangian dynamics. Ignoring higher-order terms, the Lagrangian is

$$L = \frac{M}{2}\left[\sum_{m=1}^{N}(\dot{q}_m)^2 - v_{COM}^2 \sum_{n,m=1}^{N} A_{nm} q_n q_m\right], \tag{2.16}$$

with q_m being a small displacement from ion m's equilibrium position [35]. A_{nm} is a real, symmetric matrix for which the eigenvalues and eigenvectors can be found. These eigenvalues provide information about the change in motional frequency of the ion, as

$$\nu_p = \sqrt{\mu_p}\nu_{COM}, \tag{2.17}$$

where ν_p is the mode frequency of mode p, μ_p is the eigenvalue and ν_{COM} is the mode frequency of the centre of mass (COM) mode. This COM mode is the mode in which all the ions move in unison along the same vector. A further discussion of how the scaling of modes in the trap affects the qubit is detailed in Figure 4.12.

2.2.3 Quantum Harmonic Oscillators and Phase space

Now that each of the mode frequencies for the modes is defined, a further investigation of each mode's dynamics can be undertaken by treating the modes as quantum harmonic oscillators (QHO). The Hamiltonian for a particle of mass m in a quantum harmonic oscillator with frequency ω is given by

$$H = \frac{p^2}{2m} + \frac{1}{2}m\omega^2 x^2, \tag{2.18}$$

with the position and momentum operators in the direction of the normal mode eigenvector being x and p. The annihilation and creation operators a and $a^\dagger$ can be constructed from these operators, where

$$a^\dagger = \sqrt{\frac{m\omega}{2\hbar}}\left(x - \frac{i}{m\omega}p_x\right), \tag{2.19}$$

$$a = \sqrt{\frac{m\omega}{2\hbar}}\left(x + \frac{i}{m\omega}p_x\right). \tag{2.20}$$

The Hamiltonian can be rewritten in the form

$$H = \hbar\omega\left(a^\dagger a + \frac{1}{2}\right), \tag{2.21}$$

where the operators act on the Fock state $|n\rangle$ by changing the motional quanta as follows

$$a\,|n\rangle = \sqrt{n}\,|n-1\rangle\,, a^\dagger\,|n\rangle = \sqrt{n+1}\,|n+1\rangle\,. \tag{2.22}$$

For a more comprehensive explanation, refer to [7].

2.3 Ions

Different types of charged particles can be trapped in an ion trap. For example, some Penning trap experiments have successfully confined antiprotons [36]. The candidates for quantum information processing in linear ion traps are chosen according to strict criteria, with different species. Typically, chosen ions are those that, when singly ionised, have similar properties to hydrogen (one electron in the outer shell). Another consideration is the overhead required for laser control and cooling of the ions. Some laser frequencies are easier to operate and build

appropriate hardware to support them, hence this is taken into account in the choice of ion. Some typical examples include $^{88}Sr^{+}$ [37], $^{9}Be^{+}$ [38], $^{25}Mg^{+}$ [38] or $^{43}Ca^{+}$[9, 39].

In this thesis, two elements are considered, ytterbium and lutetium, which are next to each other in the periodic table. They are both heavier trapped ions, meaning their mode frequencies are higher for a given trap depth.

2.3.1 Ytterbium

The ytterbium ion is the main ion considered in this thesis. The atom has atomic number 70 and its electronic structure when one electron is removed is a good candidate for ion trap quantum computation. Ionised ytterbium has cooling transitions which are readily achieved optically (UV). A specific isotope of ytterbium 171 is chosen for this, as odd numbers of neutrons mean Ytterbium has a spin-half nucleus. This isotope is also stable and can be manufactured to be isotopically pure to high percentages. The spin half nucleus provokes a hyperfine splitting where the nucleus and electronic magnetic moments interact, causing the ground state to split into two with a splitting of 12.64GHz [40]. These ground states are called clock states, with a first-order insensitivity to magnetic fields. As such, the splitting is $\delta_z = 12.642821\text{GHz} + \delta_{2z}$, where $\delta_{2z} = \mathcal{O}(B^2)$ and B is the magnetic field.

Ionising and loading these atoms in the trap require a two-photon process. Firstly, a 399 nm beam illuminates the neutral atom flux, exciting the ${}^1S_0 \leftrightarrow {}^1P_1$ transition. Then, light from the 369.5nm laser excites the ${}^1P_1$ line to ionisation. Typically, the 355nm laser light illuminates the ions to provide extra ionisation light. For loading, either the isotope 171 or 174 can be trapped. The latter is sometimes chosen during the initial trapping of a new system as it can be easier to trap. To choose which ion to load, also known as isotope selectivity, the 399nm frequency is tuned.

Once the ion is ionised, it becomes affected by the electric fields present in the trapping region and it falls into the saddle potential well in the centre of the trap. Once this occurs, the ion can typically stay within the trap for months. Other lasers are then used to drive transitions within the trapped ion.

2.3.2 Lutetium

The other ion in the newly constructed trap is lutetium, which has an atomic number of 71. It is a favourable qubit and qutrit as it has a large hyperfine splitting of 10.49GHz and 11.29GHz and two clock transitions. The two most abundant isotopes of lutetium are 175 and 176,

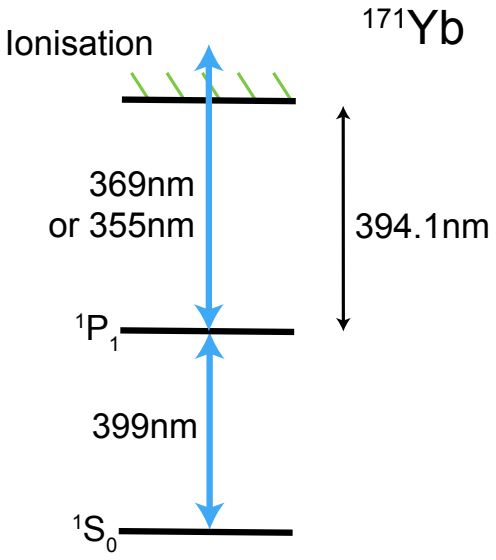

(A) Neutral Ytterbium transitions, showing the wavelengths required for ionisation.

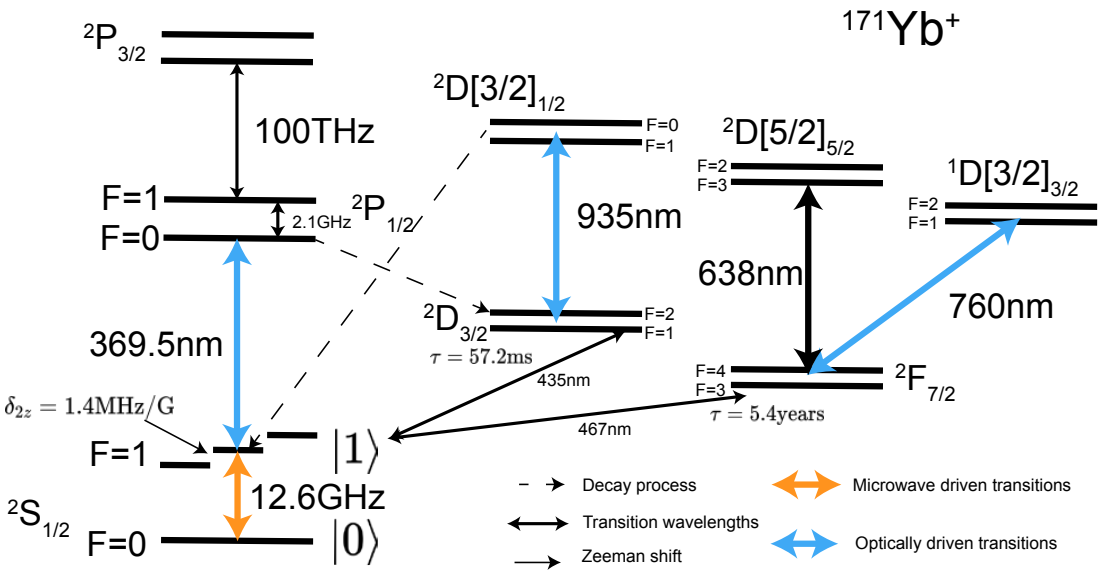

(B) Energy levels for singly ionised Ytterbium 171

FIGURE 2.3. a). By applying a 399nm laser alongside a 369nm laser, the neutral atom flux can be ionised, allowing it to experience the electric fields and fall into the trap. b). Singly ionised Yb is shown, with the qubit encoded in the hyperfine levels of the $^2S_{1/2}$ states. The optical pumping, detection and Doppler cooling transition is shown with the 369.5nm laser driving the interactions. Also the 935nm and 760nm assist in the repumping to the $^2S_{1/2}$ hyperfine manifold.

with nuclear spin $I = 7/2$ and $I = 7$ respectively. 176 is chosen for this thesis as it has $m_f = 0$ states which are suitable for quantum information processing due to its insensitivity to magnetic fields, similar to the clock states in ytterbium. Energy level structures of lutetium for ionisation and singly ionised $^{176}Lu^+$ are shown in Figure 2.4 [41].

To ionise lutetium and trap, a two-photon process is used to first excite the $^2D_{3/2}$ transition to the $^2D^0_{3/2}$ transition and secondly to ionisation using 451nm light [42, 43]. This provides isotope selectivity, as the transition frequency will differ depending on the isotope [44].

2.3.3 Doppler cooling

Cooling of the ion along its secular frequencies is critical as by doing so they form a stable crystal. There are multiple schemes used to achieve low average phonon number ($\bar{n}$) for each ion. Doppler cooling will be presented here, where a transition in the ion is manipulated to absorb and reemit a photon and lose kinetic energy. The first step is the absorption of a red-detuned photon. The ions travelling towards the laser wavevector will see the field as blue-detuned and absorb the photon as if it were on resonance. By the conservation of momentum, this absorption will impart a momentum kick along the laser wavevector. This momentum kick will overall reduce the overall momentum of the ion in the lab frame.

Cooling occurs as the photon is then reemitted isotropically, where the ion receives a momentum kick in the opposite direction to the emission vector. As this photon emission is random, over the average of many cycles this will selectively slow down the ion in the direction of the laser wavevector. and can reach a temperature related to the Doppler limit. The linewidth of the $^2S_{1/2} \leftrightarrow {}^2P_{1/2}$ transition in $^{171}Yb^+$ of 19.6MHz gives a minimum temperature achievable of $T_D = 470\mu$K. In $^{176}Lu^+$, the linewidth of the $^3D_1 \leftrightarrow {}^3P_0$ transition is 2.5MHz and gives $T_D = 60\mu$K. The temperature is calculated from

$$T_D = \frac{\hbar\Gamma}{2k_B}, \tag{2.23}$$

where Γ is the linewidth of the transition and k_B is the Boltzmann constant. To cool the ion over all three trap directions, the laser must have a vector component along all three directions and is thus incident upon the ion diagonally with respect to the blade electrodes.

The cooling transitions in $^{171}Yb^+$and $^{176}Lu^+$are not cyclical, meaning that there is a small chance that the state population leaks to another state. In $^{171}Yb^+$, the transition chosen for Doppler cooling is the $^2S_{1/2}|F = 1\rangle \leftrightarrow^2 P_{1/2}|F = 0\rangle$ transition at 369 nm and the frequency stabilised laser described in subsection 3.2.1 is chosen for this. It has a 0.5% chance of

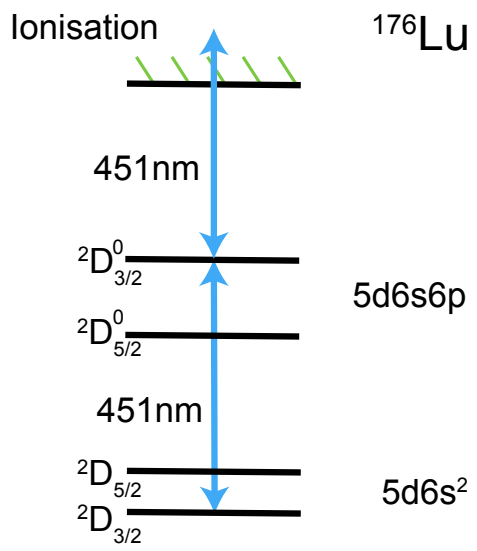

(A) Neutral Lutetium transitions, showing the wavelengths required for ionisation.

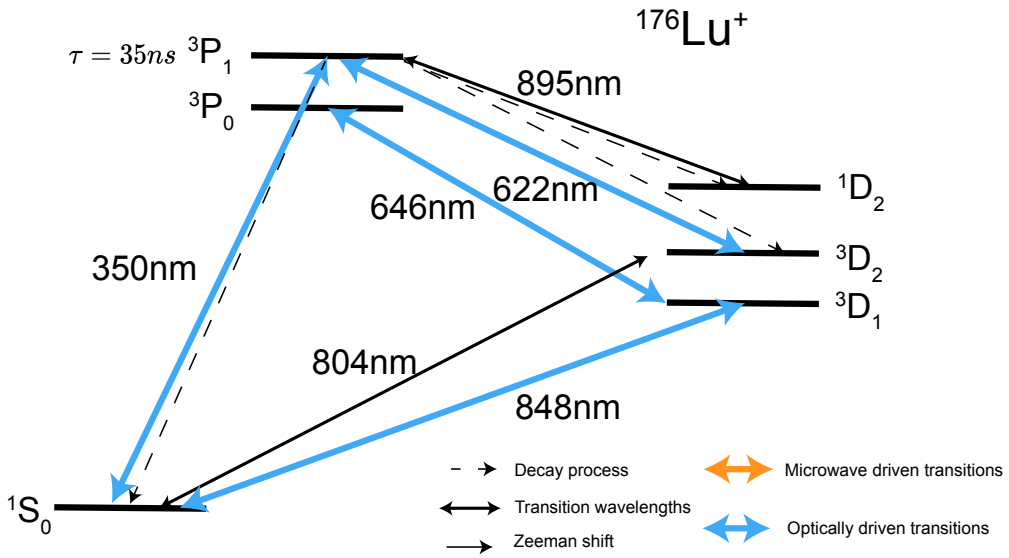

(B) Energy levels for singly ionised Lutetium 176

FIGURE 2.4. a) Neutral atom energy level diagram showing the two-photon process leading to ionisation. Two 451nm beams are targeted onto the ion, exciting it into the higher $^2D^0_{3/2}$ state and then to ionisation. b) Key transitions in the Lutetium energy levels. Hyperfine levels are not shown in this plot. 350nm and 622nm are used as repump lasers to keep the qubit in the cyclical transition between $^3D_1$ and $^3P_0$. This transition at 646nm is used for Doppler cooling, state detection and optical pumping. 848nm is used in detection methods to shelve the $^3D_1\,|F = 7, m_f = 0\rangle$ state, allowing the other hyperfine levels to fluoresce when the 646nm laser is applied.

decaying to ${}^2D_{2/3}$, so the 935 nm laser serves to repopulate the manifold ${}^2D[3/2]_{1/2}$, where it decays to ${}^2S_{1/2}\,|F=0\rangle$.

In $^{176}\text{Lu}^+$, Doppler cooling is achieved by scattering on the ${}^3D_1 \leftrightarrow {}^3P_0$ transition at 646 nm. This is also a near-perfect cyclical transition, meaning that Doppler cooling can be performed given that the decays are accounted for by repumping lasers. As seen in Figure 2.4b, decays can occur from the ${}^3P_1$ state to ${}^1S_0$, ${}^3D_1$, ${}^3D_2$ and ${}^1D_2$ states. The frequencies required to coherently repump the ion are 350 nm, 646 nm, 622 nm and 895 nm. The hyperfine splitting of the ${}^3D_1$ state is required to be addressed to perform Doppler cooling as there is an 11.29 GHz splitting between $|F=7\rangle$ and $|F=6\rangle$ and 10.49 GHz splitting between $|8\rangle$ and $|7\rangle$. As such, three co-propagating laser fields with detunings Δ_6, Δ_7 and Δ_8 drive the transition. Each field is set to be red detuned from the transitions ${}^3D_1\,|F=6,7,8\rangle \leftrightarrow {}^3P_0$ and slightly different to avoid dark states [43]. The laser setup for the $^{176}\text{Lu}^+$ion is not described in this thesis.

2.3.4 State preparation and detection

Preparing the qubit state in $|0\rangle$ requires the application of laser beams. After Doppler cooling, the ion may be in the $|0\rangle$ or $|1\rangle$ state. To prepare the qubit in $|0\rangle$, a laser on the ${}^2S_{1/2}\,|F=1\rangle \leftrightarrow {}^2P_{1/2}\,|F=1\rangle$ at 369.5 nm is targeted on the ions. An electro-optical modulator (EOM) adds a 2.105 GHz sideband onto the ion, bridging the hyperfine splitting of the ${}^2P_{1/2}$ level. This laser couples only the $|1\rangle$ state to the P level, inducing a transition. The ion will then decay back down to either the $|0\rangle$ or $|1\rangle$ state, with a 1/3 chance of decay to $|0\rangle$. After repeated operations of this incoherent process, the population can be prepared with high fidelity into the ground state of the qubit.

For lutetium, a similar process is required, where efficient state preparation in the hyperfine level ${}^3D_1\,|F=7,m_f=0\rangle$ is required. The same three laser fields of 646 nm used to address ${}^3D_1\,|F=6,7,8\rangle \leftrightarrow {}^3P_0\,|F=7\rangle$ to perform Doppler Cooling are used. However, the field addressing the ${}^3D_1\,|F=7\rangle \leftrightarrow {}^3P_0\,|F=7\rangle$ is replaced with a π-polarised field. With this laser, the transition ${}^3D_1\,|F=7,m_f=0\rangle \leftrightarrow {}^3P_0\,|F=7,m_f=0\rangle$ is forbidden. Any population that decays into the $|F=7,m_f=0\rangle$ is therefore decoupled from the interaction. Repeated driving of these three fields results in effective optical pumping into the qubit ground state${}^3D_1\,|F=7,m_f=0\rangle$.

After preparation and qubit operations, efficient detection is required to differentiate between the $|1\rangle$ and $|0\rangle$ states. To do so in $^{171}\text{Yb}^+$, the 369.5 nm laser is again used to drive ${}^2S_{1/2}\,|F=1\rangle \leftrightarrow {}^2P_{1/2}\,|F=0\rangle$ transition. If the qubit is projected in the upper qubit state

$^2S_{1/2}\left|F=1\right\rangle$, then the population will transfer to the upper $^2P_{1/2}$ state and then decay back, scattering photons which are collected as described in subsection 3.1.7. If the population was instead in the ground state, then no photons are scattered. In $^{176}Lu^+$, a similar process of state detection is used. However, in this process, a laser at 848 nm is used to drive the ion from $^3D_1\left|F=7,m_f=0\right\rangle$ to the $^1S_0\left|F=7,m_f=-1\right\rangle$. Following this, detection with a 646 nm laser resonant to the $^3P_0$ state reveals if the qubit is in the other hyperfine levels ($\left|F=8\right\rangle,\left|F=6\right\rangle$. Light at 646 nm will be collected if it is in either of these states and the fluorescence will not be observed if the ion is in the $\left|F=7\right\rangle$ state.

2.4 Entangling operations in trapped ions

2.4.1 Stimulated Raman transitions

Microwaves or lasers can be used to couple the motional and electronic states of the ions, to enable entangling gates in trapped ion systems. The former has a limitation, where the Lamb-Dicke parameters of the coupling interaction are small, due to the long wavelength of the microwaves. Instead of microwaves, this thesis uses lasers where the coupling between electronic and motional states is driven by optically stimulated Raman transitions within the ion.

The Lamb-Dicke parameter is the factor which describes the coupling factor between a motional mode and an atom-light interaction and is represented by η_i, where

$$\eta_i = k_i i_0 = k_i\sqrt{\left\langle 0\left|i^2\right|0\right\rangle} = \sqrt{\frac{\hbar}{2m\omega_i}}, \tag{2.24}$$

where $i\in\{x,y,z\}$ and i_0 is the spread of the zero point wavefunction in a Cartesian direction. k_i is the laser wavevector, m is the ion mass and ω_i is the mode frequency of the mode being addressed along direction i [35]. For $^{171}Yb^+$, a 355 nm pulsed laser is used, with a Lamb-Dicke factor of $\eta_x\approx 0.085$, dependent on the Rabi frequency of the Raman laser. A two-photon process couples the $|0\rangle$ and $|1\rangle$ states, with the energy difference being $\hbar\omega_0$. These two beams are known as "pump" and "probe" beams, where the combination of both makes the electronic state absorb a pump photon and reemit one at the energy of the probe. Enabling this in trapped ions thus requires two beams, if they are orthogonal to each other then their combined wavevector can target motional sidebands of the electronic state, a factor key to entangling gates. To understand this, the Hamiltonian in the interaction picture of a single ion with a harmonic oscillator mode driven by a laser is described. A simplification is made in this derivation, where the difference in wavevector of the two beams is only shown to be in

the direction of the motional mode (the unit vector $\hat{\mathbf{x}}$) so that $\vec{\mathbf{k}}.\tilde{\mathbf{r}} = k_x\hat{\mathbf{x}}$. $\vec{\mathbf{k}}$ is the difference in wavevector between the two pump and probe beams, $\hat{\mathbf{r}}$ is the vector for the modes, and k_x is the scalar wavevector in only one coordinate basis $\hat{\mathbf{x}}$. The derivation is similar to the two-qubit case in subsection 2.4.4, with the Hamiltonian in the interaction picture after two Taylor expansions [34],

$$H_{\text{int}} = \frac{\hbar\Omega_0}{2}\left(\sigma_+ e^{-i(\phi+\Delta t)}\left(\mathbf{1} + i\eta\left(ae^{-i\omega_x t} + a^\dagger e^{i\omega_x t}\right)\right)\right) + \text{ h.c}\,, \tag{2.25}$$

where Ω_0 is the Rabi frequency, Δ is the detuning of the beam from the carrier transition, $a, a^\dagger$ are the annihilation and creation operators, σ_+ is defined in terms of the Pauli spin matrices $\sigma_+ = 1/2(\sigma_x - i\sigma_y)$. To target the carrier or motional sideband transitions, the detuning of the beam can be set so that the difference between the pump and probe beams is $\omega_0 + \Delta$, where $\Delta = 0, -\omega_r, \omega_r$. The transitions that are induced are a carrier, red sideband and blue sideband respectively. The Hamiltonian describing a carrier transition after applying a rotating wave approximation (RWA) is

$$H_{carrier} = \frac{\hbar\Omega_0}{2}\left(\sigma_+ e^{i\phi} + \sigma_- e^{-i\phi}\right), \tag{2.26}$$

which tranfers population between the ground and excited levels, with $t_\pi = \frac{\pi}{\Omega_0}$. Here $t_p i$ is known as the pi-time and describes the time taken to transfer the qubit population between $|0\rangle$ and $|1\rangle$.

When the detuning is set to the motional frequency $\Delta = \omega_r$, then blue-sideband transition is induced, creating a transition with the electronic and motional states. This transition is $|g\rangle|n\rangle \leftrightarrow |e\rangle|n+1\rangle$ and the Hamiltonian after an RWA is

$$H_{BSB} = \frac{i\hbar\Omega_0\eta}{2}\left(a\sigma_- e^{-i\phi} + a^\dagger\sigma_+ e^{+i\phi}\right). \tag{2.27}$$

If the detuning is set to $\Delta = -\omega_r$, then a transition between $|g\rangle|n\rangle \leftrightarrow |e\rangle|n-1\rangle$ is induced, which is frequently used for cooling the motional state and known as the red-sideband. The Hamiltonian after an RWA is

$$H_{RSB} = \frac{i\hbar\Omega_0}{2}\eta\left(\hat{a}\hat{\sigma}_+ e^{i\phi} - \hat{a}^\dagger\hat{\sigma}_- e^{-i\phi}\right). \tag{2.28}$$

2.4.2 AC Stark Shift

A Stark effect is the shifting or splitting of energy levels due to an external field and the Aulter-Townes effect (or the AC Stark shift) [45, 46] is specifically when these effects are due to an oscillating field. The presence of an external laser field can therefored produce a σ_z shift on the ion, which is detrimental to qubit calibrations and operations. This energy shift

δ_{SS} is given by

$$\delta_{SS} = \pm\frac{\Omega^2}{4\Delta}, \tag{2.29}$$

for $\Delta \gg \Omega$. Here, Δ is the detuning from the transition and Ω is the Rabi rate of the applied field.

2.4.3 Frequency, amplitude and phase modulation

Modulation of signals is ubiquitous in scientific fields and plays a particular role in quantum control. Amplitude modulation (AM) and frequency modulation (FM) relate to how radio waves are changed by amplitude or frequency modulation to carry information for radio. In Figure 2.5 unmodulated waveforms along with phase modulation and amplitude modulated waveforms are shown.

This is relevant for trapped ions, as by changing the amplitude or frequency of a pulse, the interaction strength and interaction that takes place will change [47]. To give an example, imagine two qubits are affected by the same σ_x interaction, however, one qubit has a stronger interaction strength than the other. If a bit flip operation on both qubits is desired, it cannot be completed with high fidelity as one qubit will either be over or underdriven. By using frequency and amplitude modulation, the interaction can be manipulated so that the net interaction after time τ leaves the qubits in the $|01\rangle$ state. The exact amplitude and frequency modulation required to complete this can be calculated analytically, but for larger Hilbert spaces this can quickly lead to complexity. It therefore becomes an optimisation problem, where a cost function of infidelity from a target state is minimised.

This optimisation problem can be optimised by various methods, in this thesis, the optimisations come from using gradient-based deterministic optimisation in the Q-CTRL python package [48, 49]. This is embedded into the control software for the hardware, known as ARTIQ [50].

To investigate these modulation techniques, the waveform is described as

$$y(t) = A\cos(\omega t + \phi), \tag{2.30}$$

where y is the value of the waveform in time, A is the amplitude, ω is the frequency, t is the time and ϕ the phase. Firstly, amplitude modulation involves making the amplitude of the waveform vary over time, leading to $A \to A(t)$. Secondly, frequency modulation makes $\omega \to \omega(t)$ and finally phase modulation $\phi \to \phi(t)$. The latter two forms of modulation are related as the frequency is the time derivative of the phase $\omega(t) = \frac{d\phi(t)}{dt}$. With $m(t)$ being the

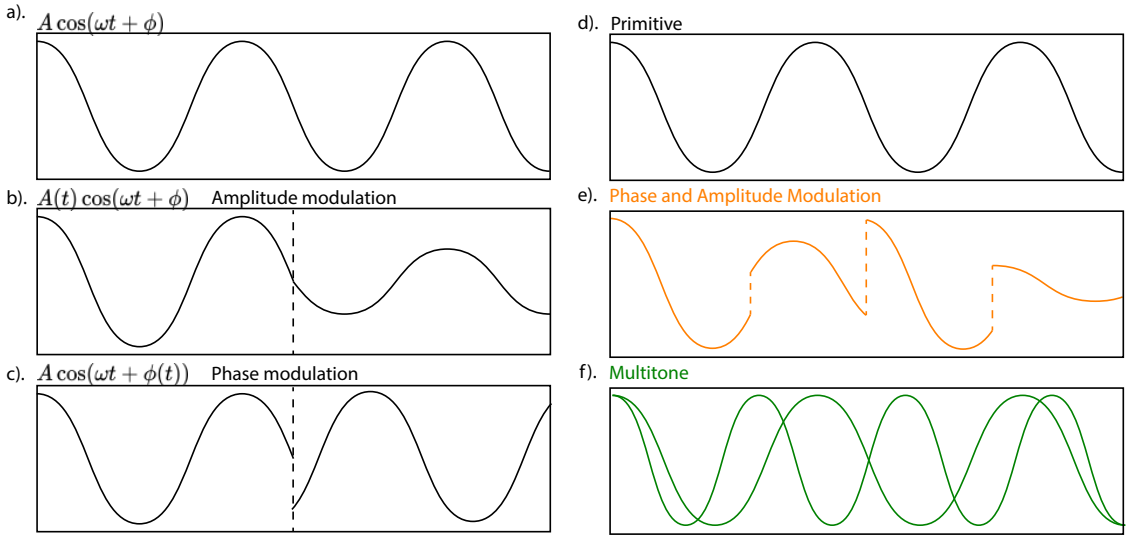

FIGURE 2.5. Summary of modulation schemes. On the left-hand side of the panels, firstly a standard waveform is in **a**. Below in panels **b** and **c**are the effect on the waveform of amplitude modulation and then phase modulation. On the right-hand side, in panel **d**, a primitive waveform for a Mølmer-Sørensen gate is shown. Then in panels **e** and **f**, the combination of phase and amplitude modulation and finally multiple tones are superimposed.

phase modulated drive and assuming that the modulated field gives $A\cos(\omega_0 t+\phi_0+m(t))$, the desired modulation can be achieved either by setting $\phi(t)=\phi_0+m(t)$ or $\omega(t)=\omega_0+\frac{dm(t)}{dt}$.

2.4.4 Mølmer-Sørensen interaction

Entangling gates were first proposed using a sequence of red sideband pulses on two ions [22]. After this successful creation of entangled states, a scheme [11] which is independent of the initial motional state of the ions was created. It uses one bichromatic Raman beam, targeting the blue- and red-sidebands. The Mølmer-Sørensen method has been implemented for entanglement creation in trapped ions for 20 years and many enhancements to the scheme have been implemented to reduce its sensitivity to noise. To understand how the gate operates, a mathematical description of this interaction follows.

The Hamiltonian describing the two-qubit system with its harmonic oscillator along with the interaction of the Raman beams is defined as

$$H = H_{qubit} + H_{boson} + H_{int} \tag{2.31}$$

$$H_{qubit} = \frac{\hbar\omega_o}{2}\sum_i \sigma_z^i, \tag{2.32}$$

$$H_{boson} = \hbar\omega_r a^\dagger a, \tag{2.33}$$

with ω_r being the mode frequency, σ_z being the Pauli-Z operator, ω_0 as the qubit frequency and $a/a^\dagger$ as the motional annihilation/creation operators. The Hamiltonian H_{int} describes the interaction term between the a pair of laser beams directed on both ions. The beams are bichromatic and detuned by the same amount on each ion, close to the red- and blue-sidebands. It is as follows, with $S_{+/-} = \sum_i \sigma_{+/-}^i$, with i being the ion index of the two ions.

$$H_{int} = \frac{\hbar\Omega_0}{2}(S_+ + S_-)(e^{i(kx-\omega t-\phi)} + e^{-i(kx-\omega t-\phi)}), \tag{2.34}$$

where Ω_0 is the carrier Rabi frequency, ϕ, ω and k are respectively the phase and frequency and wavevector of the electromagnetic field. Converting to the interaction picture with $H_0 = H_{qubit} + H_{boson}$ and assuming the fields affecting each ion are matched and the detuning of the laser frequency from the transition frequency on each ion is equal gives the following effective Hamiltonian,

$$\tilde{H}_{\text{eff}} = \frac{\hbar}{2}\left[\Omega_0 e^{i\delta' t} S_- e^{i\eta\left(a^\dagger e^{i\omega_r t} + a e^{-i\omega_r t}\right)} + \Omega_0^* e^{-i\delta' t} S_+ e^{-i\eta\left(a^\dagger e^{i\omega_r t} + a e^{-i\omega_r t}\right)}\right], \tag{2.35}$$

$\delta' = \omega - \omega_0$ is the detuning of the laser from the qubit frequency. To arrive at the Hamiltonians for the carrier and sideband transitions, the Lamb-Dicke approximation $\eta\sqrt{\bar{n}} \leq 1$ must be assumed to reduce the exponential via Taylor expansion to first-order terms. $\bar{n}$ is the mean phonon number of the motional mode. The Lamb-Dicke approximation can be assumed if sufficient cooling is obtained. The Hamiltonian with the Lamb-Dicke approximation is therefore

$$H_{int} = \frac{\hbar}{2}\Big[\Omega e^{i\delta' t} S_- + \Omega^* e^{-i\delta' t} S_+ \tag{2.36}$$

$$+ i\eta\left(\Omega e^{i(\delta'-\omega_r)} S_- a - \Omega^* e^{-i(\delta'-\omega_r)} S_+ a^\dagger\right) \tag{2.37}$$

$$+ i\eta\left(\Omega e^{i(\delta'+\omega_r)} S_- a^\dagger - \Omega^* e^{-i(\delta'+\omega_r)} S_+ a\right)\Big], \tag{2.38}$$

Further approximating the Hamiltonian using the rotating wave approximation simplifies the exponential terms. In addition, the Mølmer-Sørensen gate only considers the blue- and red-sideband terms (terms like Equation 2.27 and Equation 2.28). Also, the detunings from

each sideband δ_b and δ_r are set to be equal and opposite in sign so that $\delta_b = -\delta_r = \epsilon$. After setting the Rabi amplitude equal for each sideband so that $\Omega_r = \Omega_b$, the Hamiltonian for the Mølmer-Sørensen interaction is,

$$H_{MS} = i\frac{\hbar\eta\Omega_0}{2}\left[\left(S_- e^{i\phi_s} - S_+ e^{-i\phi_s}\right)\left(a e^{i\epsilon t} e^{i\phi_m} + a^\dagger e^{-i\epsilon t} e^{-i\phi_m}\right)\right], \tag{2.39}$$

where the spin and motional phases are defined as $\phi_s = (\phi_b + \phi_r)/2$ and $\phi_m = (\phi_b - \phi_r)/2$ where the $\phi_{b/r}$ are the blue- or red-sideband phases. The propagator for this Hamiltonian can now be found using the Magnus expansion [51]. Only the first two terms in the expansion are non-zero, giving the following,

$$U_{MS}(t) = \exp\left[S(\alpha(t)a + \alpha^*(t)a^\dagger) + iS^2\Phi(t)\right], \tag{2.40}$$

with

$$\alpha(t) = \frac{\eta\Omega_0}{2}\frac{e^{i\epsilon t} - 1}{i\epsilon}e^{i\phi_m}, \quad \Phi(t) = \left(\frac{\eta\Omega_0}{2\epsilon}\right)^2\left[\epsilon t - \sin(\epsilon t)\right], \tag{2.41}$$

where S is defined as $S = S_- e^{i\phi_s} - S_+ e^{-i\phi_s}$. $\alpha(t)$ is the coherent displacement of the wavepacket induced by the spin-motion interaction and $\Phi(t)$ is the geometric phase of the states. $\Phi(t)$ can also be interpreted as the total area enclosed by the trajectory of the wavepacket in phase-space. By imposing requirements at gate time τ_g onto the displacement in phase space $\alpha(\tau_g) = 0$ and the total acquired phase $\Phi(\tau_g) = \pi/2$,

$$U_{MS}(\tau_g) = \exp\left[iS^2\pi/4\right]. \tag{2.42}$$

The operation of this propagator on the two qubit ground state $|00\rangle$ gives $U_{MS}(\tau_g)|00\rangle$, resulting in an entangled Bell state $1/\sqrt{2}(|00\rangle - i|11\rangle)$. This gate can be extended to higher-order modes and higher numbers of ions, for which the mathematical derivation is omitted. By using this interaction, GHZ states as mentioned in subsection 2.1.1 can be created in trapped ion architectures.

CHAPTER 3

Experimental setup

This chapter describes a new trapped ion system's design, construction, and assembly. The system includes an ultra-high vacuum ion trap physical package that enables the co-trapping of ytterbium ions and lutetium ions, experimental control systems, and laser systems for manipulating the ions. This system offers novel capabilities beyond what is possible with the current generation of the ytterbium-only single-species trapped-ion system in the Quantum Control Laboratory.

3.1 Yb-Lu trap

3.1.1 Trap structure

The dual-species trap is a Pine trap designed and constructed by Alpine Quantum Technologies [52], as seen in Figure 3.1. The Pine trap is a Paul trap and consists of four radial blade electrodes and two endcaps. The trap structure allows for optical access every 45° in the X-Y plane parallel to the optical table. The endcaps have 0.5 mm diameter holes through the middle and there are clearance holes in the structure on the diagonal as seen in Figure 3.2. The trap also contains four pairs of compensation rod-like electrodes on which voltages are applied to reduce micromotion. Locations of the radial blades and the compensation electrodes can be seen in section A of Figure 3.3. The dimensions of the trap have to be extremely well calibrated and the trap structure is therefore machined to high precision. This ensures the trap is stable and ions can remain trapped for extended periods. The radial electrodes are 4.15 mm in length, with the endcap-to-endcap distance at 4.5 mm Figure 3.2.

The constituent materials of the trap are chosen to be ultra-high vacuum (UHV) [1] compatible and to keep the trap dimensions commensurate during preparation. The trap blades and endcaps are constructed from titanium, as it has a high electrical conductivity and can be precisely manufactured. When the system is baked out (heated) and undergoes temperature

[1] a regime of $< 10^{-8}$ mBar known as Ultra high vacuum (UHV)

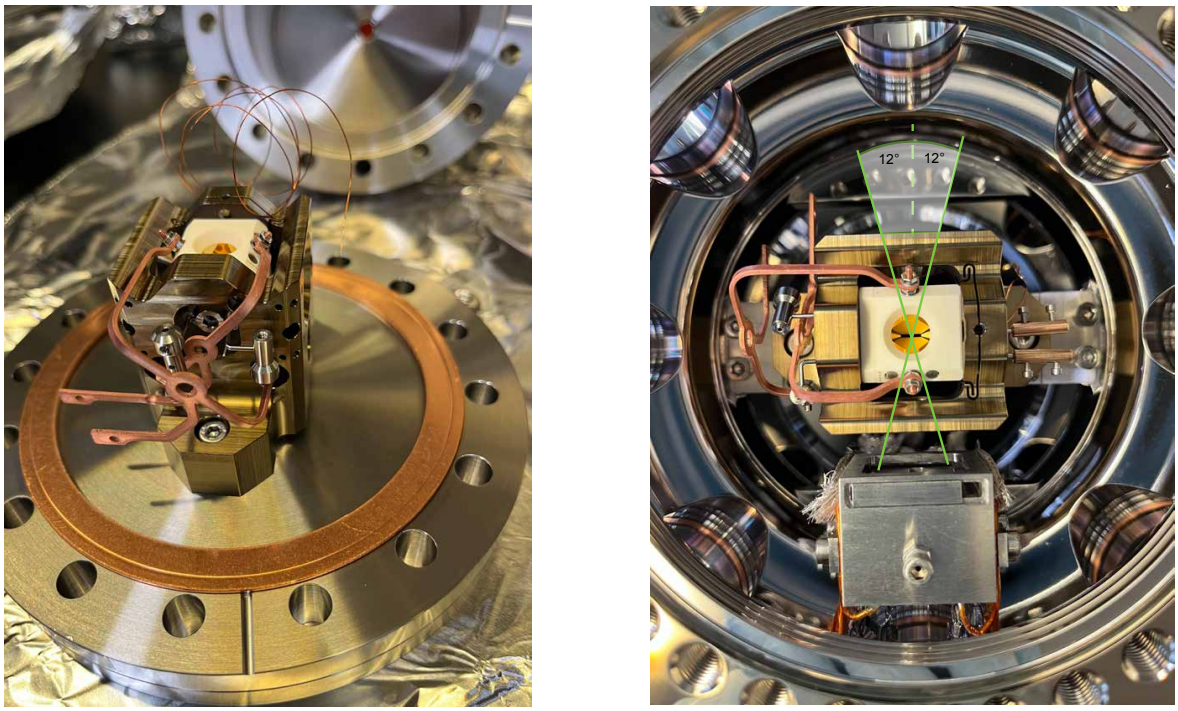

(A) AQT trap (B) Trap installed in vacuum chamber

FIGURE 3.1. Images of the AQT trap from the QCL, in **A** the AQT trap is shown before it was installed into the vacuum chamber. It is kept under nitrogen before the assembly to maintain cleanliness. **B** shows the assembled trap, with the oven holder shown opposing the radial blades. The AQT trap sits in the upper octagon of the two Kimball Physics octagonal chambers.

gradients, the trap geometry will remain precise. Each blade is also coated in gold with 1.75μm thickness, which produces a smoother surface. As a result, the gold-plated titanium electrodes have a high electrical conductivity and high work function (5.1 eV). Finally, the trap is encased in an aluminium-oxide housing, a material that is UHV compatible, has high thermal conductivity and has a similar coefficient of thermal expansion as Titanium. It also insulates the trap so that each electrode can be individually controlled. Surrounding the trap is the supporting structure, which is manufactured from AQT and contains copper wiring for RF and DC electrode access.

A radio-frequency is applied to two opposing radial electrodes to produce trapping voltage along Radial X and Y directions. The RF signal is produced by a signal generator[2], amplified by an amplifier[3] followed by a helical resonator (see Figure 3.6). The circuit can be modelled

[2]R&S®SMA100B
[3]LZY-22+ Minicircuits

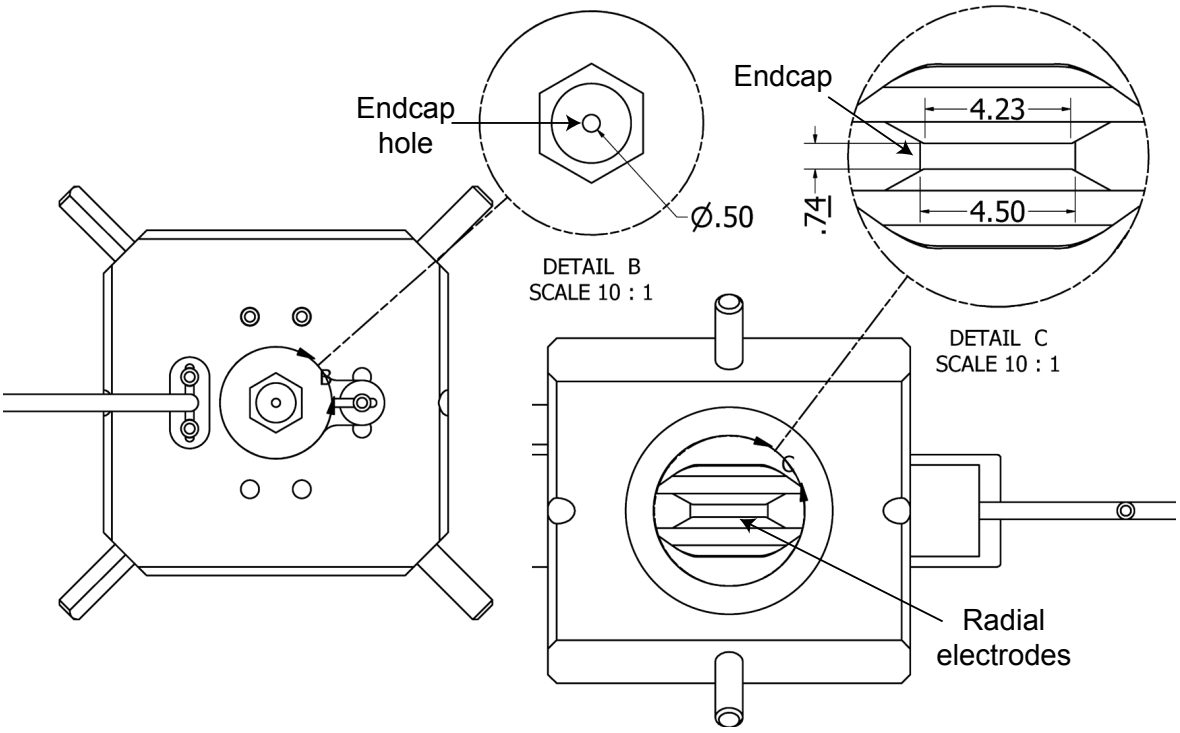

FIGURE 3.2. Front and side view of the trap. Detail B shows the endcap hole diameter for optical access. The side view in Detail C shows the length of the blade electrodes alongside the spacing between the electrodes

as an LCR series circuit with the trap blades acting as a capacitor. The other two opposing pairs of blade electrodes are grounded. The confinement along the z-axis is done by applying DC voltages to the endcap electrodes. These are produced by ARTIQ's zotino channels and amplified[4]. The details of the DC and RF/resonator setup are included in subsection 3.1.3.

3.1.2 Octagonal vacuum chamber

The Pine trap module is housed inside a vacuum chamber that can support UHV as in Figure 3.1. A lower pressure translates to a greater residual gases' mean free path inside the chamber and fewer collisions between the residual particles with the trapped ions. Collisions could lead to decoherence of the ion bosonic mode or the ion being knocked out of the potential well. Evacuating (decreasing to low pressure) vacuum chambers to UHV requires high levels of cleanliness (see Appendix section A1 for cleaning protocol) and preparation. The apparatus chosen to be evacuated is a double set of Kimball Physics octagonal chambers[5], which encloses the ion trap in this setup. This was chosen, as it allows for optical access from

[4]PDu150 Three Channel 150V Piezo Driver
[5]MCF600-SphOct-F2C8

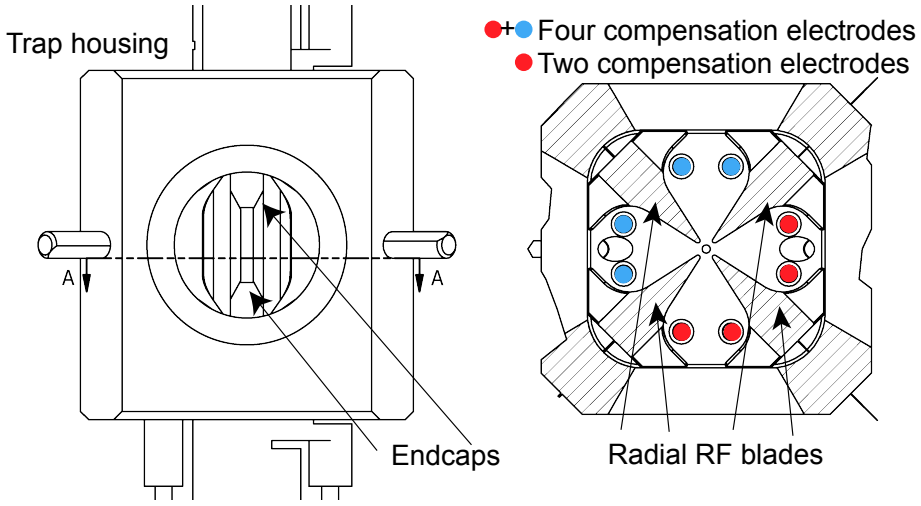

FIGURE 3.3. Section view of the trap from AQT is shown here, with the left-hand side showing the side view of the trap. The endcaps are highlighted and the line A shows the section cut axis. The right-hand side is the sectioned view, with the radial RF blades labelled. Two opposing blades are injected with the RF voltage and the other two are DC radial blade electrodes. The endcaps have a static DC potential. The two different optional configurations for compensation electrodes are shown in red and blue (four or two).

eight different angles (45° apart) on the top chamber and there are sufficient flanges on the bottom chamber for electrical access and vacuum management. It also keeps the total volume of the chamber to a minimum and has a high vacuum conductance, which can improve the quality of the vacuum as there is less area for outgassing and it is faster to pump less volume down to UHV. These two chambers are connected using a middle cylindrical piece which has threaded holes to mount parts on and can be seen in the centre of Figure 3.4.

The vacuum system components extruding from the octagons are assembled using conflat (CF) components. The viewports on the top octagon are all fused silica and CF[6], placed on each side of the top octagon. The bottom octagon contains the electrical feedthroughs, for the parts of the trap that require power, a NEXTorr ion getter and pump[7] and the valve[8] used in the bakeout process. The trap and mounting sit in the upper octagon, resting on the chamber's middle piece. The trapping location of ions will then sit in the middle of the viewport, the point at which the light transmission is maximised.

[6]Accuglass DN40CF
[7]NEXTorrr® Z-200
[8]MDC-MAV-150

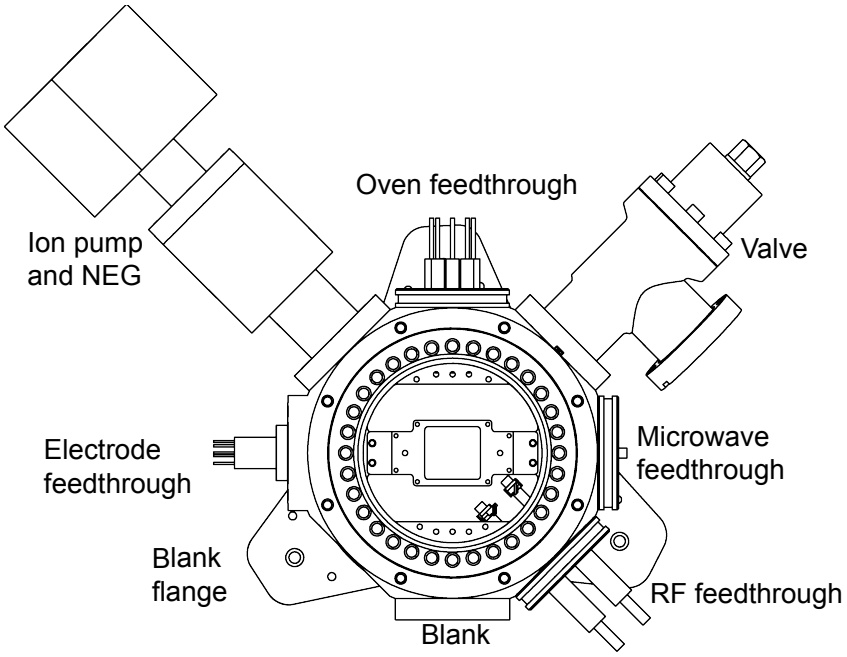

FIGURE 3.4. Bird's eye view of the bottom octagon of the trap with labels for each of the flanges. Feedthroughs are shown for the RF drive, microwave addressing, oven control and DC electrode control. The NEXTorr ion pump and getter and the valve are used for vacuum management. The mounting plate of the trap is shown here in the middle, the AQT trap slides onto it and the trap centre is in the upper octagon.

3.1.3 Electrical feedthroughs and trapping voltages

There are four sets of electrical feedthroughs for the trap. The first set is for the endcap electrodes and the compensation electrodes[9]. In the Yb-Lu trap, whilst waiting for the order of a new ISEG, a Zotino DAC channel was connected to a piezo amplifier to supply a controllable voltage source at 88V on both of the endcap electrodes. In addition to this, another channel on the zotino has a direct output to the compensation electrodes, operating at 9.9 V. The electrical feedthrough providing the eight wired connections for the ovens is detailed in Figure 3.5. There are 4 ovens in the trap and each feedthrough wire has a custom crimp contact connecting each oven. The microwave feedthrough is a single-pin SMA coaxial feedthrough and the RF feedthrough has two larger conductors to support the higher voltages required for the radial electrodes, as shown in Figure 3.6 panel **c**. In the RF feedthrough, the right-hand pin is connected to the resonator and the left-hand pin is connected to the DC output.

[9]The temperature sensors were removed after it was found to be shorting the wires for the electrodes.

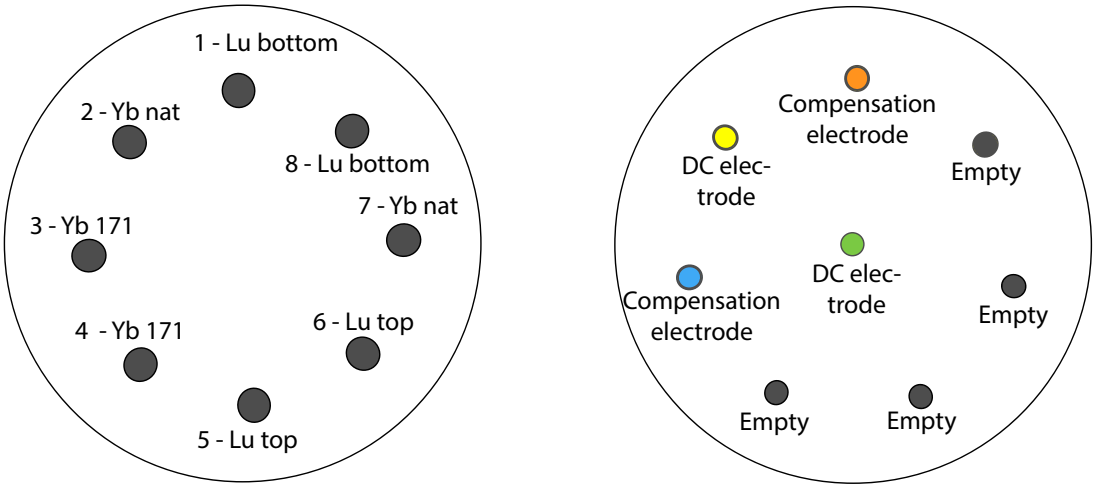

(A) Oven Mapping (B) Electrode mapping

FIGURE 3.5. Electronic feedthrough mapping for the Yb-Lu trap, showing the connections. The top and bottom $^{176}Lu^{+}$oven connections refer to the positive and negative connections to the two $^{176}Lu^{+}$foil ovens, located above and below another. The 'Yb nat' refers to the ytterbium natural abundance oven and the 'Yb 171' refers to the enriched isotope oven.

The helical resonator is impedance matched to provide the highest possible trap depth for a given RF voltage. The resonator also acts as a filter to reduce signal noise on the RF drive, with a narrow bandwidth (high Q-factor) improving the reduction [53]. Higher trap depth means more prolonged ion trapping lifetimes, however too much voltage can cause adverse effects such as sparking or instability. Conditions on resonator parameters and target peak-to-peak voltages can be found in the thesis of Matthias Brandl [54]. The design of the resonator is an iteration of the following [32]. It is constructed out of 3 mm diameter copper wire wound around a spacer inside a cylindrical can. The resonance peak of the resonator was measured at 20.53 MHz. The Q-factor Q of the resonator, a measurement of how well the resonator stores energy, was measured to be 194$\pm$14 whilst connected to the trap. Here, Q was determined with the definition $Q = \omega_r/\Delta\omega_{FWHM}$.. This measurement was performed by connecting SMA cables to the input and reflected signal of the resonator can. The other ends of the cables are connected to a signal analyser [10]. By measuring using the vector network analysis mode, an S21 measurement was completed to determine the resonant frequency ω_r and the full-width half maximum $\Delta\omega_{FWHM}$ of the resonator.

[10] FieldFox handheld MW and RF analyzer

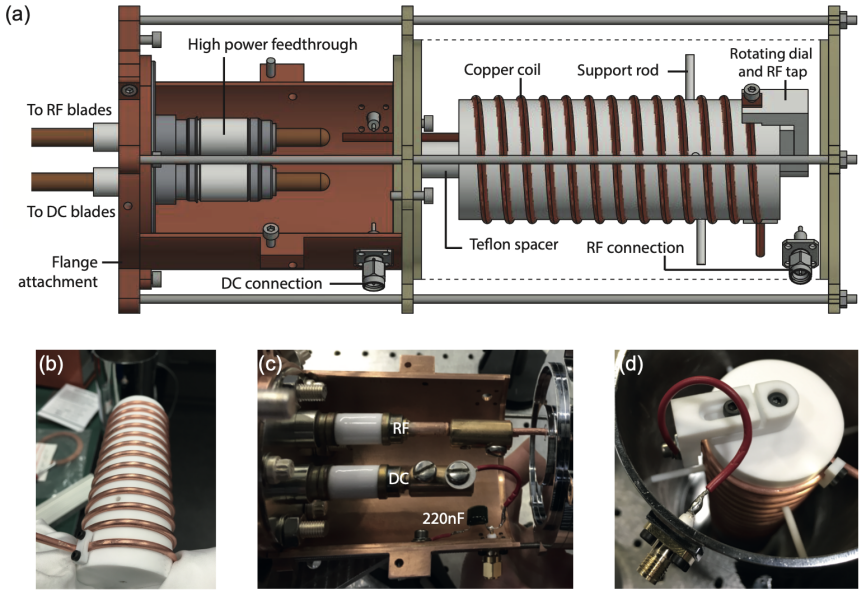

FIGURE 3.6. a). Resonator diagram showing the coil and how it attaches to the high-power feedthrough. b). Wound coil around a Teflon spacer. c). Diagram showing the RF connection using barrel connectors. d). Rotating the dial to impedance match the resonator. Image reproduced from [32].

3.1.4 Vacuum protocol

Four vacuum pumps and a large bake-out oven are used to prepare the inside of the trap chamber to UHV. The valve in Figure 3.4 is connected to a pumping station consisting of three pumps. The pumps are turned on successively to slowly decrease the pressure, and valves are closed to redundant or limiting pumps. The first pump is a scroll pump, then a turbo-molecular pump[11] and then an ion pump[12]. The turbo and ion pumps have an upper limit of pressure at which they can be activated, as activating them at ambient pressure can contaminate and increase the time taken to pump down to low pressures.

Once the system is completely assembled, the bolts holding the vacuum connections together must be tightened. These are tightened to a given specific torque for each component by using a torque wrench according to a bolt-tightening sequence[13]. This avoids over-compressing one side of the gasket and thus preventing leaks. The system is checked to ensure no loose bolts are found and then the evacuation process starts. The order of the pumps activation can be seen in Figure 3.7

[11] HiPace® 80
[12] TiTan Gamma Vacuum
[13] e.g. Legacy pattern in table 4 of [55]

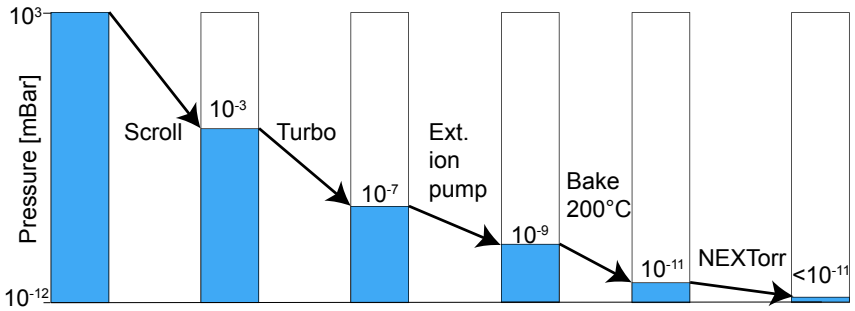

FIGURE 3.7. Graphical representation of the process required to reduce the vacuum chamber to UHV pressure. The steps are i). Scroll pump ii). Turbomolecular pump iii). External ion pump iv). Bakeout at 200° v). Activation of NEXTorr internal ion pump and getter

A minimum pressure is reached and the system is now ready for leak tests. To do so, Helium gas is injected into the weak points of the vacuum system to ensure that there are no leaks present. A rough indication that there are leaks can be seen on the ion pump, where leaking Helium will send a higher current to the pump and the pressure it calculates will increase. For a more detailed analysis of the leak, a residual gas analyzer[14] is used to verify if Helium is present in the system. Partial pressures are calculated on the analyzer by its mass spectrometer, indicating if there is a spike of Helium. If leaks are found, the bolts are further tightened and in some cases may have to be disassembled and parts exchanged.

After completing the leak testing, the bakeout procedure can commence. To prepare, the vacuum chamber is entirely covered with UHV aluminium foil[15]. This is done to avoid temperature gradients across the vacuum chamber. Additionally, foil-wrapped bricks and metal sheets are carefully arranged around the system to trap heat, while a fan is activated to circulate the air inside the oven. The bakeout procedure demands meticulous attention since a rapid temperature gradient can harm seals and lead to uneven expansion of components. Control over the oven is achieved through a Raspberry Pi running Python software, which regulates the temperature gradient by toggling the bakeout oven on and off with longer or shorter duty cycles for ramping up and down. The desired target temperature is set within the control server, and the duty cycle is restricted to a maximum of 42% as this corresponds to a temperature of 200 °C when ramped up from 0 continuously. Temperature readings are taken every minute using thermocouples attached to the trap. To ensure reliability and accurate measurements, each thermocouple has a probability of approximately 1/30 of failing to read. Consequently, two thermocouples are employed for both fail-safe purposes and to provide

[14] Stanford RGA Residual Gas Analyser
[15] All-Foils-Inc

an averaged measurement. It is important to note that the thermocouples are not perfectly insulated and must be carefully managed to prevent them from shorting against the aluminium foil or the trap.

The oven control system alone was characterised and by varying the duty cycle from 0 to 0.5, the temperature was compared after letting the system stabilise. A linear fit was taken to find the gradient of 36.3 °C per 0.1 increase in the duty cycle. Maintaining the maximum temperature change in the system below 3 °C every 10 minutes requires the change in duty cycle to be at a maximum of 10^{-4} per minute. This is set as a limit in the oven controller and when activated, the gradient is changed as such. Finally, the pressure is monitored using Grafana during the bakeout procedure, with data from a pressure gauge sent to the Raspberry Pi and uploaded to the Grafana server. This allows remote checks to be performed when the system is baking out overnight.

After successful baking and lower pressures are reached, the final step in the pumping process involves activating the internal ion pump and getter. Firstly, the ion pump is flashed on and off and then the getter is activated by supplying a high voltage, as the non-evaporable materials in the getter only develop pumping characteristics after heating under vacuum. After activating the NEG, the internal ion pump can be turned on and left in operating mode.

The valve connecting the trap to the pumping station can be closed and the valve[16] in the Yb-Lu trap is sealed with 10.5Nm of torque using a torque wrench and disconnected from the pumping station. Upon bakeout on the Yb-Lu trap and activation of the internal ion pump and getter, UHV pressures were achieved. However, when the system valve was closed and the trap separated from the pumping station, the pressure was not maintained. This was due to the leak rate through the valve being too high for it to be compensated for by the ion pump. Therefore, when disconnecting the pumping station, the increased pressure gradient caused a higher pressure ($> 10^{-11}$ mBar) to become the equilibrium point. To maintain the low pressures in all vacuum systems, the leak rate must be less than the rate of absorption from the ion pump.

As a result of faulty valves and shorting temperature sensors, the trap had to be vented and components replaced or removed. Speeding up this process can be achieved by venting the system with Nitrogen. As the system is being vented out, the HiPace turbo pump was configured to vent with Nitrogen instead of air. The trap is coated with Nitrogen before being exposed to air, reducing the pumping time in the following pumps.

[16] MDC-MAV-150

Combining the pump and bakeout procedure on the Yb-Lu trap, a pressure of $< 10^{-11}$mBar was achieved. This pressure is calculated from the ion pump reading of 0nA where it has a resolution of 5nA. The pressure reading is therefore at a minimum and the trap is at UHV.

3.1.5 Microwave antenna design

Addressing the hyperfine levels can be done using microwave fields at the resonant transition frequencies and antennas are placed in this trap to drive the transition directly. A magnetic field of microwave radiation $B(t)$ will interact with the ion $H = -\vec{\mu}.\vec{B}(t)$, with $\vec{\mu}$ being the magnetic moment of the ion. Ytterbium has a hyperfine splitting of 12.6 GHz and lutetium has two addressable hyperfine levels with splittings of 10.6 GHz and 11.3 GHz respectively. As a result, the antenna must have a bandwidth that encompasses these transitions so that each transition can be driven. The wavelength of these waves is large and individual ions cannot be driven in isolation as such microwave transitions are used for the characterisation of global operations. Horn antennas are often used in ion traps to generate microwave fields, however, due to the trap constraints this would mean placing the antenna below the trap, attenuating the field. Due to space constraints, a loop antenna was characterised and placed inside the vacuum chamber. The loop antenna has a diameter of 2.37 cm and can be seen in panel **a** of Figure 3.9. The conductor is made from stripped-back coaxial which is then spot welded onto the outer conductor of the coaxial cable. The spot weld is made using a piece of tantalum foil to secure the outer conductor. The wire chosen is cleaned and vacuum-compatible Kapton insulated 26AWG wire[17]. It has one SMA connector end to connect to the electrical feedthrough. To fit the loop wire to the desired dimensions, a mould was designed and 3D printed. The wire is placed inside and then clamped down, ensuring that the loop antenna has the correct diameter and shape and that there are no electrical shorts.

After the loop is made, it must be placed as close to the trapping location as possible. This has some natural difficulties, as the ion trap chamber itself comes prefabricated. The microwave loop could have been mounted in a similar way to the ovens, but this would have led to loose wires which during the translation process can block optical access. To place the loop as close to the trapping location as possible, a holding structure was placed on the bottom of the AQT trap which clamps onto the wire securing it in place. The holder hooks onto holes in the trap structure with a saddle-like fit and the technical drawings are shown in Figure 3.8. The bolts hold the microwave holder onto the trap and the mounting structure has vents to ensure no trapped air is held inside the mount. To hold the antenna wire, there are two tapped holes which hold the wire into a groove. The microwave holder has M2 screws for mounting onto

[17] Accuglass part number 110755

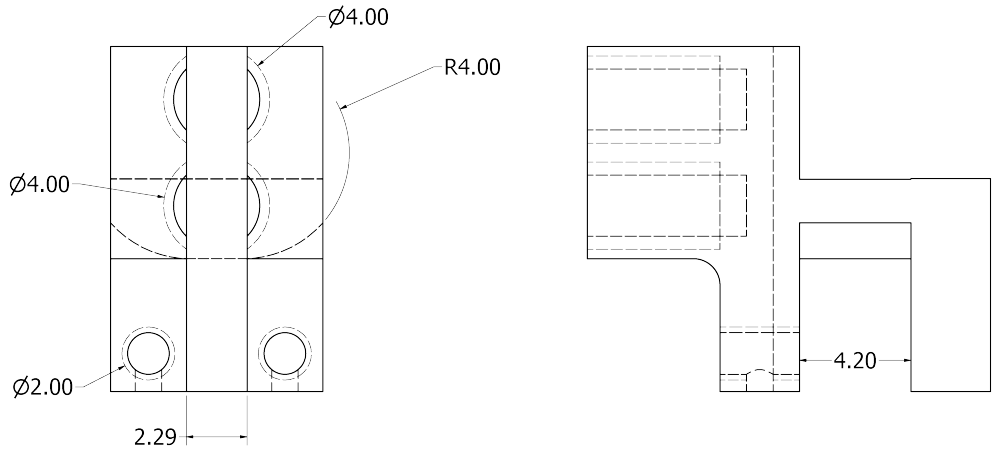

FIGURE 3.8. Microwave holder dimensions, showing the saddle-like design with a radius of 4 mm (fits onto the AQT trap base) and the vented holes for securing. Also, the groove for the 26AWG wire is shown, with the two M4 threaded holes to place setscrews and lock the wire into place.

the trap structure, and two M4 setscrews lock the wire into place. As the wire is 26AWG, the distance between the two sides of the wire clamp is 2.29 mm.

Once mounted in the holder, the microwave antenna is then located 21.1 mm away from the trap centre. High-frequency structure simulations (HFSS)[18] allowed investigation of the optimal location of the antenna, using an excitation on a thin circle as the microwave source as shown in Figure 3.9. After construction and analysis of the bandwidth, the antenna was installed in the trap and outgassed during the bakeout process.

3.1.6 Ovens

There are four sets of atomic ovens in the Yb-Lu trap: two for lutetium for redundancy and two for ytterbium. The ytterbium ovens differ by the isotopes loaded, one with natural abundance of ytterbium and one with enriched ^{171}Yb isotopes. The ovens work on the principle of resistive heating; by applying a current it can provide a sufficient temperature increase to produce an atomic flux. Their locations relative to one another can be seen in Figure 3.10. The atomic flux, if directed towards the trap, will cross the ionisation beams and then move into the trap. In Figure 3.12, the atomic flux from the natural abundance oven is shown to fluoresce with 399nm light as it passes through the trap.

[18] ANSYS HFSS

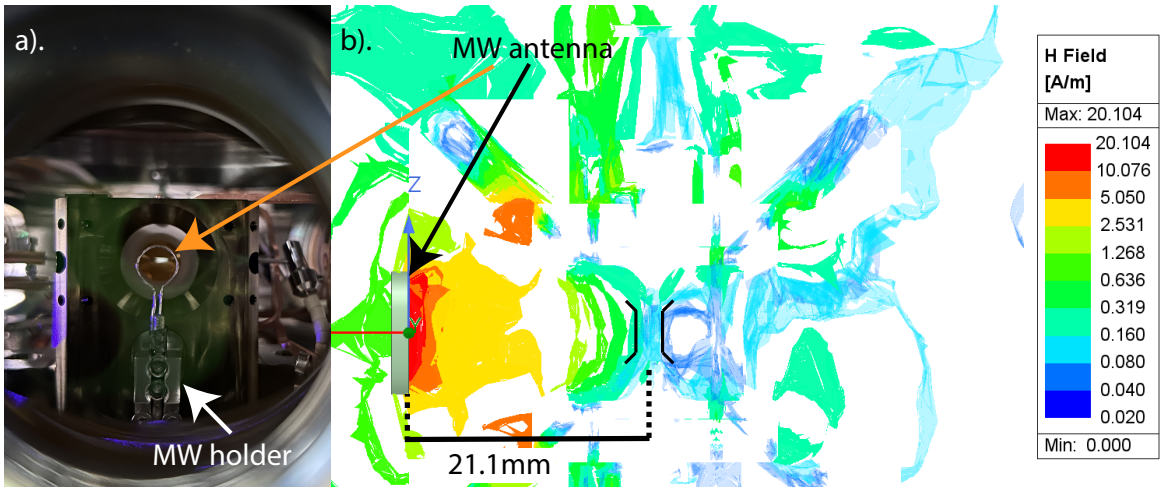

FIGURE 3.9. a). The mounted antenna on the AQT trap, with set-screws holding the coaxial cable in the microwave holder. The image is looking through one of the radial viewports. b). HFSS simulations of the microwave antenna with the entire trap housing from AQT. The trap centre is marked by the black lines in the centre of the plot. The trap architecture heavily attenuates the field, so the antenna placement is required to be as close as possible to the trap centre.

All four ovens are contained in the same holder, on the opposing side of the blades to the microwave antenna. The aluminium external holder is screwed in on top of the support ring in between the two octagons. It has two legs and extends into the main body, consisting of a sliding door, with the Macor internal holder and the ovens enclosed inside. The external holder is shown with the sliding door in Figure 3.11. The door is added to the design and is slid open and closed by rotating the system gently. The door is kept in the closed position (as in panel **b**) during the bakeout procedure to prevent the trap from being coated with atomic flux.

Several factors need to be considered when designing an oven, such as preserving optical access through the trap, avoiding electrical shorts between each oven and the external holder, and ensuring that each oven has enough current for atomisation. To address these concerns, a custom-designed Macor internal holder (Figure 3.10 panel **a**) with eight holes around a larger optical access hole was designed. The centre hole extends a few millimetres towards the trap to provide space for the ovens to sit without electrically contacting the external holder. The ovens are mounted on the front face, with the ytterbium ones angled towards the trap centre, while the lutetium ones are a foil. The ytterbium ovens have a 12° angle with the perpendicular vector of the blade.

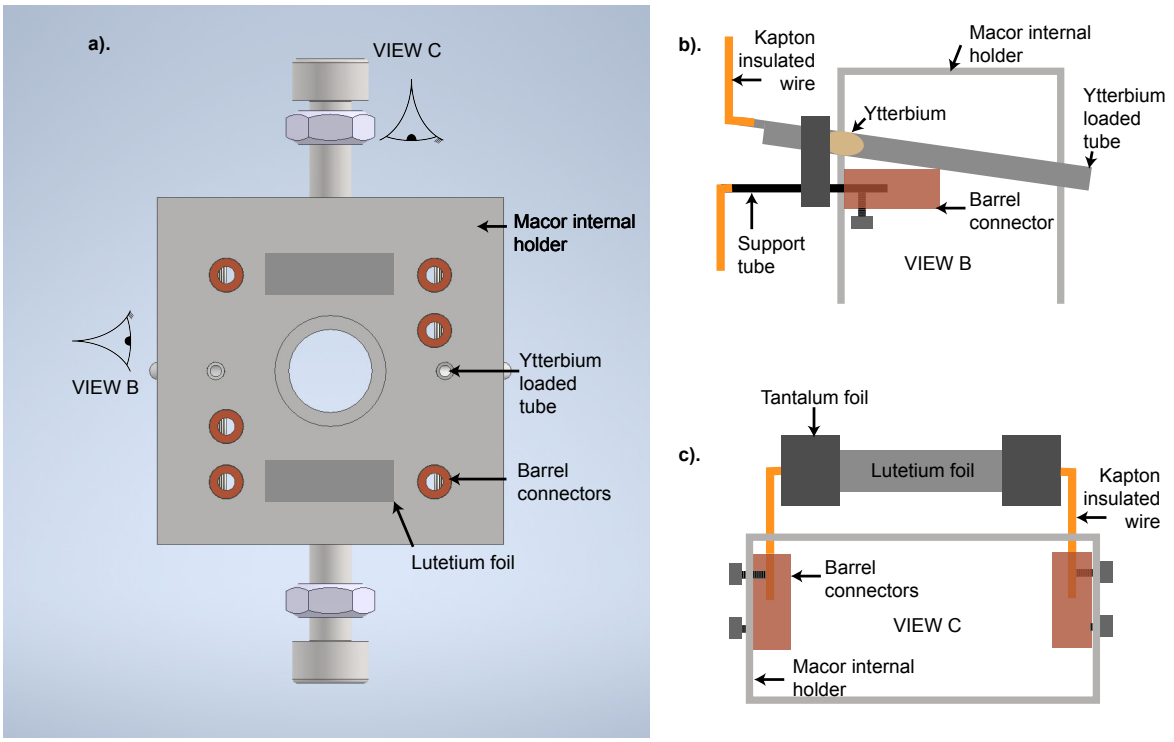

FIGURE 3.10. Description of oven locations along with their construction in the internal macor holder. **a** shows the front view of the macor holder, where the top and bottom lutetium foil ovens are shown along with the two left and right ytterbium loaded tube ovens. The final internal holder design was designed by Dr. Tomas Navickas. **b** is a side view from B, with the ytterbium ovens. Tantalum foil connects the ytterbium loaded tube (one end crimped) to the support rod. Current passes through the support tube and resistively heats the ytterbium tube, producing an atomic flux. **c** is a top view of the internal macor holder, demonstrating the lutetium foil oven construction. Tantalum foil is spot welded on the lutetium foil, connecting the foil to the Kapton insulated wire. This is then mounted into the front face of the internal holder by the barrel connectors.

The ovens have a lifetime as there is a finite amount of material and if heated too strongly, the ovens can burn out. A timing circuit using a relay is applied to the TENMA programmable power supply to provide cutoff switches to the oven current. There are two power supplies, one for each species. These are controlled in ARTIQ using the 'automated loading scripts' and if the TENMA power supplies malfunction can be deactivated using the 'force stop loading' scripts. The Yb ovens are made from a needle tube, with one end opened and the other crimped as shown in panel **b** of Figure 3.10. Tantalum foil and spot welds make the electrical connections to the ovens. Yb, either natural or enriched, is stuffed inside the tube. When the tube is resistively heated, if heated up to the Yb evaporation temperature of 253°C then atomic

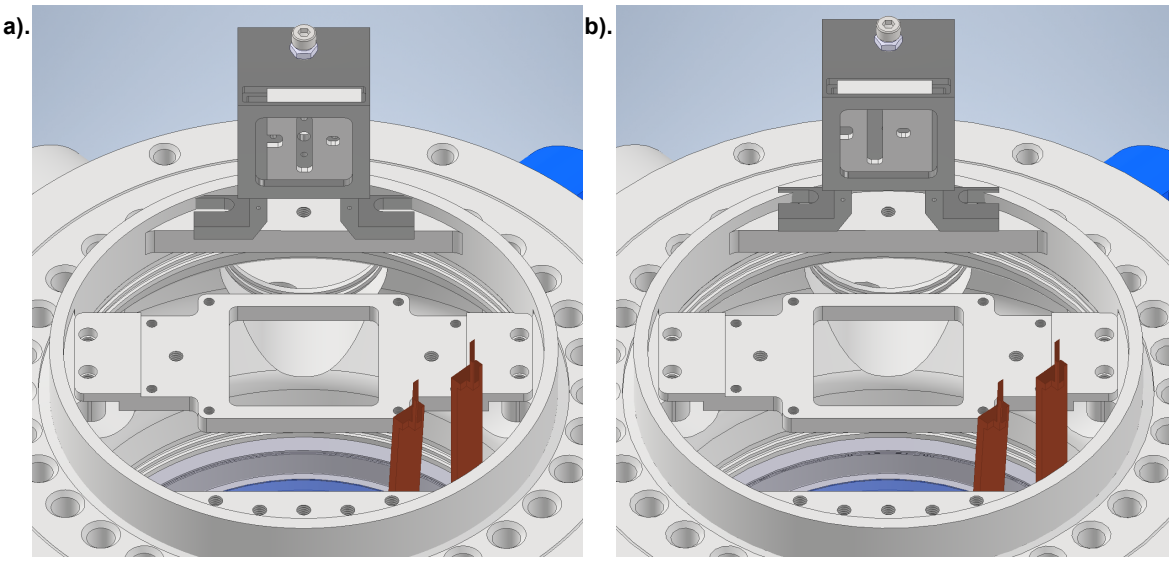

FIGURE 3.11. **a** Oven external holder, machined in aluminium and mounted on the support ring. The macor oven from Figure 3.10 is mounted inside. The sliding door piece blocks the ovens, **b**Same diagram showing the sliding door in the blocked position, preventing the oven flux from coating the trap during the bakeout procedure.

flux will exit the tube towards the trap. The resistance of the Yb ovens is for natural 0.7Ω and for enriched 0.3Ω. The power $P = I^2R$ determines the applied heating. Fluorescence is observed on the natural ovens at 8A, and to apply the same power to the enriched would require 4.7A. The lutetium ovens consist of a foil, 0.001in thick with spot welded Tantalum connections to 20AWG wire on each side as shown in panel **c** of Figure 3.10. Each wire for the lutetium and ytterbium ovens is cut short and connected to a terminal connector, embedded into the Macor holder. This takes the strain off the ovens when the ovens are bent so that they don't break during the construction process. Each wire is custom-made and is thermally isolated by placing ceramic beads and covering them with an insulating sheath.

3.1.7 Imaging system and Shim coil

Light emitted from the ions during the detection protocol must be collected to detect their state. Photons are emitted isotropically from the trap centre and the imaging system design must be optimised to collect as much light as possible. The numerical aperture of the trap is 0.5, however, this is not circular as the compensation electrodes on top of the trap block some light. Considering these, the NA that is circular is 0.2. The light coming from this top viewport is then collected by a composite lens called the objective. It is then focused down onto an avalanche photodiode (APD) or an electron-multiplying charged coupled device

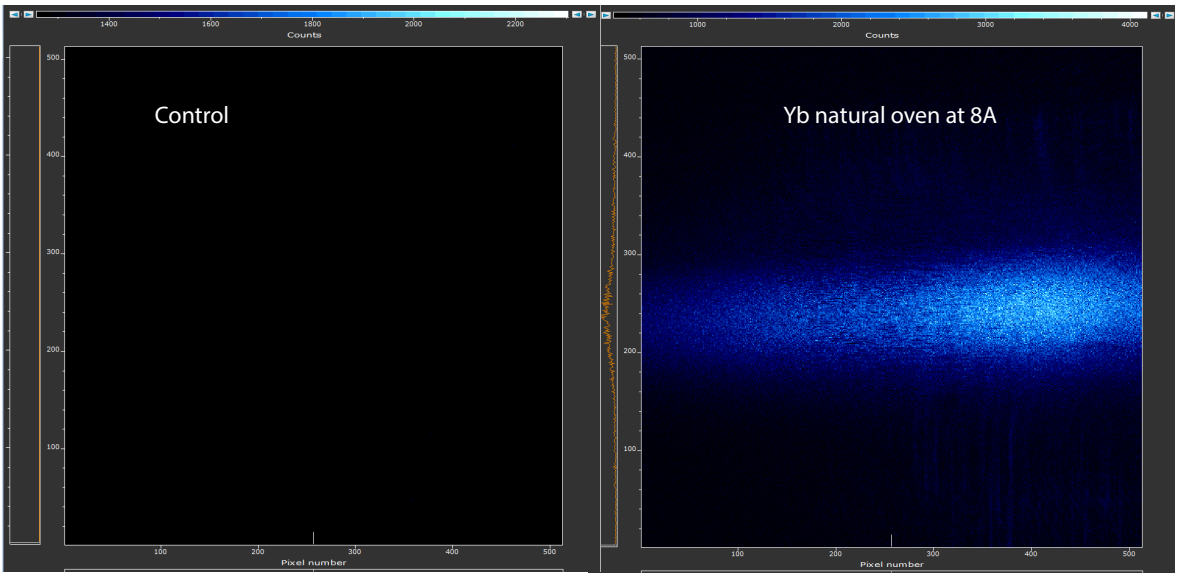

FIGURE 3.12. The two figures show the EMCCD image taken firstly when the oven has no current supplied and in the right panel the ovens are turned on at 8A. The atomic flux crosses the 399nm ionisation beam and the fluorescence at 399nm is imaged on the camera.

(EMCCD). The magnification of the system is calculated by the effective focal length of the objective 16.7 mm and the focal length of the singlet lens 400mm used to focus the light onto the detection instrument. The magnification M is therefore

$$M = \frac{f_e}{f_o} = \frac{400\text{mm}}{16.7\text{mm}} = 23.95\times, \tag{3.1}$$

where f_e, f_o is the focal length of the singlet and objective respectively.

For ytterbium, the light emitted during the state-dependent fluorescence measurement is 369 nm. A 369 nm band-pass filter (BPF) is placed in front of the EMCCD and APD to minimise background scatter which would affect the measurement fidelity. This was replaced with a 399 nm BPF to do ion fluorescence measurements during the initial trapping runs of the system. Confirmation that the Yb ovens were operating and producing atom flux was achieved on the EMCCD, along with the correct photo-ionisation frequency as seen in Figure 3.12.

Magnetic fields need to be applied on the ion to break the degeneracy. This is typically done using magnetic coils placed at the side of the trap. Once a Magnetic field is applied, other coils are also required to compensate for Earth's magnetic field and any stray field originating from other equipment or environment. The latter coils are known as shim coils and a holder for this coil was designed to be placed on top of the trap. This holder consists of a ring with 11 coils, where from the equations for magnetic field B at distance $D = 48$ mm from the

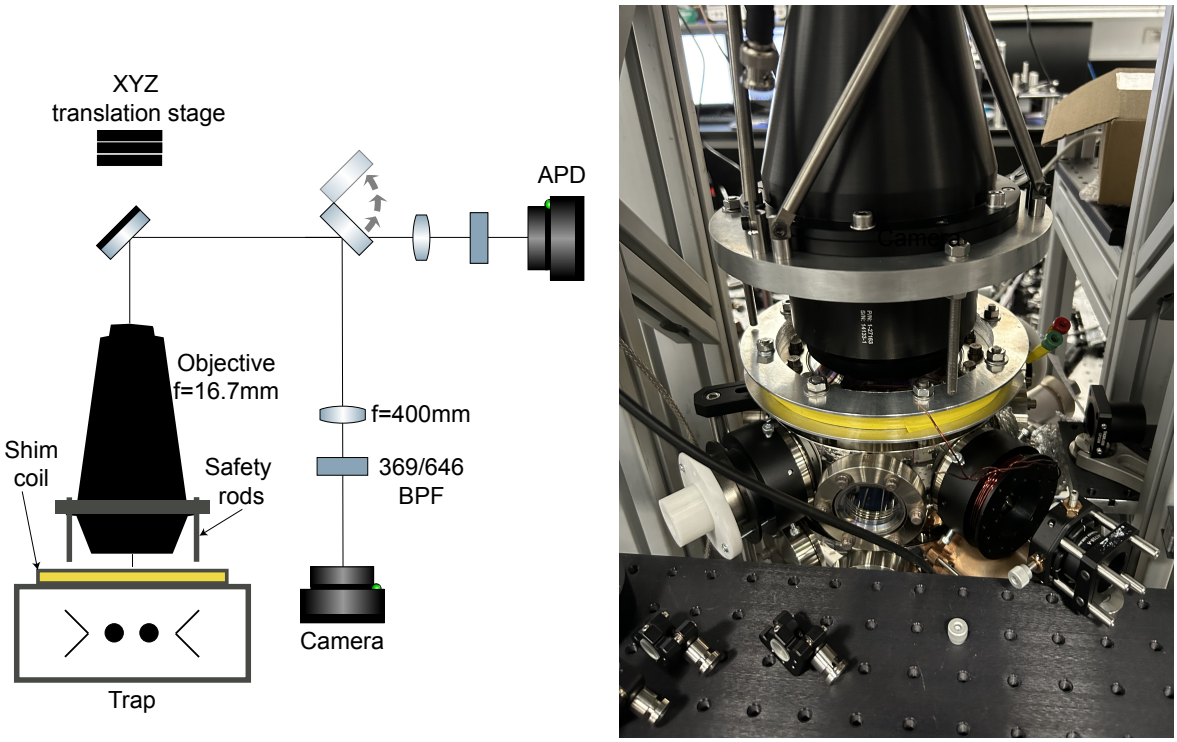

FIGURE 3.13. Imaging system simplified layout. The objective is hung from the translation stage and can be adjusted to focus on the ion plane. The trap sits on the optical table and is independent of the imaging system. Safety rods are attached vertically down from the objective to strike the shim coil and protect the top viewport from damage. The shim coil is placed and mounted on top of the trap structure.

edge originating from a solenoid length $L = 16$ mm

$$B = \frac{\mu_0 I n}{2}\left[\frac{D+L}{\sqrt{(D+L)^2+R^2}} - \frac{D}{\sqrt{D^2+R^2}}\right], \tag{3.2}$$

with $R = 88$ mm as the radius of the coil, n number of coils per meter and I the applied current through the coil. The magnetic field range at the ion can vary between 4.72 mG-9.4 G, if the current supplied varies between 0.001-2.0 A. This allows for sufficient control so that the external magnetic field can be nullified in this direction.

The top shim coil also acts as protection for the trap, as the objective hangs over the trap top viewport. If the objective were to fall, the trap viewport would break and could cause damage. As such, supporting posts are built into the magnetic field coil so that if the objective were to fall, the supporting aluminium objective ring would be caught on the posts and it would prevent damage.

3.2 Laser systems

3.2.1 369

The 369 laser is used frequently in ytterbium for the following: ion loading, Doppler cooling (DC), state detection (SD) and optical pumping (OP). As the lasers are competing for space on the optical tables, 1/2" optics were used to minimise the space required. Once trapped, the frequencies required for resonance on the ${}^2S_{1/2}\,|F=1\rangle \leftrightarrow {}^2P_{1/2}\,|F=0\rangle$ transition for ${}^{171}\mathrm{Yb}^+$ is 811.28905 THz and for ${}^{174}\mathrm{Yb}^+$ 811.29164 THz. The length of the 369 beam path was minimized, such that all optics could fit on a single breadboard (Figure 3.14). The light is emitted through the laser head and goes through the optical isolator, which prevents reflected beams from going back into the laser head. After some polarising optics, it then goes through a polarising beam splitter (PBS) which picks off the light to send to the cavity and wavemeter for locking and frequency measurements (see Figure 3.15). The transmitted light then goes to another PBS, splitting the paths for DC and OP/SD. The DC path consists of an electro-optical modulator (EOM) to add 14.74GHz sidebands to the 369nm light, preventing trapping in ${}^2S_{1/2}\,|F=0\rangle$ during the DC process. It then goes through an AOM, where the first order is used for Doppler cooling. The lack of frequency shift in the zeroth order then acts as an extra cooling beam and is activated to recrystallise the ion if it is heated due to collisions. Both beams are overlapped and coupled into the fibre to the trap. The OP/SD beam path is similar, with the OP coming from a pick-off from the first AOM and SD coming from the second. For the DC/OP/SD beams, the AOMs act as a fast switch and provide the necessary frequency shifts to drive each operation. These beams are overlapped and then further overlapped on the 399 nm beam with a dichroic. The 399nm beam is overlapped with the 369 nm to ensure that it remains aligned with the ion's position, as the 369 nm can easily be aligned using the ion's fluorescence.

3.2.2 Frequency stabilisation of 369

The 369.5 nm laser that is used for trapping and ion operations must be frequency-locked. A portion of the light is sent to a hemispherical locking cavity[19] of length 100 mm and the radius of curvature of one of the mirrors being 500 mm. To lock the laser, the reflected signal from the cavity is focused onto a high-speed photo-diode (PD) [20] which is then sent to a Pound-Drever Hall (PDH) locking module[21]. This module has two outputs; an RF signal

[19] Stable Laser Systems, Boulder CO, USA
[20] PD-AC1000-Si
[21] Qubig Q-driver 1-200 MHz ADU EOM Driver + PDH Module

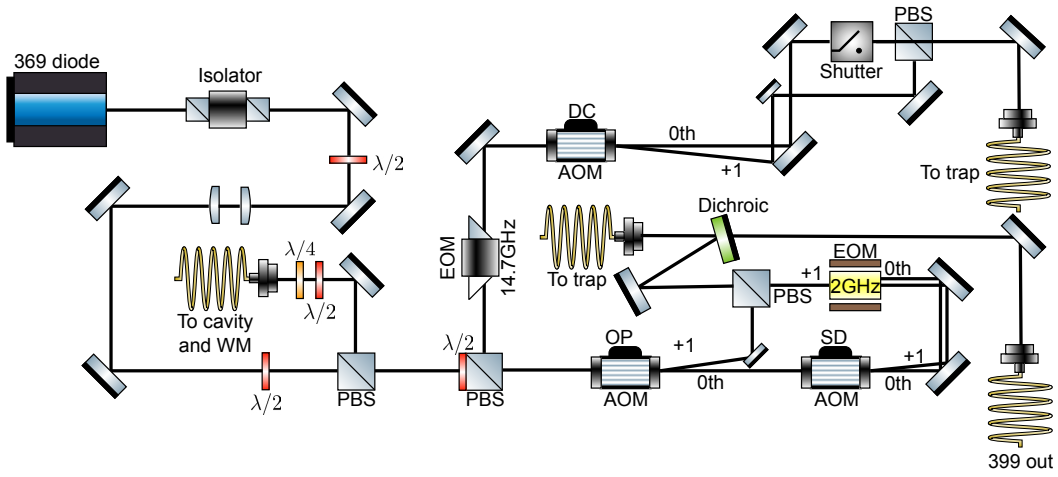

FIGURE 3.14. The laser beam path for the 369 nm laser, showing the splitting to create the optical pumping (OP), state detection (SD) and Doppler Cooling (DC) pathways. $\lambda/2$ indicates a half-wave plate and $\lambda/4$ a quarter-wave plate. PBS refers to polarising beam splitters which split the beam into separate paths. WM is the wavemeter, used to measure the frequency of the light. EOM is the electro-optic modulator which adds two sidebands at 14.7GHz.

to the EOM which gives the incoming beam optical sidebands and an error signal which is sent to the external cavity diode laser (ECDL) controller, applying frequency changes to the ECDL. This in turn provides a complete locking circuit, stabilising the frequency to be used for trapping.

After locking the frequency, the Fabry-Perot cavity length can be adjusted slowly by shifting the voltage control on a USB3105 controller. The voltage output is connected to the cavity allowing the length to be changed via a piezoelectric actuator. This in turn allows for finer control of the locking frequency after the laser is locked.

3.2.3 399

The 399 laser is used in the ionisation process of neutral ytterbium atoms. This frequency is set by the experimental results for fluorescence and each isotope was individually resolved by scanning the peaks and observing the maximum fluorescence. The ionisation frequencies for 174 and 171 are 751.5264 THz and 751.52728 THz respectively howeever can deviate due to wavemeter uncertainty. The beam path is illustrated in Figure 3.15, with a PBS splitting the paths for the light sent to the wavemeter and to the trap.

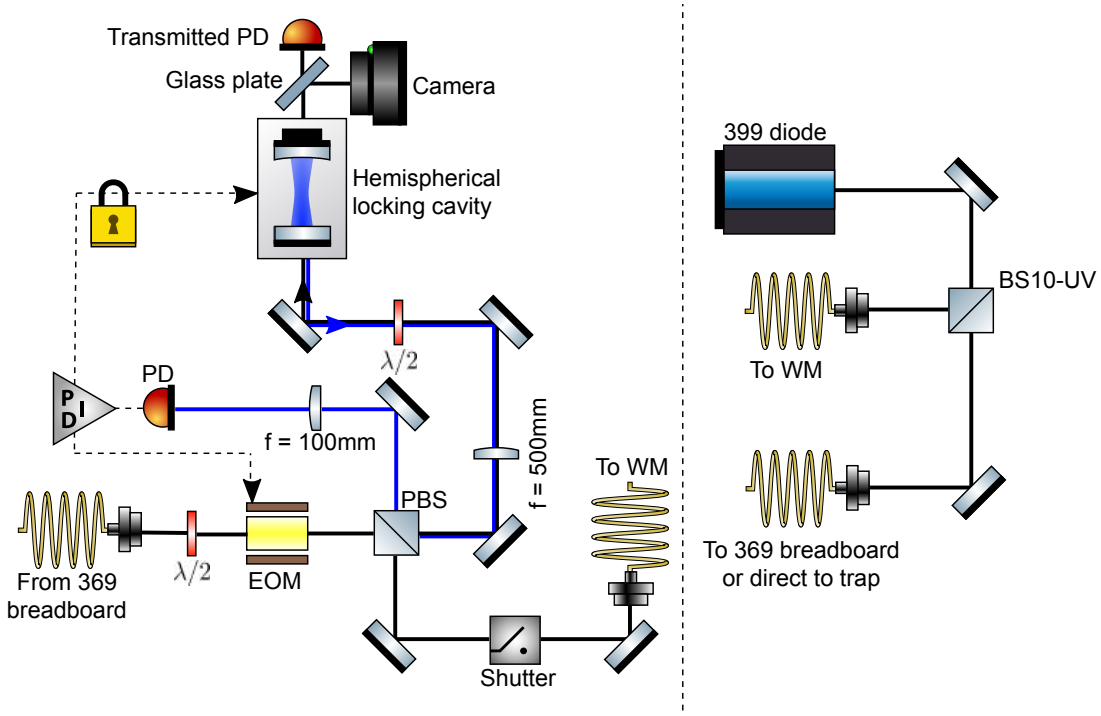

FIGURE 3.15. Optical breadboards for the 369 nm cavity PDH locking and the 399nm ECDL. The 369 cavity light comes from the first PBS in the 369 breadboard and is sent into the circuit. The hemispherical locking cavity has a length of 100 mm and a radius of curvature of 500 mm. For the 399, the ECDL is sent into a PBS which is simply split to the wavemeter for frequency tuning and the other path is sent towards the 369 breadboard. This is to overlap the 399 light with the 369 light, to ease beam delivery at the trap.

3.2.4 451

The 451nm laser is used for photoionisation of lutetium and the beam path is similar to that of the 399 nm, illustrated in Figure 3.16. To further minimise the amount of space required on the optical tables, given that this laser is not used apart for loading, it is placed inside a modularised rack and set above the optical tables, where the electronic components are stored. The rack consists of two sliding breadboard trays, on which lasers can be mounted. This has certain downsides in terms of stability and access however saves significant space by not including the laser on the same breadboard as the ion trap.

3.2.5 Trap laser orientation

Beams entering the trap have specific requirements and require optics to control the exact location. As there are eight viewports, there is ample space for beam entry. In the Yb-Lu

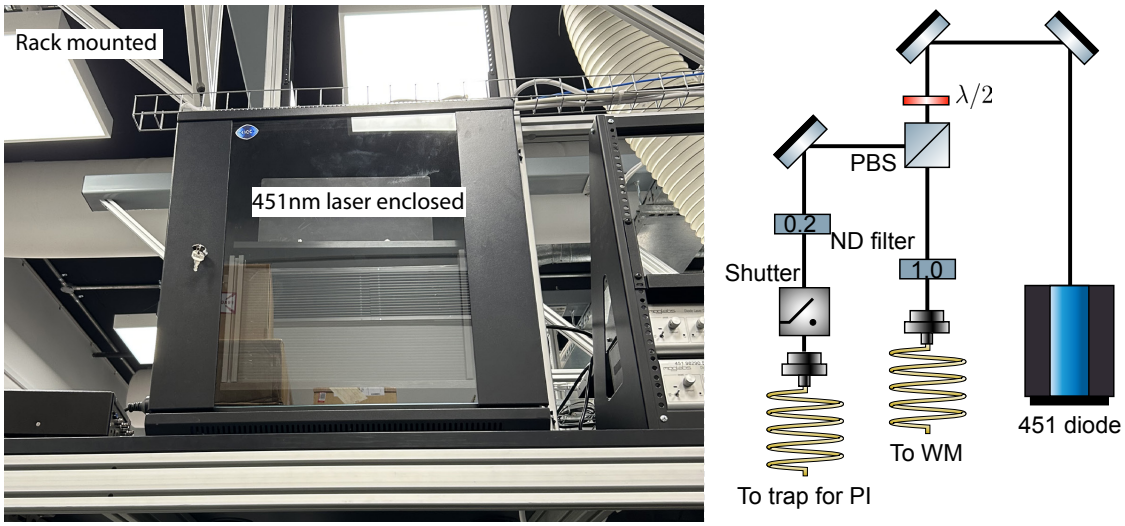

FIGURE 3.16. Rack mounted setup for 451 and laser beam path for 451. The rack-mounted setup has a similar frequency stability to the optical tables and for unlocked lasers can be an efficient way to minimise. ND filters are used to lower the power into the fibres to prevent wavemeter damage.

trap, there are a lot of lasers required for full control and so this space must be managed. The breadboards around the trap at the top octagon provide the basis for beam alignment and any further overlapping. Each beam should strike the ion plane and optical alignment techniques are critical. A number of strategies to align the beams were developed and employed to prepare the system for operation. To start, identifying the beam striking the blades and then maximising the power exiting the trap can serve as a beneficial rough alignment method. Further alignment to ensure that the beams are parallel to the table can be done using custom-made viewport mounts. These mounts are bolted onto the viewport in question and then cage rods [22] are attached to the viewport. Then, irises or lenses can be mounted onto these holders. After placing an iris on either side of the viewport (entry and exit of the laser), optimising the beam throughput the laser can be aligned to be exactly through the trap in the desired angle by slowly closing the iris.

The beams through the axial direction require greater precision as the holes for beam access through the endcaps have a diameter of 0.5 mm. Focusing optics were employed to narrow the beam size. 399 nm through the endcap is focused using a $f = 150$ mm lens mounted on an XY translation stage and the 935 has a $f = 200$ mm lens on two dovetail stages. The beam entry for each laser is as detailed in Figure 3.17.

[22] ER rods Thorlabs

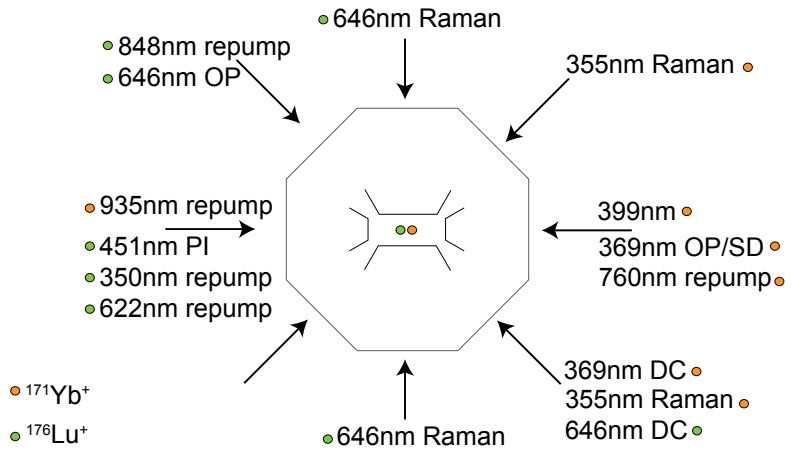

FIGURE 3.17. Beam orientation for addressing with a bird's eye view of the trap. The key with the coloured circles shows the ion species addressed by the laser type. PI stands for photoionisation, OP optical pumping, DC is Doppler cooling, the Raman interaction lasers come in a pair and all lasers labelled with repump are involved in repumping to the qubit state.

3.3 Conclusion

After construction and laser alignment onto the trap centre, ions were trapped in the Yb-Lu trap. This confirms that the construction and vacuum are up to standard. The $^{171}Yb^{+}$ ion can stay in the trap for greater than a week with the addition of Doppler Cooling, meaning the trap depth is high enough and the heating rate low enough to ensure the ion is stable. After days, the ion will 'boil' out, when collisions cause the ion to stray outside the stable trapping region. Both 171 and 174 isotopes of ytterbium were trapped and the images of the ions are shown in Figure 3.18a and 3.18b. For the 174 isotopes, the loading times were greater, leading to large clusters of ions being trapped. In the case of the 171 isotopes, the oven loading times were optimised so that only one ion was selectively loaded and the ion was left with the Doppler Cooling beam activated to test the trap efficiency. Looking forwards, the lutetium ovens and ionisation/cooling lasers should be tested to see if the lutetium ions have similar trap stability properties.

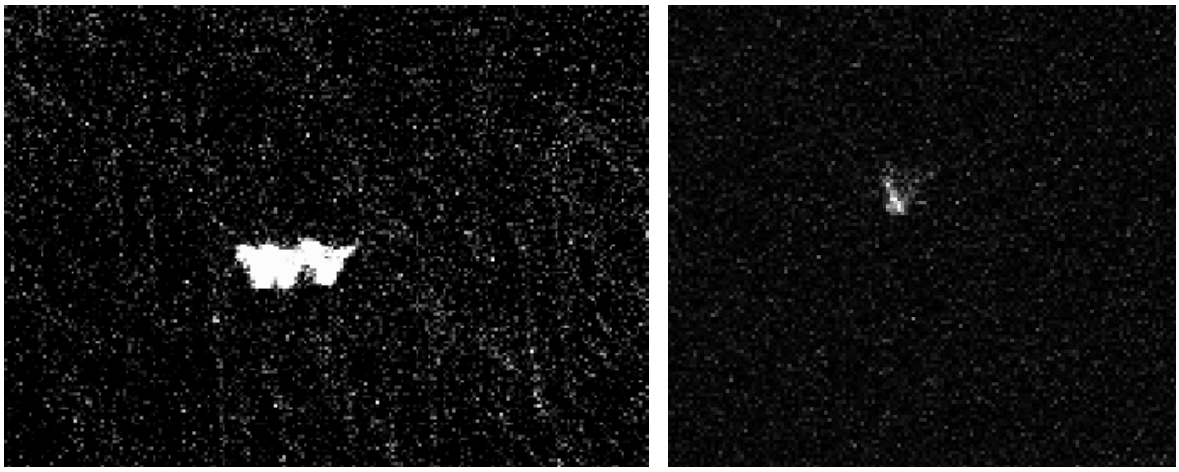

(A) Trapped 174 ytterbium ions, imaged on the Andor camera

(B) Singly trapped 171 ytterbium ion, imaged on the Andor camera

FIGURE 3.18. Ions trapped on the newly constructed system, illuminated by the 369 DC beam and fluorescence collected by the objective imaging system onto the Andor EMCCD camera. The ions are not as clear as the Yb trap as the images were taken before optimisation of the imaging system.

CHAPTER 4

Entangling gates

Entanglement is a fascinating aspect of quantum mechanics, provoking intense debate between prominent physicists about its implications in the world of physics. The famous Einstein-Podolsky-Rosen paper [56] raised concerns about the completeness of quantum mechanical descriptions given the 'spooky' nature of entanglement. Erwin Schrödinger coined the word entanglement in 1935 [57] to describe particles which have left 'remnants on one another', via some form of interaction. This interaction plays an integral part to quantum information processing (QIP), as its unique nature is harnessed for quantum information and communication. Therefore, the preparation of entanglement with high fidelity has been at the forefront of QIP research for years.

Entangling gates are readily implemented in trapped ion computers, possessing the leading two-qubit fidelity out of the quantum architectures [8, 58, 59]. This chapter focuses on their function in the Yb trap. Enacting entangling gates in trapped ions requires frequent calibration, precise timing, and consistent phase control. Advanced Real-Time Infrastructure for Quantum physics (ARTIQ) [50], a novel high-speed control system, was implemented into the existing Yb trap to facilitate these better gates. All the source code was written in Python with C++ wrappers, meaning that the experiments and datasets can be optimised entirely for ion trapping and system relevance. This provides scalability benefits because the source code is edited to accept any number of ions and complete calibrations depending on the number of modes. The entire architecture of this system was meticulously translated from the IGOR software environment to the ARTIQ framework, thereby improving the phase control and flexibility of the experiments. Duke-ARTIQ-Extensions (DAX) [60, 61], an add-on to the standalone framework, was also implemented in the Yb experiment, providing extra flexibility for scheduling and modularisation of code.

Here, the discussion of entangling gates begins with an updated description of the experimental coordination of the control software and then delves into the calibration and execution of primitive gates. Thereafter, an investigation into modulation schemes is presented, with

comparisons drawn between phase modulation, multitone gates and amplitude inhomogeneity in producing large-ion entangling gates.

4.1 Setup

The trap system must be extensively prepared and calibrated to ensure that the entangling gates operate with the highest fidelity possible. In this section, the components and procedures necessary to perform a high-fidelity MS gate are outlined, along with improvements made to the Yb trap. The gate setup process involves calibrating laser frequencies, Rabi frequencies, Avalanche Photodiode (APD) or Electron-Multiplying Charge-Coupled Device (EMCCD) detection, beam alignment, and precise adjustment of the gate parameters. The workflow for calibrating the primitive MS gate is presented in the following.

4.1.1 ARTIQ and workflow

ARTIQ is a control software created to manage hardware involved in the operation of ion trap experiments. Experiments require vast amounts of TTLs, DAC channels, DDS, AWG, etc. and interfacing exact timing between independent hardware sources can be challenging. Together with ARTIQ-centred Sinara hardware, the integrated software-hardware package provides a solution with sub-microsecond latency and nanosecond timing resolution [50]. Furthermore, ARTIQ provides a driver to manage non-proprietary hardware as an NDSP[1] that enable simple and flexible extensions to control laboratory experiments. The entire control system is then managed by a GUI with customisable applets, which can all be edited to refine workflows as it is written in PyQt .

Duke-ARTIQ-Extensions (DAX)[60] is an open-source add-on to standalone ARTIQ, which provides enhancements to the control software. One of the key advantages of the DAX upgrade is the ease to simplify experimental scripts by modularising standard experiment sequences. For example, once the state detection protocol is programmed, it can be imported and called as a function and becomes interchangeable between experiment scripts. This reconstructs the thousands of line-length scripts into neat, legible sequences. For the details of the ARTIQ layout and modules, see the QCL GitHub folder.

DAX scripts can also be calibrated automatically, with the package dax-scheduler [61]. The calibration flow is represented on a directed acyclic graph (DAG) and after successful calibration (dependent on error bars and fit) the graph moves forward.

[1] Network Device Support Package

A final upgrade implemented in the lab is that version control was implemented for the experiment. ARTIQ-DAX code is stored on Github and the repository is shared between all users on different computers. As the ARTIQ hardware can only be controlled by one user to debug timing issues, having the repository available means that all users can draft experimental scripts and edit simultaneously. In addition to this, the ARTIQ simulator[60] was installed on non-lab computers to verify code errors and test the script's functionality. Each experiment has a unique identifier and the results are condensed into a h5 file [62]. These are then uploaded to GitHub and can be decoded for further analysis.

4.1.2 Doppler Cooling and State Detection setup

Doppler cooling is an essential initial step in the experimental sequence, for cooling the ion chain to the Doppler limit and serving as an indicator of the presence of ions in the trap. Experimental calibration of both power and frequency becomes necessary, especially after trapping or unlocking of the 369nm laser lock, as the cooling efficiency may be impaired. The quantifiable ion fluorescence is measured using an Avalanche Photodiode (APD), which provides a number of photon counts displayed on the ARTIQ dashboard applet.

Optimisation of the 369 nm DC beam is performed by adjusting the power and frequency. To begin, the 369nm fluorescence is maximised by adjusting the DC laser beam frequency until the highest photon count rate per second is reached. Subsequently, the laser's power is increased until a saturation point is reached, where additional power no longer increases the ion count rate. As the laser is now tuned to the resonance, the cooling performance can be optimised by setting the detuning to $-\Lambda/2$ (with Λ representing the linewidth). To do so, the power is reduced (by reducing MOGLabs QuadRF AOM driver power) so that the count rate is halved and then the frequency (by changing cavity length) is red-detuned until the count rate is halved again. This gives the required detuning as for a low saturation parameter, halving the fluorescence by changing the frequency returns approximately $-\Lambda/2$ detuning.

Thereafter, the state detection power and frequency (QuadRF driving the AOM in SD path) are optimised by tuning the AOM frequency so that it is on resonance and the amplitude so that the SD power is at the saturation power. Once both of these intensities and frequencies are optimised, the DC and SD beams are prepared and can be used in the experimental sequences.

4.1.3 Cooling sequence

The reduction of the temperature of the ions' motional states to the Doppler limit is achieved with the 369 nm beam. The Doppler temperature is given by Equation 2.23 and for Doppler Cooling on the $^{171}Yb^{+}$369 nm transition so that $T_D \approx 470\mu$K. This can be related to the mean phonon occupancy $\bar{n}$ with $\bar{n} = k_B T_D/\hbar\omega_i$, giving $\bar{n} \approx 7$ on the radial X and Y modes and $\bar{n} \approx 20$ on the axial mode.

However, further cooling to bring the motional states close to their ground state energy is performed on the ion. MS gates do not explicitly require ground state cooling, as the protocol does not rely on the ground state blockage like the Cirac-Zoller gate [22]. Nevertheless, simulations and experimental results of MS gates note that preparation into the ground state improves gate fidelity [38]. Ground state cooling is commonly achieved by resolved sideband cooling [63, 64]. To accomplish this, the Raman beams are detuned to the red sideband, facilitating coherent population transfer from $|0\rangle_e \otimes |n\rangle_m$ to $|1\rangle \otimes |n-1\rangle$. Thereafter, optical pumping is performed to prepare the qubit back into the ground electronic state, giving $|0\rangle \otimes |n-1\rangle$. Due to the optical pumping beam being an incoherent process and reutrning the qubit in the $|0\rangle$ state, this can be performed in cycles. This process is repeated and application of this method 30-40 times reduces the motional state to $\bar{n} = 0.06$ and can be seen in Figure 4.1.

When multiple motional modes are present, it becomes necessary to cool each sideband individually. This cooling process needs to be repeated at each red-sideband mode frequency. The cooling scripts within the module are designed to scale, automatically making adjustments to the cooling protocol to account for the presence of more ions in the trap. However, it's important to note that the scaling of this method becomes increasingly time-consuming as the number of ions in the trap grows. To address this issue, alternative cooling methods are employed for longer ion chains. Electromagnetic Induced Transparency (EIT) [65, 66] cooling was implemented in the Yb trap. However, it was not included in the experimental sequence for this thesis and its discussion is omitted. For further information, see [67]. Implementation of this EIT cooling protocol enables the cooling of longer chains at a faster rate than resolved sideband cooling.

Following the cooling process, measurements of the phonon occupations of each motional mode and heating rate measurements are conducted to characterise the cooling efficiency. Temperature measurements are obtained by performing frequency scans of the blue- and red-sideband transitions after cooling, and fitting is applied using the SciPy package [68]. The average phonon number ($\bar{n}$) is computed by considering the ratio R of amplitudes, and

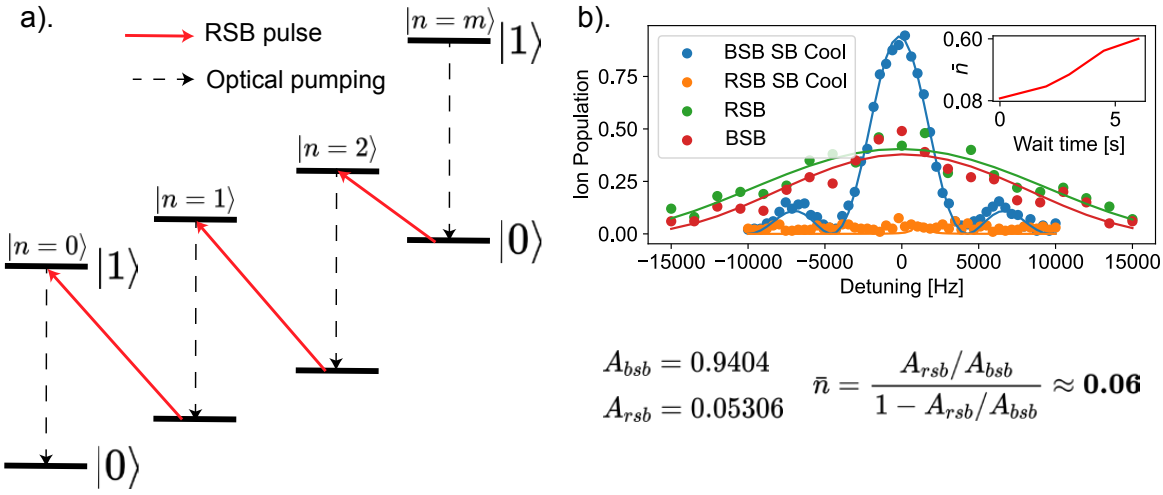

FIGURE 4.1. **a).** Sideband cooling protocol, where optical pumping and red-sideband pulses are interleaved to cool the motional state. The motional quanta are displayed above the levels and are reduced by one with each cycle. This is performed on each mode to cool the ion to the 2D ground state. **b).** Temperature measurements of the cooled motional state, with an $\bar{n} = 0.06$.

the results can be seen in Figure 4.1.

$$\bar{n} = \frac{R}{1-R}, R = \frac{A_{RSB}}{A_{BSB}}, \tag{4.1}$$

where $A_{BSB/RSB}$ is each amplitude maximum after performing a frequency scan. For lower $\bar{n}$, the amplitude of the red-sideband frequency scan diminishes. This occurs because the red-sideband transition becomes increasingly ground state blocked when $\bar{n} \to 0$. To measure the heating rate, a wait time $t \in [0, 5\text{s}]$ is introduced before the red-sideband frequency pulse, leading to an increase in the number of motional quanta. The obtained data reveals that the temperature of the COM radial X mode is approximately $\bar{n} \approx 0.06$, with a heating rate of $\dot{\bar{n}} = 0.2$ quanta s^{-1}.

4.1.4 EMCCD detection integration

Ion detection presents challenges when it comes to scalability, especially while maintaining high fidelity and achieving fast readout. Typically, Avalanche Photon Detectors (APDs) are employed for the detection of single ions, distinguishing them as either dark or bright. However, when there are multiple ions in the trap, only the total number of photons collected can be identified, without providing any spatial information as to their origin. To introduce an additional dimension of information, Multi-channel Photo Multiplier Tubes (PMTs) can be utilised. Each PMT in a one-dimensional array functions like an APD. Alternatively,

Electron-multiplying Charge-Coupled Devices (EMCCDs) offer two-dimensional spatial information, where each pixel provides a count rate. This enables the generation of images, as depicted in Figure 3.18, allowing for the visual resolution of ions.

In the Paul trap lab, an Andor iXon Ultra 897 EMCCD is used to detect the ions in two-dimensional space. This camera is operated by initiating Remote Procedure Calls (RPCs) through the ARTIQ NDSP on a Secondary Windows Computer (SWC), using the Andor Software Development Kit with an open-source wrapper [69]. The camera collects light to capture images of the Yb trap in a setup similar to the one employed for the Yb-Lu trap as shown in Figure 3.13. The comprehensive layout is detailed in [32]. Following image capture, data transfer occurs either through a USB connection to the SWC or via the ARTIQ core using a frame grabber with a Camera Link™connection[2]. When transferring full camera images, the data is sent through USB to the SWC. However, this method incurs a latency on the order of tens to hundreds of milliseconds when transmitting to the experimental Linux control computer. Alternatively, the use of a frame grabber enables high-speed data transfer but is limited to information from a 16-pixel area. Consequently, it is not possible to transfer entire camera images using this approach. To swiftly transmit images of the ions, specific regions known as Regions of Interest (ROI) are identified to encompass the ions.

Due to the precise temperature control within the lab and minimal fluctuations in the beam path, the Regions of Interest (ROIs) remain stable in terms of pixel locations for ions with the same trap parameters. However, during the calibration of the MS gate, adjustments are made to the DC potential to equalise the beam intensity. As a result, the ROIs need to be updated with each measurement of the ion Rabi rate. To streamline this process, an automatic ROI detection script was developed. Within this script, a complete image of the ion is captured, and an algorithm is employed to determine and update the location of the ROIs. This updated information is then incorporated into the ARTIQ datasets, enabling their use in further camera experiments.

The algorithm employed for ion detection is the Blob detection algorithm from [70], which relies on the Laplacian of the Gaussian method. To prepare the camera image for this algorithm, the data is first normalised and the array is then converted into Boolean values if the value exceeds a specified threshold. Subsequently, areas with fewer than two nearest neighbors are eliminated and the Blob detection algorithm is executed. The algorithm outputs the precise ion locations, which are subsequently organized into distinct regions of interest, each corresponding to an individual ion. In addition to this, a crop region is defined,

[2] https://github.com/sinara-hw/Grabber/wiki#grabber

encapsulating the entire ion area. This crop region is subsequently passed to the camera to parametrise the fast-cropped image readout.

Following the calibration of the camera with ROI detection, we can assess the state preparation and measurement fidelities through camera detection using a thresholding. In this detection method, ions are designated as "bright" if the value of the sum of the ROI pixels exceeds an optimised threshold. This threshold must first be calculated using high-fidelity operations on the ions themselves. Microwave pulses enable global operations on the trapped ions, achieving a SPAM error of 1.20(6)% as demonstrated in [71] and calibrated with the APD. Microwave operations allow for selective ion preparation in either $(|0\rangle)^{\otimes n}$ or $(|1\rangle)^{\otimes n}$. The SPAM fidelity of the entire camera operations can then be inferred, by preparing the ions and then performing detection on each of the ROIs. The counts are then plotted into two overlayed histograms, separated into those prepared into the $(|0\rangle)^{\otimes n}$ and the counts from the $(|1\rangle)^{\otimes n}$ state. Threshold values are then input with this data to compute the SPAM fidelity and the value maximising fidelity is chosen. Once calibrated, SPAM fidelities for an ion in an ROI were calculated at $96.2 \pm 0.4\%$.

4.1.5 APD thresholding

In most single ion experiments in the Yb trap, the APD is used to determine the probabilities $P_{|0\rangle}, P_{|1\rangle}$ of the ion being in the $|0\rangle$ or $|1\rangle$ states. Measurement with the APD collects the incident photons and produces a count c, representing the number of photons detected. Each data point in the experiment is repeated N_{rep} times, where the count of photons c is collected for each repetition. This number is sent to the ARTIQ control computer via an input TTL and is used to determine if the ion was measured as bright or dark.

On the experimental control computer, the extraction of a state probability is performed by using a context manager in ARTIQ. Upon opening the context manager, a new buffer to store the data is created. The input TTL channels in the ARTIQ control system detect an APD event, give it a timestamp and place it in the buffer. The buffer is read out and the data is added to a histogram as seen in Figure 4.2a. After the repetitions of the experiment are completed, the context manager exits and the probability of the ion is calculated given the APD count histogram obtained during the repetitions.

The method of thresholding is used to determine the ion state probability. A single ion will be considered bright if its photon count c within a detection period is above a threshold value t. The threshold has to be calibrated to ensure the error in assigning the ion as bright or dark

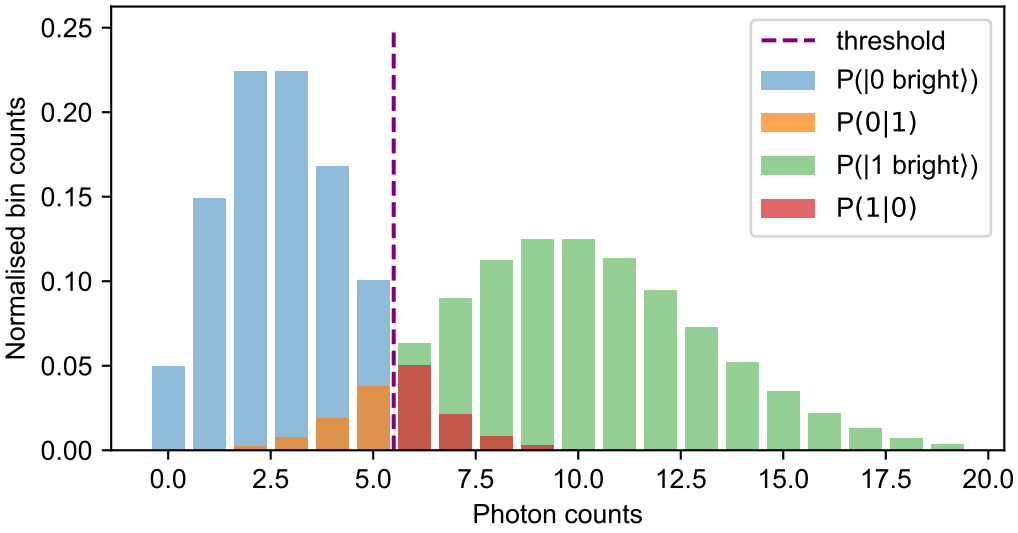

(A) Histogram for one ion thresholding, where the error matrix values are described.

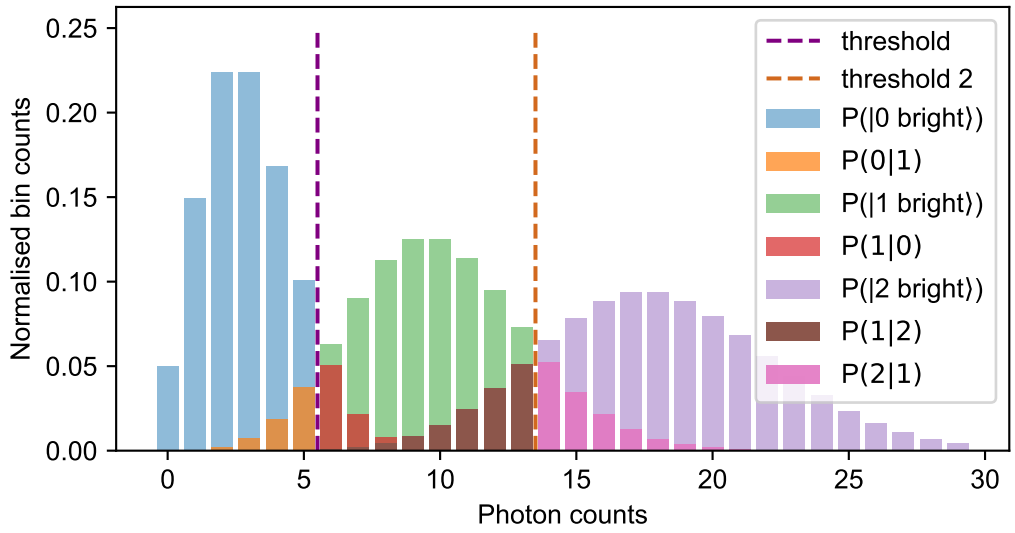

(B) Two ion thresholding

FIGURE 4.2. In 4.2a, the APD count histogram for a single ion is displayed, along with the threshold that has been calibrated. The APD histogram count is modelled as a Poisson distribution. A threshold of 6 is set here, classifying counts below this value as non-bright and those above it as bright. Moving to 4.2b, the histogram for two ions is showcased. In this case, three distributions are overlaid, representing the Poisson distributions for P(0 bright), P(1 bright), and P(2 bright). With two ions, two separate thresholds are employed, and the errors associated with incorrect measurements can be observed. The values presented are simulated but serve to illustrate the thresholding technique.

erroneously is minimised. The ion is selectively prepared into the dark or bright state to calibrate this threshold, so microwave pulses either prepare the single ion to be in $|0\rangle$ or $|1\rangle$.

The dark and bright histograms are then overlayed and the threshold is chosen which minimises the error of mislabelling dark or bright ion. A 2×2 error matrix $\hat{\mathbf{P}}$ contains the probabilities of labelling an ion with state i given a prepared state j, where,

$$\hat{\mathbf{P}} = \begin{pmatrix} P(0|0) & P(0|1) \\ P(1|0) & P(1|1) \end{pmatrix}, \tag{4.2}$$

with P($i|j$) being the probability of classifying i, given the state j was prepared. The diagonal of the matrix should be maximised by thresholding to give the optimal detection fidelity, as the fidelity is calculated as the average of the diagonal elements. For a single ion, the fidelities are calculated with list comprehension and a threshold is chosen which maximises the detection fidelity, typically the experimental value is $t = 4$.

The ARTIQ detection module contains the parameters for the APD and the default detection period is 250 μs and divided into five bins. The data stored in the buffer contains the counts alongside the timestamps of the events. Using this time-resolved data, analysis can be performed for the counts over the detection period to offset error from leakage from the $|1\rangle$ to $|0\rangle$ state via off-resonant scattering.

As mentioned before, an alternative detection method for two ions can be performed using the APD. The APD offers high fidelity for single ions, however, for multiple ions does not provide spatial resolution. Nevertheless, the number of ions that are measured as bright can be interpreted by the count rate on the APD. If one ion produces a count rate of $\dot{n}$, then m ions should be approximately $m\dot{n}$. Like a single ion, thresholds t_1, t_2 can be set to minimise the error in state detection and aim to separate the states into $P(|00\rangle)$, $P(|01\rangle) + P(|10\rangle)$ and $P(|11\rangle)$. Previous methods in the QCL used the histogram of one ion in the trap to characterise the threshold value t_2 for $P(|01\rangle) + P(|10\rangle)$. The methods developed in this thesis always use two ions in the trap and do not require the extra time-consuming step of adding an ion.

There are two ways of calibrating the thresholds for two ions when there are two ions in the trap. The first method involves preparing three histograms and subtracting them to derive the dark, one bright and two bright histograms. The other method involves just preparing the ions in a superposition state using a previously calibrated $\pi/2$ microwave pulse. Both of these methods rely on the fact that the histograms for the superposition state are a combination of the distributions for dark, one and two bright.

The prepared state from a global $\pi/2$ pulse can be written as $1/\sqrt{2}(|0\rangle + |1\rangle) \otimes 1/\sqrt{2}(|0\rangle + |1\rangle) = \frac{1}{2}|0 \text{ bright}\rangle + |1 \text{ bright}\rangle + \frac{1}{2}|2 \text{ bright}\rangle$. Hence the distribution on the APD for the $\pi/2$ experiment will be a summation of each distribution $P(|00\rangle)$, $P(|01\rangle) + P(|10\rangle)$ and $P(|11\rangle)$ with a percentage contribution of 25%, 50% and 25% respectively. For the first method to extract the distribution of $P(|01\rangle) + P(|10\rangle)$ from the $\pi/2$ pulsed state, the histograms of the zero- and π-pulse experiments are multiplied by a factor of 1/4 and subtracted.

For the second method used in this thesis, a script is set up to run two experiments each with 5,000 repetitions. The first collects APD data from a zero-pulse (delay time of $\pi/2$) and the second collects from after a microwave $\pi/2$ pulse. The first histogram is then fit to a Poissonian distribution and the second distribution is fit using curve_fit to a function with a summation of three Poissonian distributions, representing the three states. Then the fidelity is estimated using the overlap of the Poissonian functions and the threshold which optimises the fidelity is then found. The error matrix is then calculated and is shown in Equation 4.3, with the fidelity calculated by averaging the diagonal giving 0.901.

$$\hat{\mathbf{P}} = \begin{pmatrix} P(0|0) & P(0|1) & P(0|2) \\ P(1|0) & P(1|1) & P(1|2) \\ P(2|0) & P(2|1) & P(2|2) \end{pmatrix} = \begin{pmatrix} 0.9868 & 0.0544 & 0.0004 \\ 0.0128 & 0.8810 & 0.1644 \\ 0.0004 & 0.0646 & 0.8352 \end{pmatrix}. \tag{4.3}$$

4.1.6 Maximum likelihood

Despite thresholding being effective for single-ion states, the detection of two-ion states measured with the APD does not achieve a similar level of SPAM fidelity, as evident in the non-optimal fidelities in the diagonal of Equation 4.3. To enhance this fidelity, the method of maximum likelihood was integrated into the ARTIQ system, modifying the classified state values based on the estimated error matrix [72, 73, 32]. The error matrix is stored as an ARTIQ dataset from the thresholding experiment and is used after each two-ion experiment to adjust the probability values.

The method is determined using the map between measured probabilities P^* and the true probabilities P. The map between the measured and true is the matrix described by $\hat{\mathbf{P}}$ in Equation 4.3 giving $P_i^* = \sum_j \hat{\mathbf{P}}_\mathbf{ij} P_j$. To find the true values, the log-likelihood function $f(P_1, P_2, N_{rep}, \hat{\mathbf{P}})$ is probed with different P values. P_1 and P_2 are the true probabilities of measuring one bright and two bright. Note that P_0 is omitted from the function, due to the normalisation rules $P_0 = 1 - P_1 - P_2$. The function is defined as

$$
\begin{aligned}
f(P_1, P_2, N_{rep}, \hat{\mathbf{P}}) &= \log\left(\frac{(N+1)(N+2)N!(P_1^*)^{x_1}(P_2^*)^{x_2}(1-P_1^*-P_2^*)^{N-x_1-x_2}}{x_1!x_2!(N-x_1-x_2)!}\right) \\
&= \log(N) - N + \log((N+1)(N+2)) + x_1\log(P_1^*) + x_2\log(P_2^*) \\
&\quad + (N-x_1-x_2)\log(1-P_1^*-P_2^*) \\
&\quad - \log(x_1!) - \log(x_2!) - \log((N-x_1-x_2)!)
\end{aligned} \tag{4.4}
$$

and N_{rep} represents the number of repetitions. The P values that maximise the function are the closest to the true values. To evaluate this function efficiently, Stirling's approximation, $\log(x!) \approx x\log(x) - x$, is employed to compute large terms for any x of the form $\log(x!)$, as these can be computationally expensive functions. This approximation is explicitly incorporated into the maximum likelihood function when dealing with factorial values where $x > 150$.

Upon the completion of the experiment, the measured state probabilities P^*, along with the number of repetitions N and the SPAM error matrix $\hat{\mathbf{P}}$, are provided as input to the maximum likelihood map function. By iterating through each scan point, the maximum likelihood P values are determined. These values are found by cycling through different P values (range search) to apply the mapping and calculate the log-likelihood. The values that maximise the function are then identified, typically requiring only a few seconds to complete. The improvement in data is seen in Figure 4.3, where microwave Rabi flops for two ions using the APD are shown.

4.1.7 Raman calibration

In the Yb trap, a two-photon stimulated Raman process is driven with a 355 nm laser, as described in subsection 2.4.1. The two beams are non-co-propagating and are generated from the same pulsed laser. The laser head is a Spectra-Physics Vanguard with an average power of 2.5W and a repetition rate of 80MHz. The beam path and breadboard diagrams of the 355 nm laser can be found in [32, 74].

To achieve the frequency splitting between the two $^2S_{1/2}$ hyperfine levels $|0\rangle$ and $|1\rangle$, two beam paths are generated with a PBS and arrive at the ion orthogonally. In the first beam path (referred to as 70 arm), a 70 MHZ AOM is placed in, from which the first-order is picked-off with a negative frequency shift. This beam is then fibre-coupled and delivered to the trap breadboard. In the other (referred to as the 200 arm), a double pass 200 MHz AOM and a beatnote 200 MHz AOM are used, both shifting negatively with the first order. At the ion,

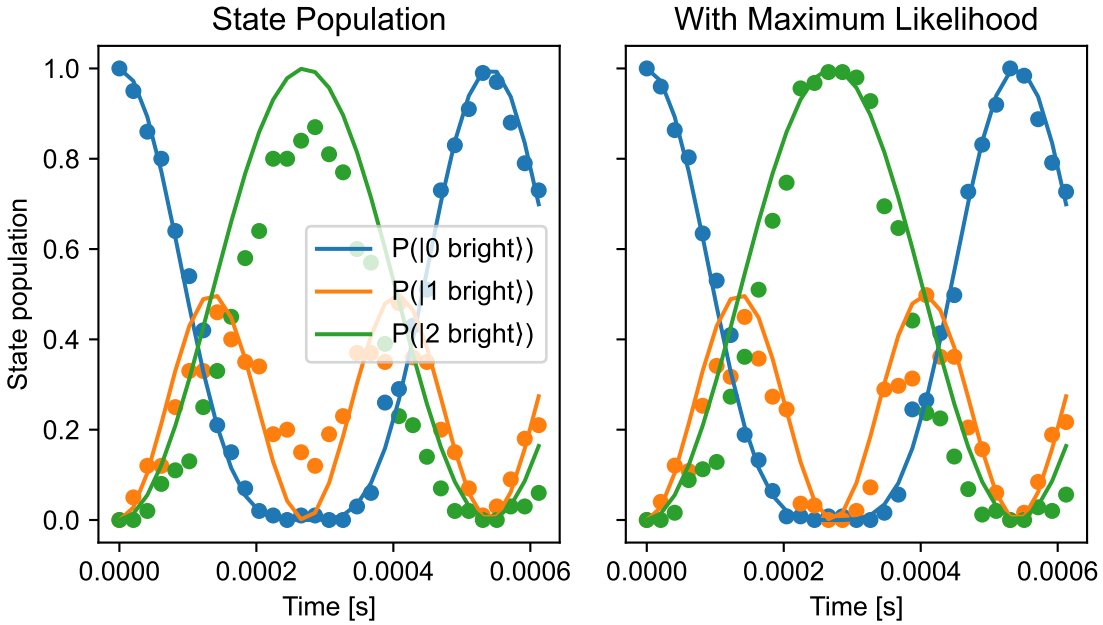

FIGURE 4.3. Maximum likelihood correction to state probabilities demonstrated on microwave Rabi flops. The panel on the left shows the state probabilities for the APD without the maximum likelihood method applied. The right-hand panel shows the state probabilities after the collection of true probabilities, closer matching the predicted rabi flops. In the plots, it is evident that the P(|1 bright⟩) and P(|2 bright⟩) have the largest improvement, with their flops reaching 0.5 and 1 respectively.

the difference wavevector becomes $\Delta\vec{k} = \vec{k}_{200} - \vec{k}_{70}$, where $\Delta\vec{k}$ is perpendicular to the trap axis and it couples to the radial modes. Therefore, the shift Δ_{AOM} of the AOMs taking into account the beam orientation is as follows

$$\Delta_{AOM} = \Delta_{200} - \Delta_{70} \tag{4.5}$$

$$= (-2 \times 200 - 200) - (-70) \tag{4.6}$$

$$= -530\text{MHz} \tag{4.7}$$

As the laser is pulsed, each beam is considered to be an optical pulse train. In the frequency domain, each beam is represented as a set of comb teeth with a spacing of 80 MHz. Pairs of teeth within the frequency comb give stimulated absorption from the $(m+n)$th comb tooth and stimulated emission from the mth tooth. The 355 nm laser achieves the qubit splitting with the mth and m+165th comb teeth, giving the frequency shift due to the repetition rate as $165 \times \omega_{rep} = 13200$ MHz. The final interaction frequency is then determined by the

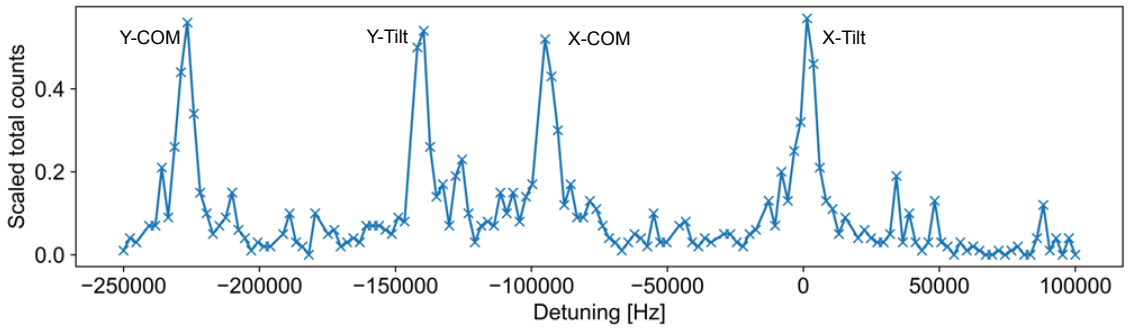

FIGURE 4.4. Raman spectroscopy on the Red sidebands with the centre point of the detuning set at 69.65MHz. The sidebands can drift (see later section) and the frequencies must be recalibrated to maintain the same level of precision for sideband cooling or entangling gates.

summation of the AOM and repetition shifts, giving the hyperfine splitting.

$$\omega_0 = n\omega_{rep} + \Delta_{AOM} = 12.6\text{GHz}, \tag{4.8}$$

where ω_0 is the qubit frequency, with finer tuning available by changing the frequency of the 70 MHz AOM.

Finding the transition frequencies of the ion can then be performed, using Raman spectroscopy. This is performed and scanned in ARTIQ by altering the frequency on the 70MHz AOM and driving the ions with a fixed duration. When a transition is driven, coherent population transfer occurs between the states[3]. Individual peaks are seen for each transmission, lines are seen for the carrier, and red and blue sidebands with $\pm\omega_{x,y}$ detuning. In Figure 4.4, the spectrum for two ions' red sidebands can be seen by performing Raman spectroscopy. This process is used to calibrate the sideband cooling frequencies and then Rabi flopping is performed on each mode to calibrate the pi times used in the cooling.

Optimising the Rabi rate of the Raman laser is also critical to enact fast gates. To increase the incident laser power on the ion, a set of lenses are held in high precision zoom mountings in X-Y translation stages just before the trap viewport. These can be adjusted along with optimising fibre coupling.

Afterwards, Ramsey wait time measurements using microwaves as in Figure 4.5 can be used to indicate the intensity of each 355 nm beam one by one on the ion. To maximise the intensity, the Stark shift [45, 46] on the ion is maximised. This is done by coupling 369 nm light into the 355 nm fibre, which then is shone through the trap using the 355 nm pre-trap optics. This Stark

[3] e.g. $|0, n\rangle \rightarrow |1, n+1\rangle$ for the blue sideband

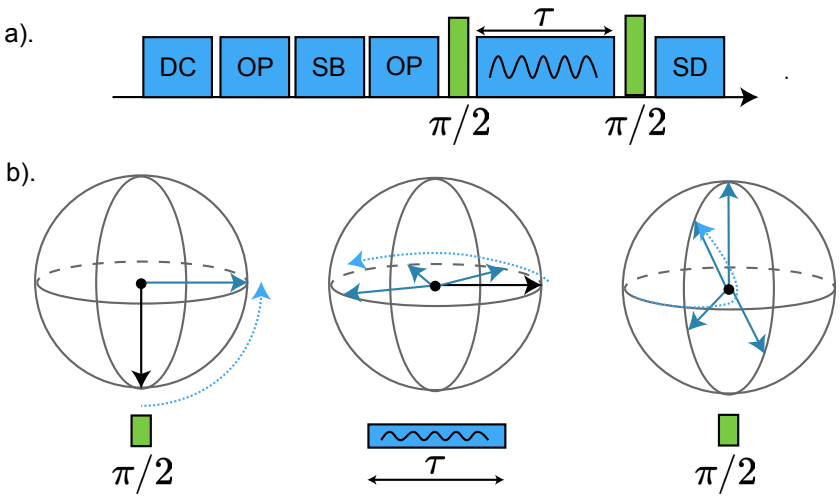

FIGURE 4.5. a). Ramsey experiment microwave wait time experiment pulse sequence, to calibrate individual Raman beam intensities and other experiments such as coherence time measurements. Green pulse $\pi/2$ is enacted by driving the hyperfine qubit at 12.6 GHz and the wait time τ is varied. During the wait time, the 355nm laser beams are individually activated and thereafter another $\pi/2$ pulse. b). Bloch sphere representation of the Ramsey wait time experiment to induce procession around the equator of the Bloch sphere. The $\pi/2$ pulse moves the state to the equator creating an equal superposition. Activating either the 70 or 200 arm of the Raman laser then processes the qubit around the equator, inducing a σ_z interaction due to the Stark shift. Finally, another $\pi/2$ pulse is completed and a projective measurement is taken.

shift is seen as the frequency of precession around the Bloch sphere in a Ramsey wait time or phase experiment. Scanning one of the Raman beams and performing the measurement allows each beam's interaction to be individually optimised. Further optimisation is then performed by driving carrier operations on the ion and maximising the Rabi frequency.

4.1.8 Gate tune up

For the gate calibration, mode frequency datasets from Raman spectroscopy for sideband cooling optimisations are imported into the MS calibration. These are updated with more precise scans, to calibrate the MS interaction and improve the gate fidelity.

Rabi rate equalisation When performing the MS gate, both ions require equal Rabi frequencies from the Raman laser beams to maximise fidelity. This process requires two steps, firstly measuring the inequality between the two ion rates and secondly altering the ion or beam position to change the intensities. Either the APD or the EMCCD can be used to measure

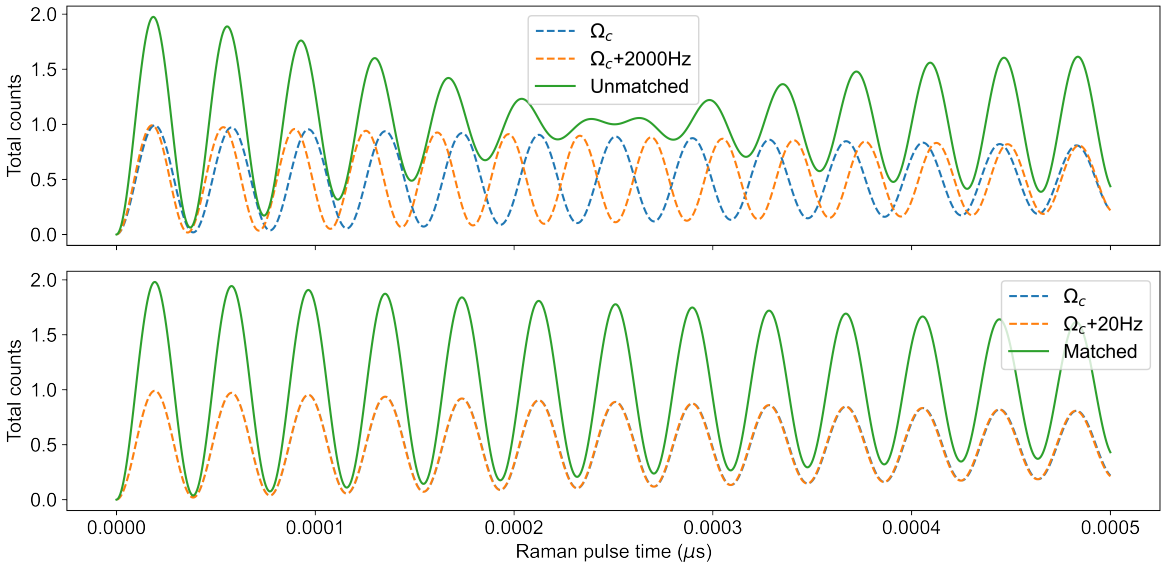

FIGURE 4.6. The APD measurement from two ions with unmatched Rabi frequencies differing by 2 kHz and matched Rabi frequencies Ω_c. The y-axis is the total counts observed on the APD. In the top plot, there is a point where destructive interference between the frequency unmatched Rabi flop signal of the two ions. This is resolved by balancing the beam intensity, leading to the lower plot where both ions have equal Rabi frequencies.

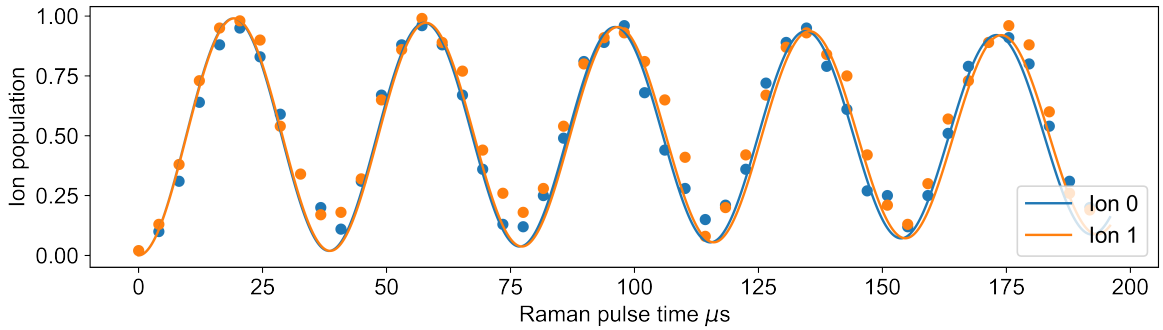

FIGURE 4.7. Balanced Rabi rates for both of the ions on the EMCCD. Each ion is individually resolved by the camera and the data is streamed into ARTIQ for plotting. The standard deviation is calculated between the two ions and minimised by offsetting the DC voltage control.

the intensity homogeneity between the ions. The difference in the measurement process lies in the EMCCD's ability for individual ion resolution. For the APD, when driving carrier transitions with the Raman beams, the difference between beam intensity can be seen as each ion will independently flop at different frequencies and an interference pattern between both appears on the APD as seen in Figure 4.6. The difference beatnote frequency $\Delta\Omega = \Omega_1 - \Omega_2$

is minimised to improve the equality of the laser intensity. For the camera, as each ion is individually resolved, the Rabi rates are fitted and extracted. The standard deviation between the two Rabi rates is calculated, serving as a quantifiable metric to minimise. The beam intensity is altered by moving the position of the foci of the Raman laser beams. However, if the Raman beams are already optimised for intensity then it can prove problematic to adjust these finely. Instead, the DC voltage control can be finely offset, displacing the ions around in the trap. The process for minimising the amplitude inhomogeneity is then done in a stepwise fashion. The ions are moved, the carrier time scan is completed and the gradient of inhomogeneity is found.

Fine spin-motion interaction frequency calibrations For the calibration of the motional frequencies, two distinct methods are employed. Initially, Raman spectroscopy of the sidebands is conducted to obtain an estimate of the motional frequencies. This process is essential for sideband cooling. However, for achieving higher-fidelity entangling gates, more precise mode frequency calibration is required. This level of calibration is achieved by using the spin-motion interaction.

The calibration process begins with the ion in the ground state, cooled and prepared. A specific mode is selected, and a bichromatic signal is sent to the acousto-optic modulator (AOM), either through a direct digital synthesizer (DDS) or an arbitrary waveform generator (AWG). The two tones are set to the resonance of the red- and blue-sideband, with either a symmetric or anti-symmetric detuning as the scanning variable. This interaction initiates a spin-motion interaction between the ion and the bosonic mode, resulting in the displacement of the motional wavepacket. After preparation into the fiduciary state $|00\rangle$ [4], the wavepacket is split into two and displaced. The Unitary operator for displacement on the COM mode is described as

$$U_{out}(t) = D(\alpha(t)) \left|++\right\rangle_x \left\langle++\right|_x + D(-\alpha(t)) \left|--\right\rangle_x \left\langle--\right|_x , \tag{4.9}$$

where the phase-space trajectory after the drive time t can be simplified as

$$\alpha(t) = \eta \int_0^{\tau/2} dt' \Omega\left(t'\right) e^{-i\delta(t')t} e^{i\phi(t')} \tag{4.10}$$

$$\alpha(t) = e^{i\phi}\alpha_0(1 - e^{i\delta t}) \tag{4.11}$$

as phase, frequency and Rabi rate are constant and the global phase factor is omitted. In these equations $\alpha_0 = \eta\Omega_c/2\delta$. δ is the symmetric detuning which is scanned, Ω_c is the carrier

[4] The fiduciary state can be decomposed as $|00\rangle = \frac{1}{2}\left|++\right\rangle_x + \left|+-\right\rangle_x + \left|-+\right\rangle_x + \left|--\right\rangle_x)$, with the first and last term being affected by the COM spin-motion interaction.

Rabi frequency and η is the Lamb-Dicke parameter for the spin-motion interaction. This displacement is linear if $\delta = 0$ and curved if $\delta \neq 0$.

At a pulse time of $\tau/2$, the motional phase of the driving signal is changed by π and then driven again for another $\tau/2$. This results in the following operator

$$U_{in}(t) = \hat{D}(\alpha(t)) \left|--\right\rangle_x \left\langle--\right|_x + \hat{D}(-\alpha(t)) \left|++\right\rangle_x \left\langle++\right|_x , \tag{4.12}$$

as the π phase shift alters the displacement operator so that $\hat{D}(e^{i\phi}\alpha(t)) = \hat{D}(e^{i\pi}\alpha(t))$. Therefore, the operation of $U_{in}U_{out}$, when the detuning is zero, serves as an identity operator on the state $|00\rangle$. When the calibration frequency precisely matches the mode frequencies, the displacement occurs along straight lines in phase space, resulting in a probability of zero. The motional wavepacket returns to its origin and the spin-motion interaction becomes disentangled.

However, when the detuning is non-zero and there is an offset in the motional sidebands, changing the phase throughout the experiment invalidates the assumption made from equations 4.10 to 4.11. By splitting the integral and recalculating, a final displacement is given by

$$\alpha(\tau) = 2\alpha_0 \left(e^{i\delta\tau} - 1\right). \tag{4.13}$$

Consequently, at the gate time τ, the displacement is non-zero, and as a result, the state does not return to $|00\rangle$. Upon measurement, since the state is in a superposition between the spin and motional state, there will be a loss of purity in the projective measurement, leading to a non-zero P_2 measurement. Taking the result from before, when the frequency is on resonance, a dip will be seen in the P_2 value, indicating adequate calibration. To further increase the precision of the calibration, the total pulse time is gradually increased, narrowing the dip feature and allowing finer calibration accuracy in the range of Hz.

4.1.9 MS experimental sequence and fidelity

Following the detuning calibration, a primitive MS interaction was initiated. To perform the MS calibration, specific parameters needed to be obtained. For this purpose, an ARTIQ script was set up to calculate the MS detuning and Lamb-Dicke parameters, automatically populating datasets. This script is versatile, allowing it to be applied to different modes, and providing the flexibility to configure the number of loops for a k-loop gate. The detuning δ_{MS} is calculated as follows, with

$$\delta_{MS} = \frac{2\pi}{\tau_g} = 4\pi\Omega_{BSB/RSB}\sqrt{k} = \frac{2\pi\sqrt{k}}{\frac{t_{BSB}+t_{RSB}}{2}}. \tag{4.14}$$

Here, τ_g is the MS gate time, $\Omega_{BSB/RSB}$ is the Rabi frequency of the BSB or RSB interaction, and $t_{BSB/RSB}$ is the pi time for the BSB or RSB interaction.

An MS time scan was conducted to confirm whether the state population evolution aligned with the expected population trajectory. The MS time scan involves a symmetrical detuning from the sidebands using the calculated δ_{MS} and scanning the interaction time. The resulting scan is shown in the top panel in Figure 4.8. After verifying that the gate time matches predictions, an additional MS detuning scan was performed. If the gate is pulsed at τ_g with the symmetric detuning scanned, the result should equate to the bottom panel in Figure 4.8. The point in the detuning and time scan, which equates to the generation of a maximally entangled Bell state, is where populations P_0 and P_2 are equal to 0.5, and the population P_1 is minimised. Nevertheless, this information is not sufficient to determine if the maximally entangled Bell state has been generated. To do so, a more comprehensive test of the state is required by investigating fidelity via parity measurements.

The fidelity of achieving a target Bell state $|\Phi\rangle = 1/\sqrt{2}(|00\rangle + |11\rangle)$ can be measured with the density matrix of the measured state $\hat{\rho}$ in the following formula

$$\mathcal{F} = \langle\Phi|\hat{\rho}|\Phi\rangle\,, \tag{4.15}$$

where $\mathcal{F}$ is the measured fidelity.

In practice, the fidelity can be characterised by performing a parity measurement on the state after the MS gate is completed. Parity measurement involves rotating the final maximally entangled state using a $\pi/2$ carrier pulse (Figure 4.9). This carrier pulse is then repeated with different phases scanning over the range $[0, \pi]$ to characterise the state in each basis. For APD detection without spatial information of the ions, the parity contrast is obtained by computing the function $P_{parity} = P(|0 \text{ bright}\rangle) + P(|2 \text{ bright}\rangle) - P(|1 \text{ bright}\rangle)$ for each scanned phase point. The oscillation amplitude of this function is equal to contrast π_{parity}. Hence, the fidelity is obtained as,

$$\mathcal{F} = \frac{P_0 + P_2}{2} + \frac{\pi_{parity}}{2}, \tag{4.16}$$

4.1.10 Drift of motional mode frequencies

A significant source of error in trapped ion entangling operations is the fluctuations in the secular frequencies. For example, suppose these frequencies are miscalibrated and an MS interaction is intended. In that case, the desired MS Hamiltonian will not be induced onto

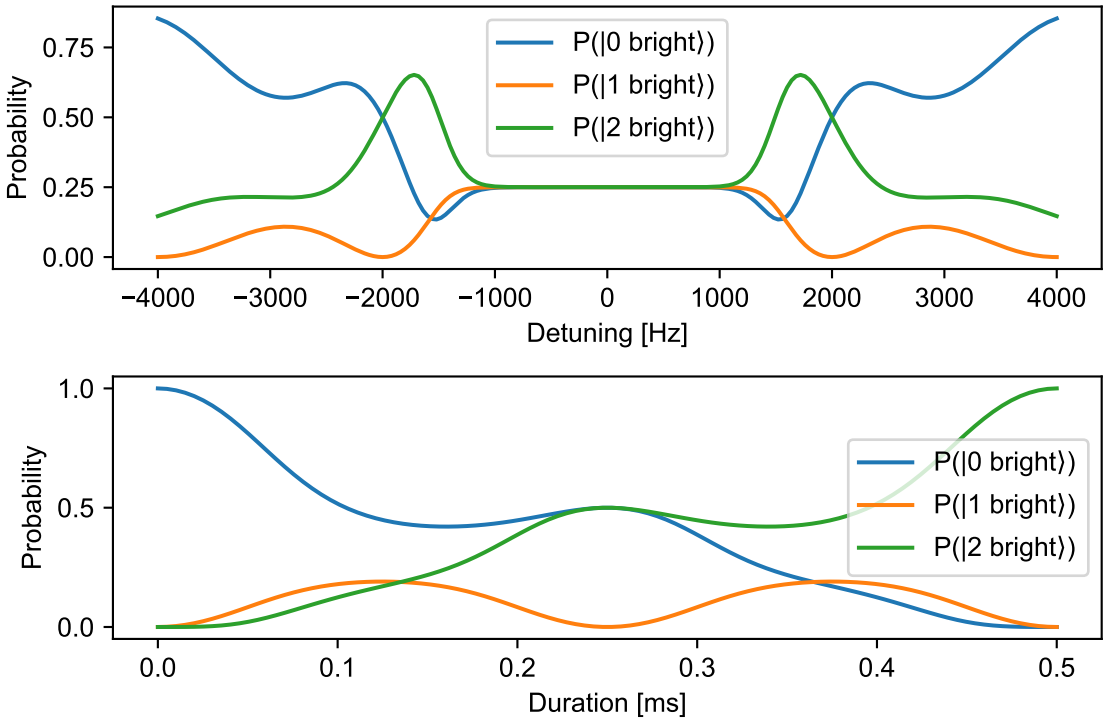

FIGURE 4.8. Top panel shows the theoretical MS detuning scan in the absence of noise. The x-axis is the scan variable of the symmetric detuning of the bichromatic Raman beams. The points corresponding to ± 2 kHz are points where the gate is maximally entangled at the gate time and indicates the correct MS detuning for a given gate time. The bottom panel shows the MS evolution for a primitive MS gate, with a bichromatic drive detuned away from the red- and blue-sidebands. The x-axis shows the evolution in time and at 0.25ms the maximally entangled Bell state $|\Phi\rangle$ is reached.

the ion and the target state will not be achieved. A critical focus in developing trapped ion architectures is thus the production of stable secular frequencies and this can be achieved by improving hardware.

Hardware errors tend to propagate and typically by improving hardware sources the signal can be improved. The secular mode frequencies are directly proportional to the radial oscillating voltage on the electrodes and noise originating from this voltage source can incur fluctuations in the motional mode frequencies. Additionally, if the resonator, wiring or blades cause additional noise, then this will transform into noise on the motional frequencies. As the Mølmer-Sørensen gate uses the motional modes as an information bus, motional decoherence will impact the fidelity of the gates. There are different forms of motional decoherence which can impact the gate fidelity, such as thermal noise, heating/cooling of the ion chain and

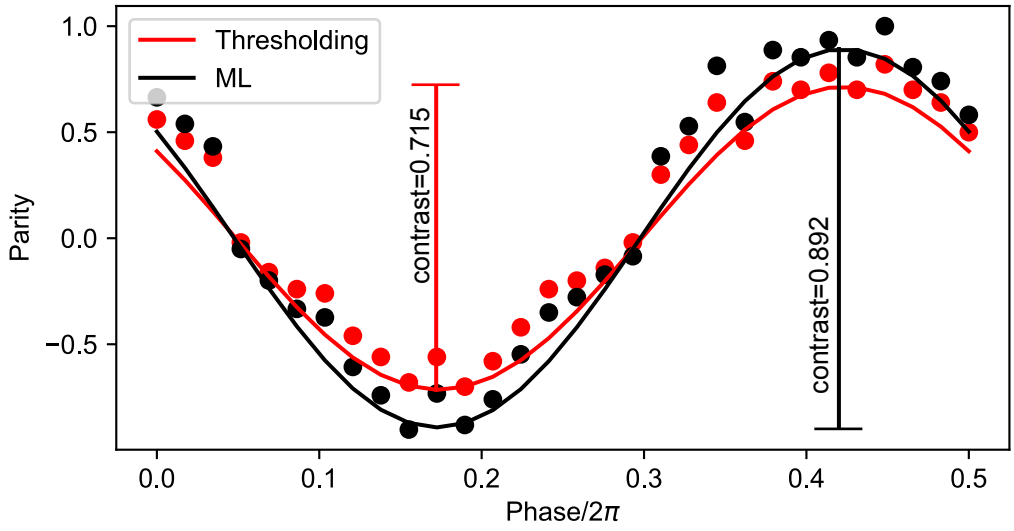

FIGURE 4.9. Parity scan for a two ion entangling gate, measured using the APD. The red analysis is done with state probabilities derived from thresholding and the black line is when the state probabilities are computed using the maximum likelihood analysis developed in this thesis. It shows a 24.8% increase in contrast.

dephasing. Motional dephasing is produced when there are detuning offsets in the gate and by improving the quality of the RF drive, the gate can be improved.

Motional mode dephasing can be measured by calculating the BSB Ramsey coherence time for a given radial mode. A Ramsey-type experiment, similar to Figure 4.5, performs this. To measure coherence times T2, Ramsey contrasts are measured for varying durations. Performing this, the qubit is prepared in a superposition state with a $\pi/2$ carrier pulse $1/\sqrt{2}(|0\rangle + |1\rangle) \otimes |n = 0\rangle$ and then a delay for a scanned Ramsey wait time is introduced to allow the qubit to be perturbed by the environment. The superposition action is undone by enacting a pulse with a phase varied in the range $\phi \in [0, 2\pi]$.

The experiment to measure the motional coherence time differs. First, it leverages the ARTIQ-DAX capability to initiate a 2D scan, with the independent variables being the phase of the final $\pi/2$ pulse along with the Ramsey wait time. Second, the pulse sequence differs as a set of two BSB π pulses intercede the carrier pulses. The full pulse sequence is as follows : the $\pi/2$ carrier pulse initiates the electronic state into a superposition and then to prepare the qubit state in a superposition between the bosonic modes, a BSB π pulse takes the state to $\psi = 1/\sqrt{2}(|0\rangle \otimes |n = 0\rangle + |1\rangle \otimes |n = 1\rangle)$. As there is a superposition now prepared in the motional states different by Fock basis of one, this can probe the stability of the bosonic state as electric field noise or other noise processes will decohere it [75]. Then, another BSB

π pulse is performed along with the scanned phase carrier $\pi/2$ pulse to map the Fock state superposition onto the qubit for readout. Like the spin T2 experiment, for a given wait time, the experiment will undergo oscillations. As the state becomes increasingly decohered, the contrast of the oscillations will decrease. The contrast of the oscillations is extracted for each scanned wait time and the decay function is fit to a decaying exponential function to extract the T2 time. This decoherence time is defined as a measure of motional coherence for a given experimental setup and can be used to quantify the motional noise.

Experimental efforts in the Yb trap, worked to improve the motional coherence time by reducing the amplitude noise from the RF drive [74]. First, RF drive sources were investigated and an increase in motional coherence time of $2\times$ was achieved by integrating a Rohde & Schwarz SMB100B RF drive. Then a noise-suppressing 'squarer' circuit was added to the RF resonator circuit to limit the amplification of fast voltage fluctuations. Additionally to reduce slower noise processes, a PI-controlled feedback circuit was added to the RF circuit. This also impedes the long-term drift of the motional modes. The net change was the increase of the motional coherence time from ~ 1.5 ms to ~ 70 ms.

The motional coherence time captures the impact of noise on short timescales. The motional stability of the sidebands over a longer timescale (seconds to hours) can be measured on the qubit by using Raman spectroscopy on the modes of the BSB, all whilst performing routine calibrations for experiments. During the data collection in the work of Ref. [76], frequent calibrations were taken to measure the sideband frequency and the values were added to a logging dataset in ARTIQ. To quantify this longer timescale, the Allan deviation is used, as it provides a quantitative measure of the stability and precision of frequency standards. It is a tool developed to characterise the noise present in a signal. Allan deviation measurements are thus used to characterise the logged data, however, the data is imperfect and has dead time. Instead of calculating the non-overlapping Allan deviation and interpolating between the dead time points [77], the logged data is formatted and a subset of data is selected where the time series is evenly spaced. Then, the overlapping Allan deviation is used to maximise the use of the smaller data set.

The overlapping Allan deviation σ^2_{OADEV} [78] can display a measure of the frequency stability where

$$\sigma^2_{OADEV}\left(m\tau_0\right) = \frac{1}{2\left(m\tau_0\right)^2\left(N-2m\right)} \sum_{n=1}^{N-2m} \left(x_{n+2m} - 2x_{n+1m} + x_n\right)^2, \tag{4.17}$$

where x_m is the time series of frequency data, $m\tau_0$ is the averaging time, τ_0 is the minimum time interval and N is the length of data. For a single ion, the Allan deviation for both the

radial X and Y modes is plotted in Figure 4.10. From the plot, the stability of the motional frequencies can be seen over different timescales. The analysis provides periods to define the duty cycle of experiments if an experiment is required to have a certain frequency precision. For example, in the work in Ref. [76], this plot is used to define a recalibration of motional frequencies every 6 minutes to maintain a frequency precision of < 30 Hz.

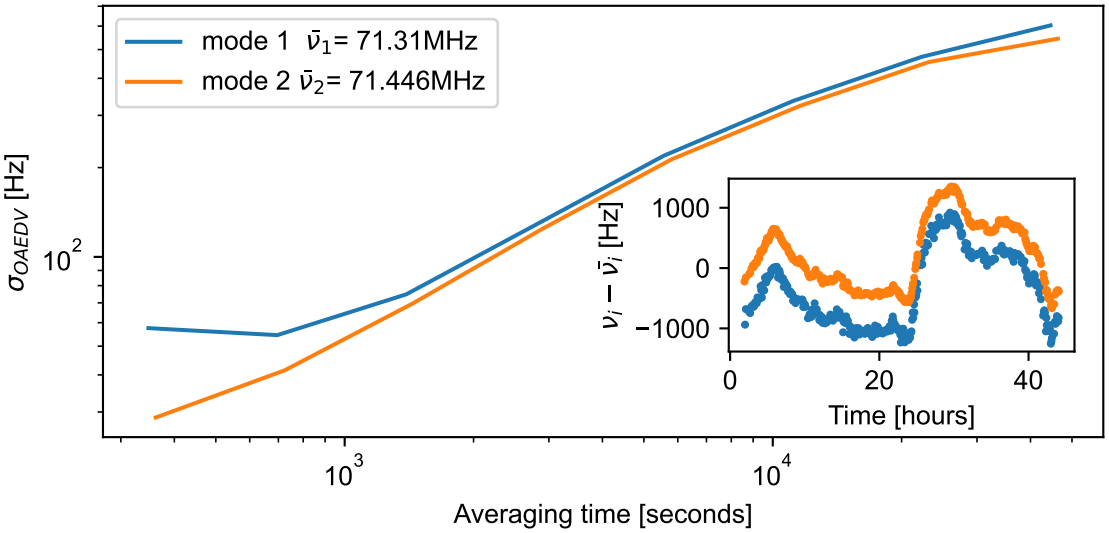

FIGURE 4.10. Single ion Allan deviation calculations measuring the BSB frequency over 40 hours. Edited from [76]. The overlapping Allan deviation is calculated for different averaging times, giving a measure of the drift over each period. **Inset**: Frequency time series data where the data collection is evenly spaced and there are no dead time points over 40 hours. The data is collected during the Geometric phase data collection period and modes 1 and 2 refer to the radial x-y modes of oscillation. The y-axis is the difference between the mode frequency and the mean mode frequency in a particular direction.

4.1.11 Experimental phase modulated gates

Modulation techniques, as mentioned in the theory section, are ubiquitous in recent applications of MS gates. The implementations of modulation can vary between ion trap laboratories, amplitude modulation in [79, 80] frequency modulation in [81, 82, 83, 84, 85] and the technique of phase modulation for entangling gates was demonstrated with high fidelity in the Yb trap [86, 87, 88]. The phase modulation technique worked well, producing entangling gates with 99.4(2)% fidelity [86]. However, the pulse upload and compilation speeds were not integrated into the software control (IGOR) and the pulses were uploaded externally via USB onto a Keysight 33600A AWG. The methods developed in this thesis extend from the

previous implementation and add phase modulation into the new control system of ARTIQ leveraging a controllable AWG with faster integrated upload and compilation speeds.

Phase and amplitude modulation can be used to control the path of the wavepacket in phase space, producing robustness and higher fidelity gates than the primitive MS gates. Phase space diagrams are often used to show the evolution of oscillators and are frequently used in displaying the motional changes to the ions. In particular, during any state-dependent force, the wavepacket of the ions is used as a visual tool to see the dynamics [47]. This can offer insights into the robustness of quantum gates or alternative bosonic states can be prepared. The conditions of the phase space trajectory can also be controlled to produce a gate that is robust to frequency errors (such as laser detuning noise). At the start of each gate, the wavefunction of the oscillator mode is cooled to its ground state and centred at the origin in phase space. Primitive Mølmer-Sørensen gates, as described before, push the wavefunction and trace a circle out in phase space, returning to the origin. The area encircled is equal to the relative phase between the ions Φ, which if equal to $\pi/4$, a maximally entangled gate is enacted. In addition to this, the detuning, amplitude and phase define the trajectory, where the detuning curves the path, amplitude defines the speed of displacement and phase defines the direction of travel. Instead of following curved lines, the optimised paths enclose trajectories in phase space according to the optimised control parameters such as amplitude, phase or frequency. This can be seen in Figure 4.11b, highlighting an optimised trajectory in phase space and by closing all of the motional modes it reduces the residual qubit-oscillator entanglement.

Modulation on the control using Q-CTRL's Boulder Opal [48, 49] was then added to the toolbox. ARTIQ scripts are enabled to switch to the AWG instead of the DDS and using Q-CTRL's pulse optimiser an arbitrary waveform is generated and the data is sent to the M8190A AWG. This waveform is then amplified and sent to the AOM to imprint the modulation onto the laser. The imprinting of the waveform onto the laser profile has a transfer function, dependent on the AOM rise time and switching speed which was characterised and shown in section A3.

4.2 Multi-partite gates

The initial Mølmer-Sørensen gate protocol can be extended to multiple ions and has been used to generate GHZ states between multiple ions in a linear Paul trap [89, 90, 91]. These states are important in the field of quantum metrology, where large ion entanglement is used for the creation of quantum mechanical sensors. They are also useful in the preparation of

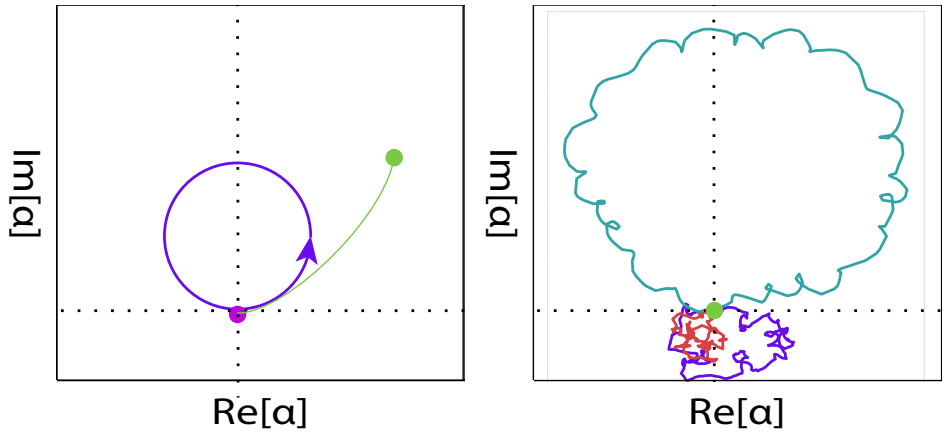

(A) Primitive trajectory (B) Optimised trajectory

FIGURE 4.11. Example Phase-Space trajectories, for primitive and optimised trajectories for the MS gate. In Figure 4.11a the path for a primitive MS gate is shown where the detuning is close to one mode, enclosing a circle (purple). The other mode, in green, is shown to be displaced and at the end of the gate time is left outside of the origin, leaving residual qubit-oscillator entanglement thus decreasing the fidelity of the target state. This displacement is exaggerated for illustration. In Figure 4.11b, an optimised path in phase space is shown, showing the trajectory of three modes. The three modes are all closed by returning to the origin at the end of the gate time, reducing the qubit-oscillator entanglement and increasing the gate fidelity. This figure is extracted from simulations of MS gates using the Q-CTRL package.

quantum circuits [92, 93, 94] , where the circuit depth in the creation of all-to-all entangled gates is greatly reduced by implementing a global entangling protocol by illuminating all the ions and entangling them in a single operation. This produces the following global entangling time evolution operator

$$U_{GE}(\tau_g) = \exp\left(i \sum_{j=1}^{N-1} \sum_{k=0}^{j-1} \psi_{jk} \sigma_x^j \sigma_x^k\right), \tag{4.18}$$

where j and k are ion indices, σ_x is the Pauli X operator and ψ_{jk} is a matrix of the relative phases between the indexed ions. For the global entangling operation to occur, the relative phase between each ion must be $\pi/4$.

There are some challenges in the production of this gate, as with the production of two-qubit entanglement. The design of the gates has to be robust to experimental errors and noise. Fidelity tends to decrease with a large ion crystal, due to superdecoherence and the increase in the number of modes and ions [90]. When creating a global entangling gate via the Mølmer-Sørensen interaction, the presence of the additional motional modes can lead to a

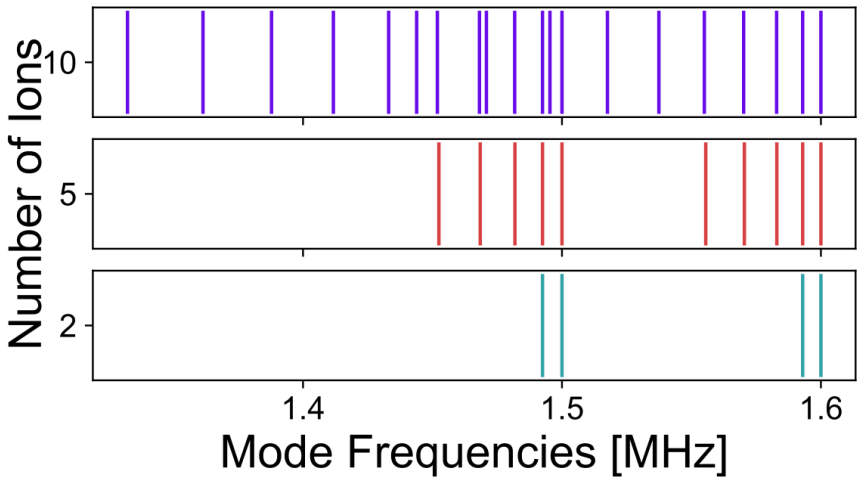

FIGURE 4.12. Motional mode crowding demonstration showing the spacing between the frequencies decreasing as the number of ions increases. Each line is a motional mode frequency as a single point and as the number of ions increases the number of modes scales proportionally. If the two radial modes in question are space by 100kHz, then for Ytterbium ions the modes will begin to overlap and fast gates can cause spectator modes to be excited.

loss of gate fidelity. One of the reasons this occurs is because of the crowding of motional modes. In Figure 4.12, as the number of ions increases the motional modes appear closer and then when quickly driving the ions with a set MS detuning, spectator motional modes may instead be displaced. Additionally, non-uniform laser illuminations lead to an unequal Rabi rate reducing the final state fidelity.

There have been several quantum control methods suggested to reduce gate infidelity by modulation of the laser-induced spin-motion interaction, thereby managing the spectator motional modes and permitting robust evolutions. For example, the collaborative effort between QCL and Q-CTRL [86, 88, 87] on phase-modulated gate sequences uses the spectator modes to create relative phase between the ions in the chain and ensure that at the end of the gate time, the modes are all closed. The optimisation of pulse schemes grows in complexity with larger qubits [89], indicating that this technique may not scale well to higher ion registers in linear Paul traps.

4.2.1 Simulation of phase and amplitude modulated gates

The phase modulation entangling gate protocol in [86, 88] demonstrates the creation of arbitrary qubit entanglement in trapped ion registers. As mentioned in the paper, the framework is extensible to multi-partite entangling gates. In this subsection, an overview of the numerical

tool is shown and simulation results and analysis for GHZ states are presented, extending the work on discrete phase modulated gates. Fast, error-robust gates are generated by using a gradient-based numerical optimisation tool, custom-built in TensorFlow. The graph is based on an interaction Hamiltonian parametrised by modulated controls modelled as a complex drive.

The drive is a complex piecewise constant signal, where each segment has an optimisable phase and amplitude. The outputs of this graph are the amplitude and phase control signals to modulate the laser drive. The drives are generated by minimising a cost function C, where

$$\mathcal{C} = \sum_{\substack{j=1 \\ k<j}}^{N} (\epsilon_{jk})^2 + \sum_{j=1}^{N} \sum_{p=1}^{M} \left|\alpha_j^p(\tau)\right|^2, \tag{4.19}$$

where $(\epsilon_{jk})^2$ is an infidelity term based on the entangling phase error such that $\epsilon_{jk} \equiv \psi_{jk} - (\phi_{jk}(\tau) + \phi_{kj}(\tau))$. Here ψ_{jk} refers the target phase in Equation 4.18 and ϕ_{jk} are the acquired phases between the ions. $\left|\alpha_j^p(\tau)\right|^2$ quantifies the error for residual spin-oscillator entanglement at gate time τ. This cost function is used as it provides a faster approach to determining the control pulse error than by using the full infidelity defined by the trace norm of the control propagator $U(\tau)$ and the target MS propagator U_C.

The output pulses of the graph are then sent to the AWG, which produces a signal modulating the 70 arm of the Raman laser beam.

4.2.2 Extension to multi-partite systems

To modify the optimisation tool to demonstrate global entangling gates, the simulation parameters must be edited (namely the controls and target Hamiltonian). Instead of creating a two-qubit entanglement between the ions in large registers, the target state was altered to produce GHZ states and represent the Yb system. Firstly, instead of each ion having its own optimisable control, the graph was edited to have a single global drive affecting every qubit simultaneously. Whilst this introduces a reduction in controllable parameters, it more accurately describes the global entangling hardware used in the lab.

Q-CTRL's MS package optimises for a target relative phase between the ions, where if two ions differ by $\pi/4$ the entangled state is produced as in Equation 4.19. Simulations were set up by populating the target phase matrix with a full strictly lower triangular matrix of $\pi/4$ and optimising for different scanned gate times, with a set Rabi frequency of $\Omega = 33$ kHz. With larger ion registers, the gates take longer to compute, due to the expanded Hilbert space.

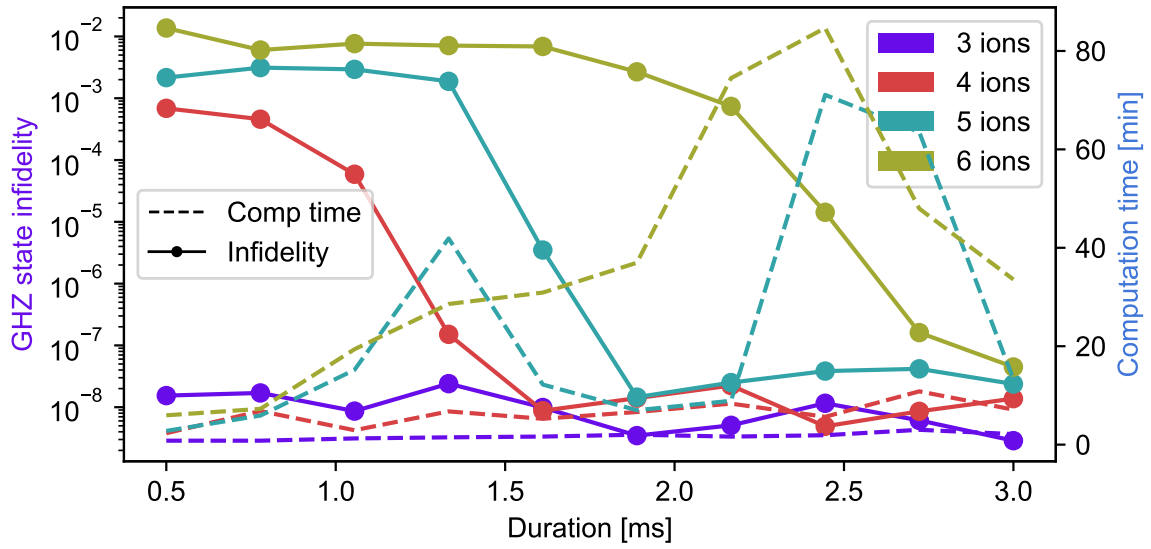

FIGURE 4.13. This implementation shows the work done on the simulation of MS gates in larger ion registers, creating GHZ states between all of the ions in the trap. Placeholder, update with new colours, fonts etc. Parallelised Q-CTRL graph optimisation runs and is calculated over multiple different durations. Larger durations are required to close the additional motional modes introduced by the crowding.

Infidelity scaling with several ions is seen in the Figure 4.13, where the other axis is populated with the computation time.

The number of segments is constrained by the duration of the gate, with a fixed segment rate of 80 per millisecond. In general, adding more segments provides more degrees of freedom for the optimiser and can improve the gate fidelity. However, there is a hardware limitation on the experiment, where a larger segment rate causes higher frequency voltage changes, falling outside the AOM's bandwidth.

Analysing the Figure 4.13, for larger ion gates, the phase-modulated sequences take a longer time to be optimised. This is owing to the larger Hilbert space complexity from adding in more ions and thus more motional modes, taking longer for the optimiser to generate entanglement and find paths with low residual qubit-oscillator entanglement. For lower ion numbers, it takes less gate time to produce a GHZ state. Additionally, the computational time is lower and the fidelity floor is lower. The key result from this plot shows that for phase-modulated entangling gates creating GHZ states, there is a tradeoff between achieving high-fidelity gates whilst keeping the pulse optimisation time low. This can be varied by the duration of the gate time.

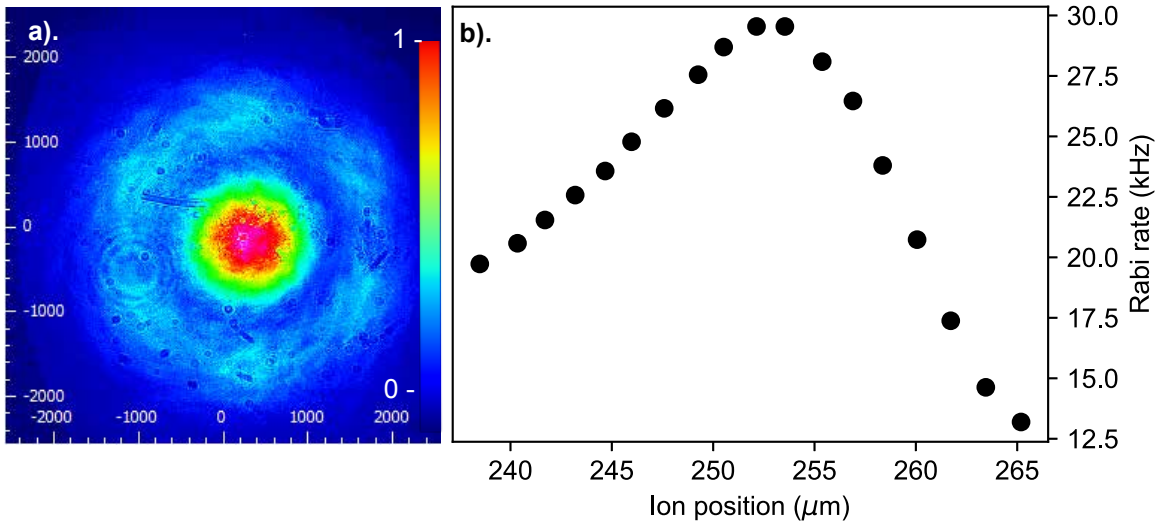

FIGURE 4.14. a). Scaled Raman beam profiling data was taken on the 200 Arm of the beam path before the focusing optics, using a Thorlabs beam profiler. ND filters were placed before the profiler hence the intensity is in arbitrary units. The beam profile can be seen to be Gaussian in intensity. Profiling measurements were also taken for the other arm of the laser. b). Rabi rate against ion position measurements for the Yb trap, data from [95]. Using the DC electrodes and offsetting the voltage on C0 of the ISEG, a singular ion is moved around in the trap. Each point is created from a Raman carrier time scan and the pi time is fit based on the scan results. The Gaussian intensity profile can be seen on the ion, where the shape could be described as a convolution of both of the intensity fields.

4.2.3 Amplitude inhomogeneity

Two non-co-propagating Raman laser beams are focused down onto the ions in the trap, driving the MS interaction. Whilst this provides a benefit in smaller ion registers by driving with faster Rabi frequency, it can cause non-equal illumination of the ions in a large ion chain. In the production of multipartite entanglement, the impact on the fidelity by amplitude differences is investigated.

To characterise the effect on the MS gate, the illumination profile on the ions is experimentally extracted. The beam profiles of each of the beams were measured and the Rabi rates at different ion positions were extracted. With a single ion in the trap, the ion position with respect to the Raman field can be adjusted by applying a voltage offset to one of the end-cap DC electrodes. By driving the carrier to perform π-time measurements, the Rabi frequency of the driving field is found at each position in the trap. The results are presented in Figure 4.14.

The minimum inter ion spacing $x_{\min}(N)$ for an ion chain length N is found from [35]

$$x_{\min}(N) = \left(\frac{Z^2e^2}{4\pi\epsilon_0 M\omega_z^2}\right)^{1/3} \frac{2.018}{N^{0.559}}, \tag{4.20}$$

where Z is the degree of ionisation, e is the electron charge, M is the mass of each ion, ω_z is the axial frequency and ϵ_0 is the permittivity of free space. From the experiment and previous calculations of the inter-ion spacing, the FWHM of the beam is 50 μm where the ion spacing is 5.5 μm. This means that as the ion number increases the amplitude inhomogeneity should not be neglected in the Yb trap. The ion position data is interpolated to further investigate the effect, and the simulation of phase-modulated global entangling gates is completed.

The effect of amplitude inhomogeneity on the creation of GHZ states is then investigated, where each ion can be simulated in the Boulder Opal suite with a varying control pulse maximum Rabi rate. Leveraging the optimisation input tools, a singular optimisation variable is created representing the global drive. This then can have an amplitude map applied, giving different amplitude effects on each ion, reducing the maximum Rabi rate for outer ions in the chain. To calculate this map, the beam profile data in Figure 4.14 was interpolated. Then, an array of ions with size N was sampled, each having the minimum inter-ion distance between them.

To find the inter-ion distance for different ion chain lengths, the experimental value for two ions of 5.5 μm was taken from Equation 4.20 and then a ratio applied when changing between ion number, so that $x_{\min}(N) = 5.5\mu\text{m} \times 2^{0.559}/N^{0.559}$. In practice, the ions will diverge even more at the edges due to the increased axial Coulomb force, exacerbating the amplitude inhomogeneity. The ion position eigenvalues were not used and the ions were assumed to be separated by a constant $x_{\min}$. Then the ions were placed at the centre of the experimental beam profile and the theoretical amplitude was then calculated by sampling the interpolated function at each of the ion points. This provides the map to then use for the control drive onto each ion and the simulation can be parallelised and run for multiple ion lengths.

If the beam profile is then altered, the effect on the fidelity of the MS gate can be seen. By applying a scanned multiplication factor onto $x_{\min}(N)$ from $[0.5\times, 6\times]$ and then rerunning simulations of the GHZ state production, the effect of focussing or broadening a beam is applied. The simulation results are shown in Figure 4.15, where for different ion numbers, the standard deviation of the control amplitudes σ_{amp} is shown. The σ_{amp} is related to the inverse of the FWHM of the Raman beam, as a larger amplitude spread between the drives incurs a lower FWHM of the applied global Raman beam. For a larger spread in the amplitudes affecting the ion, a higher infidelity is given, related to a power law. To achieve an infidelity

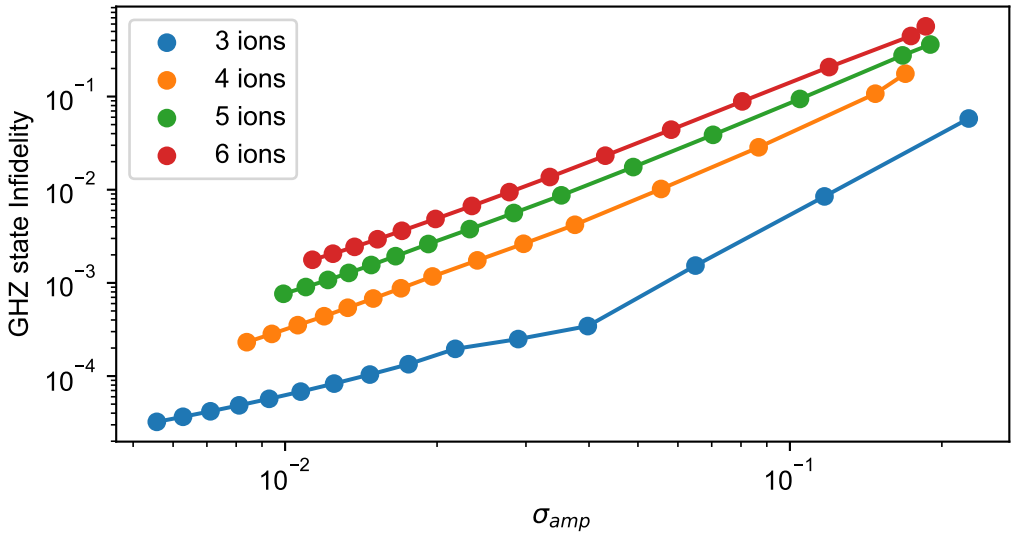

FIGURE 4.15. Simulation results for GHZ states created with phase and amplitude modulated pulses in the Boulder Opal suite. Maximum Rabi frequency used is $\Omega = 2\pi \times 33$ kHz, with a fixed gate time of 1ms and 80 segments per ms. Log-log plot, noting a power law relationship between the infidelity and σ_{amp}. The x-axis shows the amplitude standard deviation between the ions, where the experimental Gaussian profile is interpolated to generate the control amplitudes for each ion. An additional scaling is applied to tighten or broaden the profile. The simulations are parallelised with 10 iterations to reduce run time.

of below 10^{-3} for 3 ions, a standard deviation of control amplitudes $\sigma_{amp} < 6 \times 10{-}2$ is required. For larger ion numbers, the infidelity scales up accordingly, for 6 ions to achieve a GHZ state infidelity of 10^{-2} then the $\sigma_{amp} < 2 \times 10^{-2}$. The Gaussian beam profile can thus increase experimental error on the production of GHZ states, reducing the maximum achievable infidelity.

4.2.4 Multitone

Another quantum control method proposed is that of multitones [96, 97], where the sideband fields are not modulated, however, there are multiple tones with pre-optimised frequencies and varying amplitudes. This technique potentially offers more scalability than the aforementioned because dependent on the setup, arbitrary PSTs can be created with less optimisation parameters. In ref. [96], a high-fidelity global MS gate is produced using multitones. The frequencies of the tones are set to harmonics of the gate time, detuned away from the motional modes and the bandwidth encompasses the normal mode frequencies. The amplitudes of each

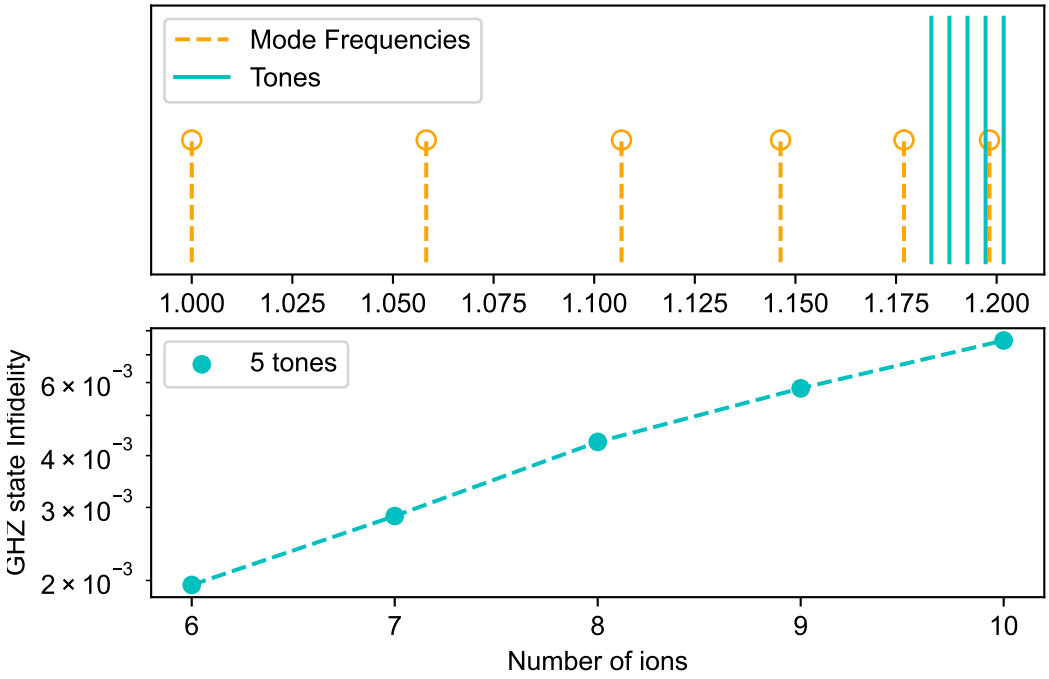

FIGURE 4.16. Tone frequencies for six ions and five-tone optimisation. Here each tone is spaced 6 kHz apart, spanning 30 kHz. The six radial frequencies for one axis are shown. Each tone is an optimisable variable in Q-CTRL, with amplitude and phase modulation. The bottom panel shows the results for the new multitone with phase modulation approach in simulation. 6 to 10 ions are prepared in GHZ states and their fidelities are extracted. The gate time for each simulation is 5 ms, with a maximum Rabi rate of 6.6kHz for each tone and 10 optimisable segments over the 5 ms gate period.

of the tones are then numerically optimised to reduce the gate infidelity. The effect of this process is a non-primitive phase space trajectory, similar to the effect of other modulation sequences [98].

For this thesis, a novel variation of the multitone approach was developed. Instead of having fixed amplitudes throughout the pulse, each tone was added as an optimisation variable. This means that every tone added has its own amplitude and phase modulation applied. The graph optimisation process from Q-CTRL's Boulder Opal [48, 49] was used to test if it was better to perform globally entangling gates than with the phase-modulated optimisation sequences.

Various tone frequencies were trialled, with varying tone separation and amount of tones. It was found for higher amounts of tones and segments the optimisation would take too long to converge and would time out. The most consistent optimisation method used was five

tones each separated with 6 kHz, with one of the tones detuned away from the mode with the highest mode frequency ω_1 where $\omega_1 = \max(\omega_{bsb/rsb} - \omega_{carrier})$. For 4 ions, the range in frequency space of five tones spanning the radial modes is shown in Figure 4.16. This novel method was then simulated to produce GHZ states at different ion numbers ranging from 6 to 10 ions. Each tone has equal illumination amplitude on the ions and the maximum Rabi rate is 6.6 kHz. The graph optimisations have a gate duration of 5ms.

This result is compared against simulations of the same duration but using the traditional phase-modulated sequences. As each tone contributes to the field driving Rabi oscillations, the maximum Rabi rate of each tone must be scaled to create an equal comparison between phase modulation and the multitone case. The maximum Rabi rate of each tone is then $\Omega_{MTM} = \Omega_{\Phi M}/5$, where Ω_{MTM} is the Rabi rate for the multitones and $\Omega_{\Phi M}$ for the phase modulated comparison. In addition to this, only 10 segments are permitted for the multitone method whereas the phase-modulated sequences have a fixed segment rate. The pulses generated are shown in the appendix in Figure 4.16.

Gate solutions were found for the multitone sequences within these bounds, whereas the phase-modulated sequences would take a lot longer to find solutions for 6 and 7 ions and at >7 ions were unable to find control pulses which produce GHZ inducing gates. The infidelities for the multitone scheme with 5 amplitude and phase-modulated pulses are shown in Figure 4.16.

Overall, the choice between phase-modulated or multitone sequences should not affect robustness to motional decoherence, as this is determined from the PST [98] and both methods give arbitrary control to the PST. Further power budget comparisons and robustness investigations must be drawn between the two methods. Additionally, to confirm the multitone method's versatility at higher ion numbers, the arbitrary pulses should be used to drive AOMs and the pulses experimentally confirmed on the ion.

CHAPTER 5

Conclusion

In this thesis, the construction of a two-species trap was performed, detailing the design of the components required to trap $^{171}Yb^{+}$and $^{176}Lu^{+}$outlined in chapter 3. This system has been used to demonstrate the trapping of $^{171}Yb^{+}$and $^{174}Yb^{+}$. Additionally, the Yb trap was migrated to a new control software, ARTIQ, along with gradual improvements to the state detection and experimental control. This was performed to improve entangling gates calibration and execution. A novel multitone method was developed, combining AM and PM with multitone gates. It appears to offer more flexibility, allowing for the creation of GHZ states in long ion chains. Additionally, multitone entangling gates were investigated along with global entangling gates and their impact due to experimental imperfections, such as amplitude inhomogeneity. This work fits into the broader research field, as quantum control methodologies are being used to develop and refine the processes in ion trapping and other quantum computing architectures.

Updates to the experimental system are continually being made, with new lasers and features to existing setups being added to improve the ease of trapping and qubit manipulation.

5.1 Future outlook

Looking forwards, the Yb-Lu trap should be characterised for lutetium, with the lasers addressing and oven fluoresence demonstrated with the lutetium ovens. After this is completed, experiments harnessing Lu's electronic energy level structure should be completed demonstrating its capability as a qutrit and sympathetic cooling. The qutrit energy level structure in lutetium provides an avenue to explore further quantum chemistry experiments where mixed-qudit-boson simulators are required [99]. This can allow the simulation of more complex molecules than can be achieved in a qubit-boson simulator like the Yb trap. Single ion addressing is also being enabled in the Yb trap and this is to be completed in the Yb-Lu trap. The mechanism to enable this differs, as it will be sent through one of the horizontal viewports instead of addressing through the objective lens. To achieve this, a reentrant window must

replace a horizontal viewport in the vacuum chamber, as it will allow tighter focussing optics onto the ion plane. The individual addressing will give increased qubit control, allowing multiple individual qubits to be altered and can also improve the capability of the trap to perform complex quantum simulations or selective entangling gates.

Entangling operations are essential to achieving fault-tolerant quantum computation as single qubit gates along with entangling operations provides universal quantum computation. In addition, multipartite qubit entanglement can be used in sensing operations and quantum algorithms to reduce their gate depth. With regards to the Yb trap, further improvements to the entangling operations can be performed to push the fidelity as high as possible. This thesis aligns with ongoing research, aiming to not only increase the fidelity of entangling operations but also demonstrate their robustness and high-fidelity multipartite capabilities. Additional experiments, including multiple ion phase modulation schemes and beam shaping experiments to create a flat-top profile for the Raman laser, are envisioned to improve fidelity and verify the experimental advantages of achieving equal illumination for the production of Greenberger-Horne-Zeilinger (GHZ) states. Finally, the novel multitone scheme can be performed on the experiment to characterise and compare this technique to phase modulation and regular multitone schemes.

Overall, the ion traps in the Quantum Control Laboratory are continually being upgraded in order to increase the precision of the traps and their computing capability. The field is expanding in popularity and reach, leading to the isolation of larger arrays of qubits for intricate simulations, such as those completed at the QCL on chemical dynamics. Quantum Control efforts are concurrently addressing qubit development, aiming to provide error robustness and enhance operation fidelity. The synergy of effective quantum control and the use of larger qubit arrays holds the promise of practical applications for quantum computing, with the prospect of meaningful integration into our society.

Bibliography

[1] Richard P Feynman. 'Simulating physics with computers'. In: *International Journal of Theoretical Physics* 21.6–7 (1982), pp. 467–488. ISSN: 0020-7748. DOI: 10.1007/bf02650179.

[2] G E Moore. 'Cramming More Components Onto Integrated Circuits'. In: *Proceedings of the IEEE* 86.1 (1998), pp. 82–85. ISSN: 0018-9219. DOI: 10.1109/jproc.1998.658762.

[3] G. E. Moore. 'Progress in Digital Integrated Electronics'. In: *Technical Digest 1975. International Electron Devices Meeting*. IEEE. 1975, pp. 11–13.

[4] Max Born. 'Statistical Interpretation of Quantum Mechanics'. In: *Science* 122.3172 (1955), pp. 675–679. ISSN: 0036-8075. DOI: 10.1126/science.122.3172.675.

[5] F. T. Arecchi et al. 'Atomic Coherent States in Quantum Optics'. In: *Phys. Rev. A* 6 (6 Dec. 1972), pp. 2211–2237. DOI: 10.1103/PhysRevA.6.2211. URL: https://link.aps.org/doi/10.1103/PhysRevA.6.2211.

[6] L. M. Narducci, C. Alton Coulter and Charles M. Bowden. 'Exact diffusion equation for a model for superradiant emission'. In: *Phys. Rev. A* 9 (2 Feb. 1974), pp. 829–845. DOI: 10.1103/PhysRevA.9.829. URL: https://link.aps.org/doi/10.1103/PhysRevA.9.829.

[7] Michael A. Nielsen and Isaac L. Chuang. *Quantum Computation and Quantum Information: 10th Anniversary Edition*. Cambridge University Press, 2011. ISBN: 9781107002173.

[8] John P Gaebler et al. 'High-fidelity universal gate set for be 9+ ion qubits'. In: *Physical review letters* 117.6 (2016), p. 060505.

[9] CJ Ballance et al. 'High-fidelity quantum logic gates using trapped-ion hyperfine qubits'. In: *Physical review letters* 117.6 (2016), p. 060504.

[10] Daniel M. Greenberger, Michael A. Horne and Anton Zeilinger. 'Going Beyond Bell's Theorem'. In: *arXiv e-prints*, arXiv:0712.0921 (Dec. 2007), arXiv:0712.0921. DOI: 10.48550/arXiv.0712.0921. arXiv: 0712.0921 [quant-ph].

[11] Anders Sørensen and Klaus Mølmer. 'Entanglement and quantum computation with ions in thermal motion'. In: *Physical Review A* 62.2 (2000), p. 022311. ISSN: 1050-2947. DOI: 10.1103/physreva.62.022311.

[12] Anders Sørensen and Klaus Mølmer. 'Quantum Computation with Ions in Thermal Motion'. In: *Physical Review Letters* 82.9 (1999), pp. 1971–1974. ISSN: 0031-9007. DOI: 10.1103/physrevlett.82.1971.

[13] A. Wallraff et al. 'Strong Coupling of a Single Photon to a Superconducting Qubit Using Circuit Quantum Electrodynamics'. In: *Nature* 431.7005 (Sept. 2004), pp. 162–167. DOI: 10.1038/nature02851.

[14] John M. Martinis et al. 'Rabi Oscillations in a Large Josephson-Junction Qubit'. In: *Phys. Rev. Lett.* 89 (11 Aug. 2002), p. 117901. DOI: 10.1103/PhysRevLett.89.117901. URL: https://link.aps.org/doi/10.1103/PhysRevLett.89.117901.

[15] A. J. Berkley et al. 'Entangled Macroscopic Quantum States in Two Superconducting Qubits'. In: *Science* 300.5625 (2003), pp. 1548–1550. ISSN: 0036-8075, 1095-9203. URL: http://www.jstor.org/stable/3834468 (visited on 06/11/2023).

[16] R. Hanson, O. Gywat and D. D. Awschalom. 'Room-Temperature Manipulation and Decoherence of a Single Spin in Diamond'. In: *Phys. Rev. B* 74 (2006), p. 161203. DOI: 10.1103/PhysRevB.74.161203.

[17] M. V. G. Dutt et al. 'Quantum Register Based on Individual Electronic and Nuclear Spin Qubits in Diamond'. In: *Science* 316 (2007), pp. 1312–1316. DOI: 10.1126/science.1139831.

[18] A. Imamoglu et al. 'Quantum Information Processing Using Quantum Dot Spins and Cavity QED'. In: *Phys. Rev. Lett.* 83 (1999), pp. 4204–4207. DOI: 10.1103/PhysRevLett.83.4204.

[19] J. R. Petta et al. 'Coherent Manipulation of Coupled Electron Spins in Semiconductor Quantum Dots'. In: *Science* 309 (2005), pp. 2180–2184. DOI: 10.1126/science.1116955.

[20] D. Englund et al. 'Controlling the Spontaneous Emission Rate of Single Quantum Dots in a Two-Dimensional Photonic Crystal'. In: *Phys. Rev. Lett.* 95 (2005), p. 013904. DOI: 10.1103/PhysRevLett.95.013904.

[21] R. Hanson et al. 'Spins in Few-Electron Quantum Dots'. In: *Rev. Mod. Phys.* 79 (2007), pp. 1217–1265. DOI: 10.1103/RevModPhys.79.1217.

[22] J. I. Cirac and P. Zoller. 'Quantum Computations with Cold Trapped Ions'. In: *Phys. Rev. Lett.* 74 (20 May 1995), pp. 4091–4094. DOI: 10.1103/PhysRevLett.74.4091. URL: https://link.aps.org/doi/10.1103/PhysRevLett.74.4091.

[23] R. Blatt and C. F. Roos. 'Quantum Simulations with Trapped Ions'. In: *Nature Physics* 8 (2012), p. 277. DOI: 10.1038/nphys2252.

[24] D. Leibfried et al. 'Quantum Dynamics of Single Trapped Ions'. In: *Rev. Mod. Phys.* 75 (2003), pp. 281–324. DOI: 10.1103/RevModPhys.75.281.

[25] R. Blatt and D. Wineland. 'Entangled States of Trapped Atomic Ions'. In: *Nature* 453 (2008), p. 1008. DOI: 10.1038/nature07125.

[26] H. Häffner, C. Roos and R. Blatt. 'Quantum Computing with Trapped Ions'. In: *Physics Reports* 469 (2008), pp. 155–203. DOI: 10.1016/j.physrep.2008.09.003.

[27] D. J. Wineland, R. E. Drullinger and F. L. Walls. 'Radiation-Pressure Cooling of Bound Resonant Absorbers'. In: *Phys. Rev. Lett.* 40 (25 June 1978), pp. 1639–1642. DOI: 10.1103/PhysRevLett.40.1639. URL: https://link.aps.org/doi/10.1103/PhysRevLett.40.1639.

[28] Wolfgang Paul. 'Electromagnetic traps for charged and neutral particles'. In: *Rev. Mod. Phys.* 62 (3 July 1990), pp. 531–540. DOI: 10.1103/RevModPhys.62.531. URL: https://link.aps.org/doi/10.1103/RevModPhys.62.531.

[29] Hans G. Dehmelt. 'Radiofrequency Spectroscopy of Stored Ions I: Storage'. In: *Advances in atomic and molecular physics* 3 (1968), pp. 53–72. URL: https://api.semanticscholar.org/CorpusID:94044670.

[30] University of Innsbruck. *Trapped Ions Research Group*. Accessed: November 2023.

[31] Maciej Malinowski. 'Unitary and Dissipative Trapped-Ion Entanglement Using Integrated Optics'. en. Doctoral Thesis. Zurich: ETH Zurich, 2021. DOI: 10.3929/ethz-b-000516613.

[32] Alistair Robertson Milne. 'Construction of a linear ion trap and engineering controlled spin-motional interactions'. PhD thesis. 2021. URL: https://hdl.handle.net/2123/25869.

[33] F M Arscott. 'Theory and Application of Mathieu Functions. By N. W. Mclachlan. Pp. xii, 401. (Dover, New York.)' In: *The Mathematical Gazette* 52.379 (1968), pp. 94–95. ISSN: 0025-5572. DOI: 10.2307/3614519.

[34] D J Berkeland et al. 'Minimization of ion micromotion in a Paul trap'. In: *Journal of Applied Physics* 83.10 (1998), pp. 5025–5033. ISSN: 0021-8979. DOI: 10.1063/1.367318.

[35] D. F. V. James. 'Quantum dynamics of cold trapped ions with application to quantum computation'. In: *Applied Physics B* 66.2 (1998), pp. 181–190. DOI: 10.1007/s003400050373. URL: https://doi.org/10.1007/s003400050373.

[36] G Gabrielse et al. 'First capture of antiprotons in a Penning trap: a kiloelectronvolt source'. In: *Physical review letters* 57.20 (1986), p. 2504.

[37] Dana Berkeland and Daisy Raymondson. 'Quantum Information and Spectroscopy with Trapped Strontium Ions'. In: *APS Division of Atomic, Molecular and Optical Physics Meeting Abstracts*. APS Meeting Abstracts. May 2002, P6.041, P6.041.

[38] Ting Rei Tan. 'High-Fidelity Entangling Gates with Trapped-Ions'. B.S., National University of Singapore, 2009. Doctoral Dissertation. Department of Physics: University of Colorado, 2016.

[39] Andrew M Steane. 'The ion trap quantum information processor'. In: *arXiv preprint quant-ph/9608011* (1996).

[40] S Debnath et al. 'Demonstration of a small programmable quantum computer with atomic qubits'. In: *arXiv* (2016). DOI: 10.48550/arxiv.1603.04512.

[41] K. J. Arnold et al. 'Blackbody radiation shift assessment for a lutetium ion clock'. In: *Nature Communications* 9.1 (2018). Lutetium paper, p. 1650. DOI: 10.1038/s41467-018-04079-x.

[42] Xiande Samuel Wang. 'Spectroscopy of $^{176}Lu^{+}$ using an ion trap'. B.Sc. (Hons.) Master of Science thesis. National University of Singapore, Sept. 2017.

[43] Rattakorn Kaewuam. 'Development of an Optical Atomic Clock Based on Trapped Lutetium Ions'. In: (2020).

[44] U. Georg et al. 'Laser spectroscopy investigation of the nuclear moments and radii of lutetium isotopes'. In: *The European Physical Journal A - Hadrons and Nuclei* 3.3 (1998), pp. 225–235. ISSN: 1434-6001. DOI: 10.1007/s100500050172.

[45] N B Delone and Vladimir P Krainov. 'AC Stark shift of atomic energy levels'. In: *Physics-Uspekhi* 42.7 (July 1999), p. 669. DOI: 10.1070/PU1999v042n07ABEH000557. URL: https://dx.doi.org/10.1070/PU1999v042n07ABEH000557.

[46] S. H. Autler and C. H. Townes. 'Stark Effect in Rapidly Varying Fields'. In: *Phys. Rev.* 100 (2 Oct. 1955), pp. 703–722. DOI: 10.1103/PhysRev.100.703. URL: https://link.aps.org/doi/10.1103/PhysRev.100.703.

[47] Christophe Henri Valahu. 'Robust laser-free entanglement with trapped ions'. PhD thesis. Imperial College London, Apr. 2022. DOI: 10.25560/105029. URL: http://hdl.handle.net/10044/1/105029.

[48] Harrison Ball et al. 'Software tools for quantum control: improving quantum computer performance through noise and error suppression'. In: *Quantum Science and Technology* 6.4 (2021), p. 044011. DOI: 10.1088/2058-9565/abdca6. URL: https://doi.org/10.1088/2058-9565/abdca6.

[49] Q-CTRL. *Boulder Opal*. https://q-ctrl.com/boulder-opal. [Online]. 2023.

[50] Sébastien Bourdeauducq et al. *ARTIQ 1.0*. Version 1.0. May 2016. DOI: 10.5281/zenodo.51303. URL: https://doi.org/10.5281/zenodo.51303.

[51] Wilhelm Magnus. 'On the exponential solution of differential equations for a linear operator'. In: *Communications on Pure and Applied Mathematics* 7.4 (1954), pp. 649–673. DOI: https://doi.org/10.1002/cpa.3160070404.

[52] I Pogorelov et al. 'Compact Ion-Trap Quantum Computing Demonstrator'. In: *PRX Quantum* 2.2 (2021), p. 020343. DOI: 10.1103/prxquantum.2.020343.

[53] J. D. Siverns et al. 'On the application of radio frequency voltages to ion traps via helical resonators'. In: *Applied Physics B* 107.4 (2012), pp. 921–934. ISSN: 0946-2171. DOI: 10.1007/s00340-011-4837-0.

[54] Matthias Brandl. 'Towards cryogenic scalable quantum computing with trapped ions'. PhD thesis. 2016.

[55] American Society of Mechanical Engineers (ASME). *Pressure Boundary Bolted Flange Joint Assembly*. ASME, 2022, p. 116. ISBN: 9780791875384.

[56] Albert Einstein, Boris Podolsky and Nathan Rosen. 'Can Quantum-Mechanical Description of Physical Reality be Considered Complete?' In: *Physical Review* 47.10 (1935), pp. 777–780.

[57] Erwin Schrödinger. 'Die gegenwärtige Situation in der Quantenmechanik'. In: *Naturwissenschaften* 23 (1935), pp. 807–812, 823–828, 844–849.

[58] R. Srinivas et al. 'High-fidelity laser-free universal control of trapped ion qubits'. In: *Nature* 597.7875 (2021), pp. 209–213. DOI: 10.1038/s41586-021-03809-4. URL: https://doi.org/10.1038/s41586-021-03809-4.

[59] Craig R. Clark et al. 'High-Fidelity Bell-State Preparation with $^{40}Ca^{+}$ Optical Qubits'. In: *Phys. Rev. Lett.* 127 (13 Sept. 2021), p. 130505. DOI: 10.1103/PhysRevLett.127.130505. URL: https://link.aps.org/doi/10.1103/PhysRevLett.127.130505.

[60] Leon Riesebos, Brad Bondurant and Kenneth R. Brown. 'Universal Graph-Based Scheduling for Quantum Systems'. In: *IEEE Micro* 41.5 (2021), pp. 57–65. DOI: 10.1109/MM.2021.3094968.

[61] Leon Riesebos, Brad Bondurant and Kenneth R. Brown. 'Universal Graph-Based Scheduling for Quantum Systems'. In: *IEEE Micro* 41.5 (2021), pp. 57–65. DOI: 10.1109/MM.2021.3094968.

[62] Brand Fortner. 'HDF: The hierarchical data format'. In: *Dr Dobb's J Software Tools Prof Program* 23.5 (1998), p. 42.

[63] C. Monroe et al. 'Resolved-Sideband Raman Cooling of a Bound Atom to the 3D Zero-Point Energy'. In: *Phys. Rev. Lett.* 75 (22 Nov. 1995), pp. 4011–4014. DOI: 10.1103/PhysRevLett.75.4011. URL: https://link.aps.org/doi/10.1103/PhysRevLett.75.4011.

[64] Dl Wineland and Hans Dehmelt. 'Proposed 1014 delta upsilon less than upsilon laser fluorescence spectroscopy on t1+ mono-ion oscillator iii'. In: *Bulletin of the American Physical Society*. Vol. 20. 4. AMER INST PHYSICS CIRCULATION FULFILLMENT DIV, 500 SUNNYSIDE BLVD, WOODBURY ... 1975, pp. 637–637.

[65] L. Feng et al. 'Efficient Ground-State Cooling of Large Trapped-Ion Chains with an Electromagnetically-Induced-Transparency Tripod Scheme'. In: *Phys. Rev. Lett.* 125 (5 July 2020), p. 053001. DOI: 10.1103/PhysRevLett.125.053001. URL: https://link.aps.org/doi/10.1103/PhysRevLett.125.053001.

[66] Giovanni Morigi, Jürgen Eschner and Christoph H. Keitel. 'Ground state laser cooling using electromagnetically induced transparency'. In: *Physical Review Letters* 85 (2000), p. 4458. DOI: 10.1103/PhysRevLett.85.4458.

[67] Michael Ma. 'Towards efficient ground-state laser cooling of Ytterbium ion chains in a linear Paul trap using electromagnetically induced transparency'. Bachelor of Science (Honours) thesis. School of Physics, Faculty of Science, May 2022.

[68] Pauli Virtanen et al. 'SciPy 1.0: Fundamental Algorithms for Scientific Computing in Python'. In: *Nature Methods* 17 (2020), pp. 261–272. DOI: 10.1038/s41592-019-0686-2.

[69] Chris Ballance. *andorEmccd*. https://github.com/cjbe/andorEmccd. 2019.

[70] Stéfan van der Walt et al. 'scikit-image: image processing in Python'. In: *PeerJ* 2 (June 2014), e453. ISSN: 2167-8359. DOI: 10.7717/peerj.453. URL: https://doi.org/10.7717/peerj.453.

[71] C. L. Edmunds et al. 'Scalable hyperfine qubit state detection via electron shelving in the $^2D_{5/2}$ and $^2F_{7/2}$ manifolds in $^{171}\mathrm{Yb}^+$'. In: *Phys. Rev. A* 104 (1 July 2021), p. 012606. DOI: 10.1103/PhysRevA.104.012606. URL: https://link.aps.org/doi/10.1103/PhysRevA.104.012606.

[72] A. E. Webb et al. 'Resilient Entangling Gates for Trapped Ions'. In: *Physical Review Letters* 121.18 (Nov. 2018), p. 180501.

[73] J. Randall et al. 'Generation of high-fidelity quantum control methods for multilevel systems'. In: *Phys. Rev. A* 98 (Oct. 2018), p. 043414.

[74] Tim Fabian Wohlers-Reichel. 'Engineering interactions for analog simulation of quantum chemistry in a linear Paul Trap'. 2022. URL: https://hdl.handle.net/2123/27748.

[75] D. M. Lucas et al. *A long-lived memory qubit on a low-decoherence quantum bus*. 2007. arXiv: 0710.4421 [quant-ph].

[76] C. H. Valahu et al. 'Direct observation of geometric-phase interference in dynamics around a conical intersection'. In: *Nature Chemistry* (2023). DOI: 10.1038/s41557-023-01300-3. URL: https://doi.org/10.1038/s41557-023-01300-3.

[77] C Hackman and T E Parker. 'Noise analysis of unevenly spaced time series data'. In: *Metrologia* 33.5 (Oct. 1996), p. 457. DOI: 10.1088/0026-1394/33/5/4. URL: https://dx.doi.org/10.1088/0026-1394/33/5/4.

[78] W.J. Riley. *Handbook of Frequency Stability Analysis*. NIST Special Publication 1065. National Institute of Standards and Technology, 2008.

[79] Shi-Liang Zhu, C. Monroe and L.-M. Duan. 'Arbitrary-speed quantum gates within large ion crystals through minimum control of laser beams'. In: *Europhysics Letters* 73.4 (2006), pp. 485–491. ISSN: 0295-5075. DOI: 10.1209/epl/i2005-10424-4.

[80] Christian F. Roos. 'Ion trap quantum gates with amplitude-modulated laser beams'. In: *New Journal of Physics* 10 (2008). ISSN: 13672630. DOI: 10.1088/1367-2630/10/1/013002.

[81] Pak Hong Leung et al. 'Robust 2-Qubit Gates in a Linear Ion Crystal Using a Frequency-Modulated Driving Force'. In: *Physical Review Letters* 120.2 (2018), p. 020501. ISSN: 0031-9007. DOI: 10.1103/physrevlett.120.020501.

[82] Ye Wang et al. 'High-Fidelity Two-Qubit Gates Using a Microelectromechanical-System-Based Beam Steering System for Individual Qubit Addressing'. In: *Phys. Rev. Lett.* 125 (15 Oct. 2020), p. 150505. DOI: 10.1103/PhysRevLett.125.150505. URL: https://link.aps.org/doi/10.1103/PhysRevLett.125.150505.

[83] Pak Hong Leung and Kenneth R. Brown. 'Entangling an arbitrary pair of qubits in a long ion crystal'. In: *Phys. Rev. A* 98 (3 Sept. 2018), p. 032318. DOI: 10.1103/PhysRevA.98.032318. URL: https://link.aps.org/doi/10.1103/PhysRevA.98.032318.

[84] K. A. Landsman et al. 'Two-qubit entangling gates within arbitrarily long chains of trapped ions'. In: *Phys. Rev. A* 100 (2 Aug. 2019), p. 022332. DOI: 10.1103/PhysRevA.100.022332. URL: https://link.aps.org/doi/10.1103/PhysRevA.100.022332.

[85] Mingyu Kang et al. 'Batch Optimization of Frequency-Modulated Pulses for Robust Two-Qubit Gates in Ion Chains'. In: *Phys. Rev. Appl.* 16 (2 Aug. 2021), p. 024039. DOI: 10.1103/PhysRevApplied.16.024039. URL: https://link.aps.org/doi/10.1103/PhysRevApplied.16.024039.

[86] A.R. Milne et al. 'Phase-Modulated Entangling Gates Robust to Static and Time-Varying Errors'. In: *Physical Review Applied* 13 (2 2020), p. 024022. DOI: 10.1103/physrevapplied.13.024022.

[87] T.J. Green and M.J. Biercuk. 'Phase-Modulated Decoupling and Error Suppression in Qubit-Oscillator Systems'. In: *Physical Review Letters* 114 (12 2014), p. 120502. DOI: 10.1103/physrevlett.114.120502.

[88] C.D.B. Bentley et al. *Numeric optimization for configurable, parallel, error-robust entangling gates in large ion registers*. 2020. URL: ArXiv%20Link.

[89] Y. Lu et al. 'Global entangling gates on arbitrary ion qubits'. In: *Nature* 572 (7769 2019), pp. 363–367. DOI: 10.1038/s41586-019-1428-4.

[90] Thomas Monz et al. '14-Qubit Entanglement: Creation and Coherence'. In: *Phys. Rev. Lett.* 106 (13 Mar. 2011), p. 130506. DOI: 10.1103/PhysRevLett.106.130506. URL: https://link.aps.org/doi/10.1103/PhysRevLett.106.130506.

[91] S A Moses et al. 'A Race Track Trapped-Ion Quantum Processor'. In: *arXiv* (2023). DOI: 10.48550/arxiv.2305.03828.

[92] J. Casanova et al. 'Quantum Simulation of Interacting Fermion Lattice Models in Trapped Ions'. In: *Phys. Rev. Lett.* 108 (19 May 2012), p. 190502. DOI: 10.1103/PhysRevLett.108.190502. URL: https://link.aps.org/doi/10.1103/PhysRevLett.108.190502.

[93] M. -H. Yung et al. 'From transistor to trapped-ion computers for quantum chemistry'. In: *Scientific Reports* 4.1 (2014), p. 3589. DOI: 10.1038/srep03589. URL: https://doi.org/10.1038/srep03589.

[94] Svetoslav S. Ivanov, Peter A. Ivanov and Nikolay V. Vitanov. 'Efficient construction of three- and four-qubit quantum gates by global entangling gates'. In: *Phys. Rev. A* 91 (3 Mar. 2015), p. 032311. DOI: 10.1103/PhysRevA.91.032311. URL: https://link.aps.org/doi/10.1103/PhysRevA.91.032311.

[95] Pranav Anantha Alavandi. 'Improving Qubit Readout in a Linear Paul Trap'. School of Physics, University of Sydney, Oct. 2022.

[96] Y. Shapira et al. 'Theory of robust multiqubit nonadiabatic gates for trapped ions'. In: *Physical Review A* 101 (3 2020), p. 032330. DOI: 10.1103/physreva.101.032330.

[97] F. Haddadfarshi and F. Mintert. 'High fidelity quantum gates of trapped ions in the presence of motional heating'. In: *New Journal of Physics* 18 (2016), p. 123007. DOI: 10.1088/1367-2630/18/12/123007.

[98] C H Valahu et al. 'Quantum control methods for robust entanglement of trapped ions'. In: *Journal of Physics B: Atomic, Molecular and Optical Physics* 55.20 (Sept. 2022), p. 204003. DOI: 10.1088/1361-6455/ac8eff. URL: https://doi.org/10.1088%2F1361-6455%2Fac8eff.

[99] Ryan J. MacDonell et al. 'Predicting molecular vibronic spectra using time-domain analog quantum simulation'. In: *Chem. Sci.* 14 (35 2023), pp. 9439–9451. DOI: 10.1039/D3SC02453A. URL: http://dx.doi.org/10.1039/D3SC02453A.

[100] Harrison Burton Ball. 'Robust Quantum Control & Verification & Quantum Simulation with Trapped Ions'. PhD thesis. 2018-02-21. URL: http://hdl.handle.net/2123/17899.

ComponentLibrary by Alexander Franzen is licensed under a Creative Commons Attribution-NonCommercial 3.0 Unported License.

APPENDIX A

Appendix

A1 Cleaning

Steps must be taken to prepare the chambers and clean all the components, to aid the pressure coming down in a small evacuation time. The cleaning method used to prepare this was adapted from [100] and lab experience. It is appropriate for all of the components used in the trap (alumina, tantalum, gold, aluminium, steel and copper). Set up an ultrasonic bath with a beaker.

- If the components are from the machine shop, mix in a beaker with Alconox or diluted simple green to degrease. Sonicate for 3-5 minutes.
- Rinse the part with distilled water without sonicating
- If the parts are metallic and are oxidised, sonicate for 3-5 minutes with Citronox
- Rinse with methanol/acetone
- with fresh methanol/acetone, sonicate for 3-5 minutes
- Rinse again with distilled water and sonicate with isopropyl
- Blow the components dry with dry nitrogen
- Place the components into either the nitrogen cupboard for storage in a clean container or UHV aluminium foil

A2 Beam shaping setup

During the simulation analysis of amplitude inhomogeneity, beam profiling data of the 70 and 200 arm of the Raman beam was taken. This showed that the beam profile was 2D Gaussian and circular. In order to alter the beam profile for the Raman lasers, cylindrical lenses were used to shape the beam profile.

As demonstrated in Figure A.1, these cylindrical lenses will act as beam shaping apparatus, performing as a telescope. This can alter the ellipticity of the Raman profile before it is focused down on the ion. To test the efficacy of this setup, two sets of lenses were placed on the zeroth order beam from the 70 arm of the Raman 355nm laser setup. The effect of the lenses was measured before and after using a Thorlabs beam profiler. The vertical lenses are a $f = 30$mm and $f = 50$mm lens, creating a broadening effect. The horizontal lenses are $f = 100$mm and $f = -30$mm, creating a tightening on the Gaussian profile. These were found to have an effect of reducing the ellipticity from 90% to 60%. With further optimisation

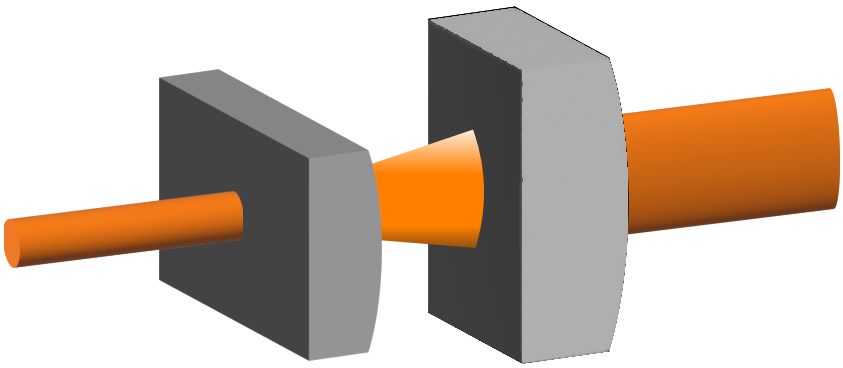

FIGURE A.1. Vertical beam shaping apparatus, showing how the circular profile is shaped by the two lenses in a similar fashion as that of a telescope. The process requires one vertical and one horizontal set of cylindrical lenses to produce the required beam shaping.

of the cages and lenses, this setup can be placed into the Raman beam path line to perform global entangling gates in large ion chains with a lower σ_{amp}.

The standard Thorlabs and Edmunds lenses had to be cut to be placed into a cage mount. The process of cutting optics is difficult as it can easily damage the optical components and straight cuts are required to fit into the cage mounts. The diamond saws in the Geophysics department of the University were used to this end and training from David Mitchell is required to operate these saws. The process below was used to cut the optics but does not represent formal training to use the saw.

Optic Protection Steps:

(1) Coat optics in cleaning glue (first contact - red glue) as per the manual.
(2) Leave to dry for 20 minutes.
(3) Tape up the optics with suitable tape that doesn't leave a strong mark.
(4) Obtain some guiding wooden paddle sticks, e.g., ice cream wooden sticks
(5) Check that the stick can guide the optics during the cut.

Cutting Preparation Steps:

(1) Check if the saw can turn on, then turn it off.
(2) Add enough water below the blade to wet the blade as it spins.

(3) Ensure that the tap is plugged in.
(4) Turn on the saw and check that water flows out over the blade and the blade is being soaked.
(5) Use a sandstone block to clean the blade from residual plastic.

Cutting Steps:

(1) Place the optic on a wooden stick.
(2) Check that it doesn't touch the base plate of the saw.
(3) Turn on the saw.
(4) Slowly cut (do not apply too much force; let the blade do the work).
(5) Keep cutting until you reach the end of the optic; sometimes it may split at the end, but to even off the cut, saw completely through.
(6) Check the quality of the cut.
(7) Use a sandstone block to clean the blade from residual plastic.

A3 AOM

In the investigation of the Mølmer-Sørensen gate, there are a number of parameters which define the optimisation of the control sequence. The segment duration (i.e. the duration of each fixed optimisable part of the piecewise constant function) is one of these and has a significant impact on the optimisation computation time and on the gate fidelity. More optimisable segments would mean higher degrees of freedom, but this must be balanced with the hardware limitations of the Raman chain. AOMs are used to imprint the modulation onto the optical pulse train. However, the pulse applied to the crystal may not have a direct mappting to the actual modulation applied to the ion and can be characterised by a transfer function. The pulses applied are defined by the AWG, where each pulse segment is defined by the Heaviside function $\Theta(t)$ [87], where

$$r_0(t;\tau_s) = A_0\Theta(t)\Theta(\tau_s - t) \tag{A.1}$$

with τ_s as the segment duration and an amplitude A_0.

The AOMs in use for the 355nm path are from IntraAction; specifically the ASM-702B8 for the 70MHz path and ASM-2002B8 for the 200MHz. These components have a fixed rise time, for example, the ASM-702B8 has a rise time of 5.5ns for 0.5mm diameter beam. This rise time can be described as a 'lag' in the applied signal onto the laser path. As this AOM is receiving the optimised pulses, each segment must therefore have a lower bound of this duration, as anything shorter would not be directly translated for the light-matter interaction. In practice, the beam diameter can be larger, changing the minimum duration time. In the Yb lab, the AOM response to modulation was characterised, highlighting the effect of amplitude and frequency modulations. For the 70MHz AOM, a signal from a Keysight 33600 AWG was sent to the AOM and the first order 355nm laser beam was measured on a Thorlabs photodetector. The beam was focused onto the photodetector and the power was reduced to a minimum so as to not saturate the photodetector. A low-pass filter was placed in to remove the noise from the 80MHz Raman beatnote.

To create the plot for the amplitude transfer function, the modulation amplitude was then increased in steps and the photodiode signal amplitude was measured. This gives an indication of the saturation point of the AOM and its response to amplitude modulation. The results of the photodetector measurement can be seen in Figure A.2. This shows that the amplitude from the control pulse does not have a linear relationship with the AOM and the transfer function must be considered when considering the experimental effect of modulation techniques. To further characterise the entire beam path, the AWG was driven at a different amplitude to drive Rabi flops on the carrier transition. The transfer function can be extracted by noting the Rabi rate for the ion and this work can be seen in [95]. This revealed that the transfer function was linear below an applied AWG amplitude of 0.3.

In addition to the amplitude characterisation, the response to segment rate was investigated by characterising the bandwidth of the AOM. In a similar fashion to Figure A.2, the AWG driving signal at 70MHz was further modulated with square modulation and sine modulation at different frequencies. This frequency was slowly increased and the amplitude of the first order on the photodiode was measured. Two different measurements from the photodiode output were taken: the peak-to-peak voltage for the oscillation (Pk-Pk) and then the root-mean-squared voltage over the cycle (Avg-Cyc). The plot reveals that both types of modulation on the driving signal have an inflexion point where the output begins to cut off, known as the cut-off frequency. This response can be fit with a Butterworth transfer function H_{Butter}, where

$$H_{butter}(f, f_c, n) = \frac{\sqrt{{f_c}^n}}{\sqrt{{f_c}^n + f^n}}, \tag{A.2}$$

Here, f_c is the frequency cut-off, n is the order of the Butterworth function and f is the frequency. Each experiment is fit with this, where the cut-off frequency is 303kHz and $7,173$kHz for the sine wave Pk-Pk and Avg-Cyc measurements, and 675kHz and $3,933$kHz for the square modulation Pk-Pk and Avg-Cyc measurements.

Using the data from this plot puts bounds on the maximum segment rate possible. The value of 32 segments per 400μs was used previously in [32]. Comparing this to the plot, the segments have a rate of 80kHz, with a minimum time of 12.5μs. This value is lower than the smallest cut-off frequency $f_c = 303$kHz in the AOM analysis and this segment rate is therefore used for the entangling gate simulation analysis.

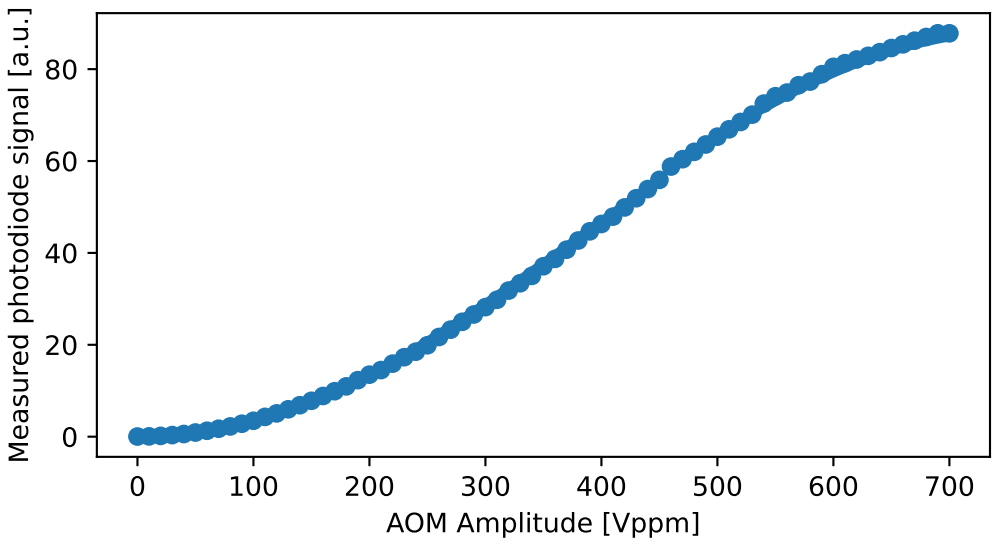

FIGURE A.2. Amplitude transfer function of the ASM-702B8 with 355nm laser light. Each data point shows the measured amplitude on a Thorlabs photodiode after modulating the amplitude of a

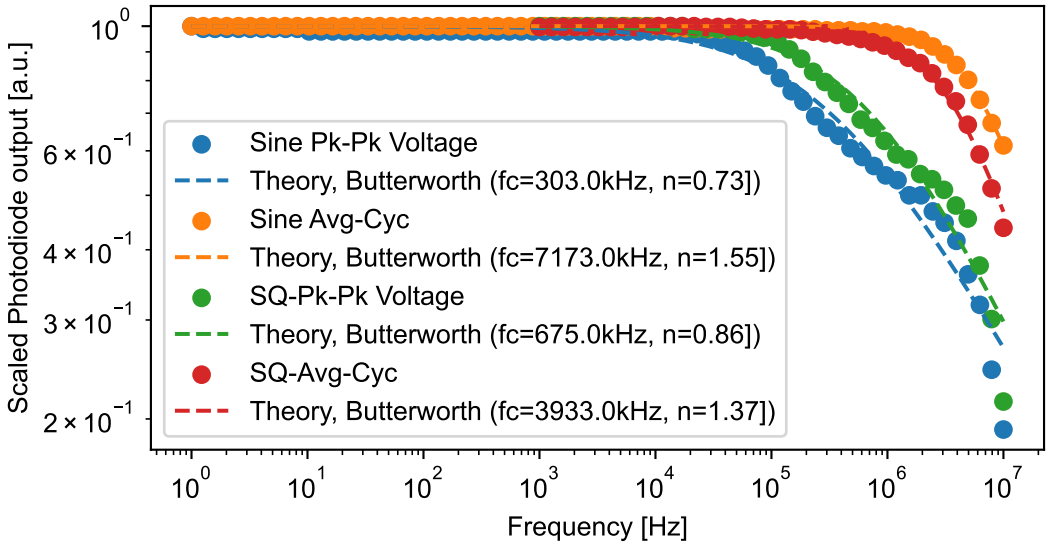

FIGURE A.3. Frequency analysis of ASM-702B8 AOM with 355nm laser light. Two modulations were tested, firstly sine amplitude modulation with increasing frequency and then square (SQ) modulation with increasing frequency. The peak-to-peak voltage (Pk-Pk) of the photodetector signal along with the RMS cyclic (Avg-Cyc) value was chosen for both of them. Each set of points has a cut-off frequency, where the scaled photodiode output begins to drop at higher frequencies.

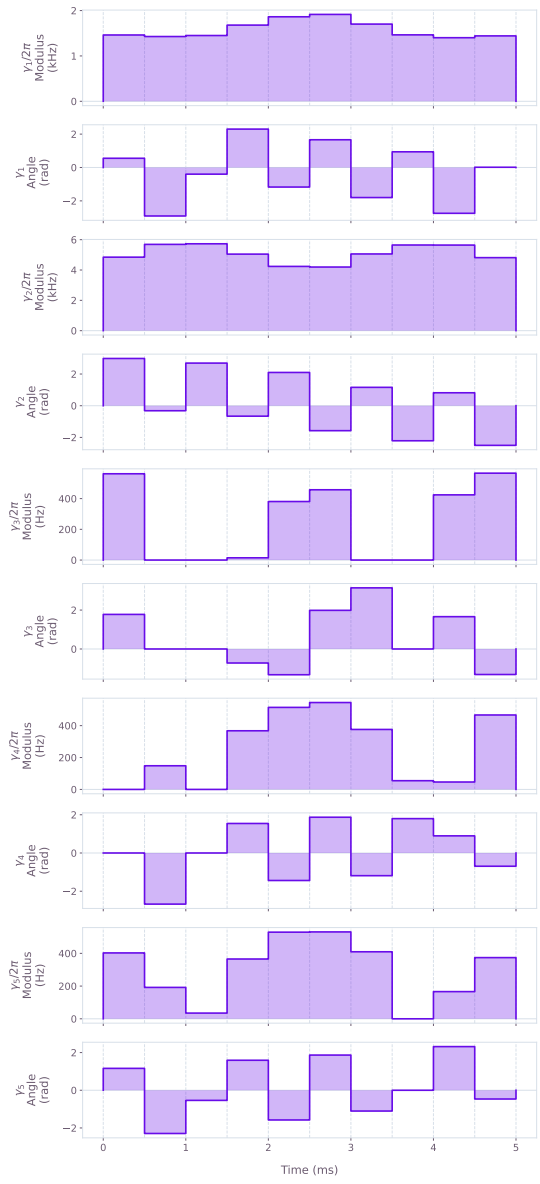

FIGURE A.4. Example of multitone controls producing the gate for 6 ions with 2×10^{-3} infidelity. Here the maximum rabi rate for each tone is 6.6kHz. Each tone has 10 segments and the pulses have a total duration of 5ms. They are detuned away from the highest radial motional mode as in fig. 4.16